



Universiteit
Leiden
The Netherlands

Spin-label EPR on Disordered and Amyloid Proteins

Hashemi Shabestari, M.

Citation

Hashemi Shabestari, M. (2013, April 16). *Spin-label EPR on Disordered and Amyloid Proteins*. Retrieved from <https://hdl.handle.net/1887/20749>

Version: Not Applicable (or Unknown)

License: [Leiden University Non-exclusive license](#)

Downloaded from: <https://hdl.handle.net/1887/20749>

Note: To cite this publication please use the final published version (if applicable).

Cover Page



Universiteit Leiden



The handle <http://hdl.handle.net/1887/20749> holds various files of this Leiden University dissertation.

Author: Hashemi Shabestari, Maryam

Title: Spin-label EPR on disordered and amyloid proteins

Issue Date: 2013-04-16

SPIN-LABEL EPR ON DISORDERED AND AMYLOID PROTEINS

Maryam Hashemi Shabestari

The work reported in this thesis was carried out at the “Leids Instituut voor Onderzoek in de Natuurkunde (LION)” and is part of the research program of the “Stichting voor Fundamenteel Onderzoek der Materie (FOM)”.

An electronic version of this dissertation is available at the Leiden University Repository (<https://openaccess.leidenuniv.nl>).

Casimir PhD series, Delft-Leiden, 2013-6

ISBN: 978-90-8593-150-8

Cover design: M. M. Motazacker

Printed by: CPI Wöhrman Print Service

SPIN-LABEL EPR ON DISORDERED AND AMYLOID PROTEINS

Proefschrift

ter verkrijging van
de graad van Doctor aan de Universiteit Leiden,
op gezag van Rector Magnificus prof.mr. C.J.J.M. Stolker,
volgens besluit van het College voor Promoties
te verdedigen op dinsdag 16 april 2013
klokke 15.00 uur

door

Maryam Hashemi Shabestari

geboren te Teheran, Iran

in 1979

Promotiecommissie

Promotor:	Prof. dr. E.J.J. Groenen	Universiteit Leiden
Co-promotor:	Dr. M. Huber	Universiteit Leiden
Overige leden:	Prof. dr. E.R. Eliel	Universiteit Leiden
	Dr. C.W.M. Kay	University College London
	Prof. dr. M. Dogterom	FOM Instituut AMOLF, Universiteit Leiden
	Prof. dr. M. Ubbink	Universiteit Leiden
	Dr. A. Alia	Universiteit Leiden

*To my beloved mother and father,
Mitra, Mehran, Masoud,
and – Mahdi of course*

CONTENTS

1 Introduction	1
1.1 Introduction to EPR spectroscopy	2
1.1.1 Zeeman interaction and hyperfine interaction	2
1.1.2 Spin labels for protein EPR.....	4
1.1.3 Dynamics by EPR: the rotation-correlation time	5
1.1.4 Spin-spin interaction.....	6
1.2 The proteins and their properties	10
1.2.1 Structure of proteins.....	10
1.2.2 Misfolding and aggregation of proteins	11
1.2.3 Diseases that involve protein misfolding and aggregation	12
1.2.3.1 Alzheimer's disease: the amyloid β peptide.....	12
1.2.3.2 Parkinson's disease: the α -synuclein protein.....	13
1.2.4 Proteins with disordered regions: the light-harvesting protein CP29	14
1.3 Thesis outline.....	15
2 The effect of a membrane mimicking detergent on amyloid β aggregation	19
<i>Overview and the regime of high detergent concentration</i>	
2.1 Introduction.....	20
2.2 Materials and methods.....	21
2.2.1 Sample preparation protocol	21
2.2.2 EPR experiments.....	22
2.2.3 The amount of spin label in different samples.....	22
2.2.4 Simulations of EPR spectra, interpretation of the rotation-correlation time	22
2.3 Results.....	23
2.3.1 Effect of SDS on the amount of different components.....	26
2.3.2 The size of aggregates at different concentrations of SDS.....	27
2.4 Discussion.....	28
2.4.1 The high SDS concentration species of A β	28
2.4.2 A β at intermediate SDS concentrations	29
3 Interaction of the amyloid β peptide with a membrane mimicking detergent	33
<i>The regime of sub-micellar detergent concentration</i>	
3.1 Introduction.....	34
3.2 Materials and methods.....	34
3.2.1 Sample preparation protocol	34

3.2.2 EPR experiments.....	35
3.2.3 Simulations of EPR spectra	35
3.3 Results	35
3.3.1 Effect of SDS on the amount of different components	39
3.3.2 Effect of SDS on the rotation-correlation time	39
3.4 Discussion.....	40
4 The aggregation potential of 1-15 and 1-16 fragments of the amyloid β peptide and their influence on the aggregation of Aβ40	47
4.1 Introduction	48
4.2 Materials and methods.....	49
4.2.1 Sample preparation protocol	49
4.2.2 EPR experiments.....	50
4.2.3 Simulations of EPR spectra	50
4.2.4 Ratio of the intensity of the “fast” and “slow” components in each spectrum	50
4.2.5 Thioflavin T fluorescence assay	51
4.3 Results	51
4.4 Discussion.....	56
5 Elucidating the α-synuclein fibril fold with pulsed EPR.....	61
5.1 Introduction	62
5.2 Materials and methods.....	62
5.2.1 Expression and purification of cysteine variants of α S	62
5.2.2 Preparation and harvesting of fibrillar α S	63
5.2.3 Atomic force microscopy (AFM)	63
5.2.4 Continuous-wave EPR at 80 K and at room temperature	64
5.2.5 DEER measurements.....	64
5.2.6 General structure parameters of fibrils.....	65
5.3 Results	65
5.3.1 Continuous-wave EPR.....	66
5.3.2 Pulsed EPR	67
5.4 Fibril fold model	71
5.5 Discussion.....	76
6 Exploring the structure of the N-terminus of the plant antenna protein CP29	79
6.1 Introduction	80
6.2 Materials and methods.....	81
6.2.1 Mutagenesis, labeling, and pigment reconstitution.....	81
6.2.2 Continuous-wave EPR measurements	82

6.2.3 Simulation of the cw EPR spectra	82
6.2.4. Assessment of the cw EPR spectra	83
6.2.5 Parameters to estimate the length of protein regions	83
6.2.6 Pulsed EPR measurements.....	84
6.3 Results	84
6.3.1 Continuous-wave EPR.....	84
6.3.2 Pulsed EPR	90
6.4 Localization of residue 4 of the N-terminus	93
6.5 Discussion.....	95
7 Structure and first EPR characterization of helical peptides with TOAC spin labels: models for short distances.....	99
7.1 Introduction.....	100
7.2 Materials and methods	101
7.2.1 Synthesis and characterization of peptides	101
7.2.2 Fourier transform infrared absorption spectroscopy	102
7.2.3 EPR spectroscopy.....	102
7.2.4 Preparation of the samples	102
7.2.5 Simulation	103
7.3 Results	103
7.3.1 Conformational analysis	103
7.3.2 Room temperature cw EPR.....	104
7.3.3 NONA ₂ and NONA _{2,8} at X-band, in frozen solution.....	108
7.3.4 NONA ₂ and NONA _{2,8} at W-band, in frozen solution	109
7.4 Discussion.....	110
7.4.1 Origin of the narrow-line contribution	111
7.4.2 The relation between structure and J-coupling	111
7.4.3 The contribution of dipolar interaction	112
7.4.4 Summary and conclusions	112
Appendix A: supporting information on chapter 2	115
Appendix B: supporting information on chapter 6	117
List of abbreviations.....	123
Summary	125
Samenvatting	129
Publications	133
Curriculum Vitae	135
Acknowledgement	137

CHAPTER 1

INTRODUCTION

This chapter is a general introduction to the work presented in this thesis. A brief overview of the techniques used and the proteins investigated is provided. At the end, the outline of the chapters of the thesis is given.

1 Introduction

Proteins are essential for organisms and participate in virtually every process within cells ^[1]. Knowledge about the structure of proteins provides crucial information about their function in biological mechanisms. In determining the structure of proteins with biophysical approaches, electron paramagnetic resonance (EPR) is rapidly gaining ground ^[2-13]. The aim of this thesis is to provide insight in how broad the application of EPR can be to study proteins, in particular those which are difficult if not impossible to study with other approaches. The focus of this thesis is to investigate the aggregation and misfolding of intrinsically disordered proteins and to determine the structure of disordered parts of proteins with EPR. Specifically, the amyloid β (A β) peptide, the α -synuclein (α S) protein, and the light-harvesting protein CP29 are studied. In the present chapter, the basic theory of EPR spectroscopy is described and an overview of the proteins studied is provided.

1.1 Introduction to EPR spectroscopy

1.1.1 Zeeman interaction and hyperfine interaction

In EPR spectroscopy, transitions between the spin levels of a paramagnetic system are induced by electromagnetic radiation in a static magnetic field ^[14,15]. The interaction between the electron spin, \vec{S} , and the external magnetic field is called the electron Zeeman interaction (H_{EZ}). In the presence of the external magnetic field, the electron spin occupies one of two states, which can be thought of as the electron spin aligned with or against the magnetic field.

In addition to the Zeeman interaction, the electron spin experiences a small local magnetic field produced by nearby nuclei. This interaction is known as the hyperfine interaction (H_{HF}), and may counter or enhance the externally applied field. Taking into account the Zeeman interaction and the hyperfine interaction with one nuclear spin, \vec{I} , the spin Hamiltonian can be written as:

$$H = H_{EZ} + H_{HF} = \beta_e \vec{B}_0 \vec{g}_e \vec{S} + \vec{S} \vec{A} \vec{I} \quad (1.1)$$

Here β_e is the Bohr magneton, \vec{B}_0 is the external magnetic field, \vec{g}_e is the g-tensor, and \vec{A} the hyperfine tensor. Figure 1.1 shows the corresponding energy level scheme for a nitroxide spin label, which contains an electron spin ($S = 1/2$) and a nitrogen (^{14}N , $I = 1$) nuclear spin. In the magnetic field the degenerate $M_s = 1/2$, $-1/2$ magnetic sublevels of the electron spin split up by the Zeeman interaction and a further splitting into three $M_I = 1, 0, -1$ nuclear spin magnetic sublevels results from the hyperfine interaction. The EPR transitions correspond to transitions between

levels for which $|\Delta M_s| = 1$ and $\Delta M_I = 0$. For an isotropic g -tensor and an isotropic hyperfine tensor, the energy difference between the levels involved in the three transitions can be written as: $\Delta E = g_e \beta_e B_0 + A_{iso} M_I$ with $M_I = 1, 0, -1$. The isotropic g_e has the value of 2.00551^[16] and A_{iso} of a nitrogen (^{14}N , $I = 1$) nuclear spin of a nitroxide spin label has the typical value of about 1.63 mT^[16]. The transitions show up in the EPR spectrum at magnetic fields such that the resonance condition $\Delta E = h\nu$ is fulfilled, where h is Planck's constant ($h = 6.626 \times 10^{-34}$ Js) and ν the frequency of the electromagnetic radiation.

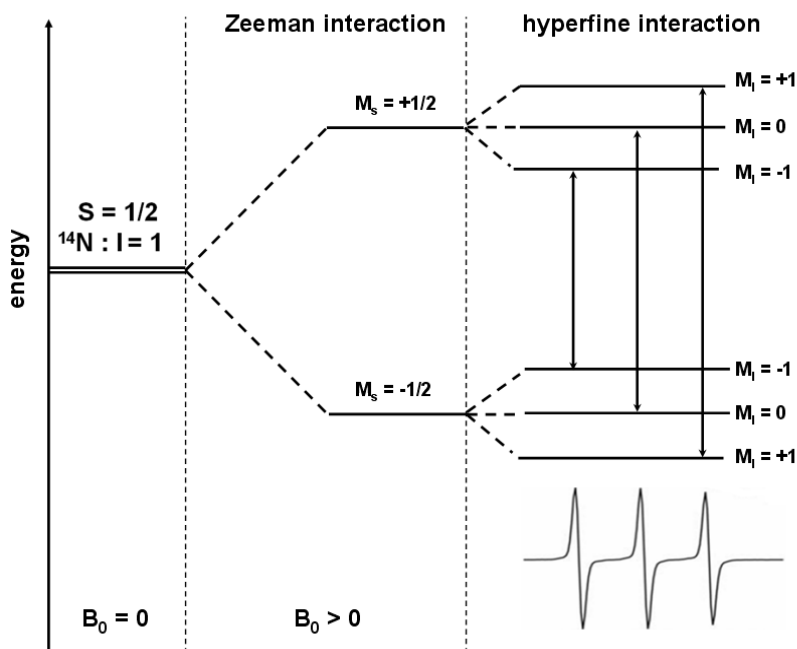


Figure 1.1 Energy level scheme and allowed EPR transitions for an electron spin ($S = 1/2$) in interaction with a ^{14}N nitrogen nuclear spin ($I = 1$). The hyperfine interaction leads to a splitting into $2I + 1 = 3$ transitions, each corresponding to a ^{14}N nuclear spin state ($M_I = -1, 0, +1$).

For anisotropic g and hyperfine tensors, the orientation of the magnetic field with respect to the molecular system has to be taken into account^[11]. The principal components of the hyperfine interaction tensor (\vec{A}) are defined as A_{xx} , A_{yy} , and A_{zz} , those of the g -tensor as g_{xx} , g_{yy} , and g_{zz} . For nitroxide spin labels typical values of the hyperfine interaction of the nitrogen (^{14}N , $I = 1$) nuclear spin are $A_{xx} \approx A_{yy} \approx 0.7$ mT and $A_{zz} \approx 3.5$ mT. The isotropic hyperfine-coupling $A_{iso} = (A_{xx} + A_{yy} + A_{zz})/3$. The difference between A_{xx} and A_{yy} is small and often the hyperfine tensor is

assumed to be axially symmetric. The magnitude of A_{zz} gives an indication of the polarity of the environment. In contrast to the hyperfine tensor, the g -tensor is rhombic with typical values of $g_{xx} \approx 2.00800$, $g_{yy} \approx 2.00586$, and $g_{zz} \approx 2.00199$ ^[11]. The anisotropy of the Zeeman and the hyperfine interactions determines the sensitivity of the EPR spectrum to the orientation and rotational motion of the spin label.

1.1.2 Spin labels for protein EPR

Spin labels are extrinsic paramagnetic probes, which are commonly nitroxide derivatives with a stable unpaired electron and a functional group that allows its site-specific attachment to a protein, site-directed spin labeling ^[11,17]. The nitroxide radicals are stable due to the presence of methyl groups adjacent to the nitroxide. Figure 1.2 shows the structure of the two nitroxide spin labels, which are used in this thesis: the MTS spin label ((1-oxyl-2,2,5,5-tetramethylpyrroline-3-methyl) methanethiosulfonate), and the non-coded nitroxyl-containing α -amino acid, TOAC (2,2,6,6-tetramethylpiperidine-1-oxyl-4-amino-4-carboxylic acid). The TOAC spin label serves as a rigidly attached spin label ^[18,19] compared to the rotationally flexible MTS spin label.

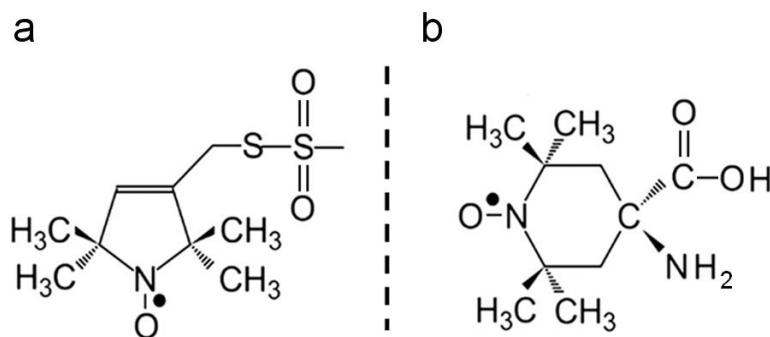


Figure 1.2 The chemical structure of two nitroxide radicals. a: The MTS spin label. The NO group of the MTS spin label is part of a five-membered pyrrole ring. b: The TOAC spin label. The NO group of the TOAC spin label is part of a six-membered piperidine ring. The black dot represents the unpaired electron.

Rotational motions of the nitroxide lead to partial averaging of the anisotropy between the elements of the g -tensor and the hyperfine tensor, and give rise to variations in the observed cw-EPR spectrum. The cw-EPR spectrum of a nitroxide spin label can be used to infer information about the local environment of the labeling site. Through EPR analysis, it is possible to determine the local structure and dynamics, to map inter-residue distances, and to reconstruct the three-dimensional structure of proteins.

1.1.3 Dynamics by EPR: the rotation-correlation time

The shape of the EPR spectrum depends not only on the static interactions in the paramagnetic molecule, but also on the dynamic processes on the timescale of the EPR experiment. The EPR timescale is determined by the anisotropy of the g and A tensors of the molecule. These cause the spectral anisotropy, i.e., the maximum difference between resonance line positions when the orientation of the molecule is varied ^[17]. Any dynamic process on the timescale determined by the g and A tensor anisotropy will affect the shape of the EPR spectrum. The most important dynamic process in solution is the tumbling of the molecules, which is characterized by the rotation-correlation time τ_r . Figure 1.3 shows the four dynamic regimes that are distinguishable ^[17,20].

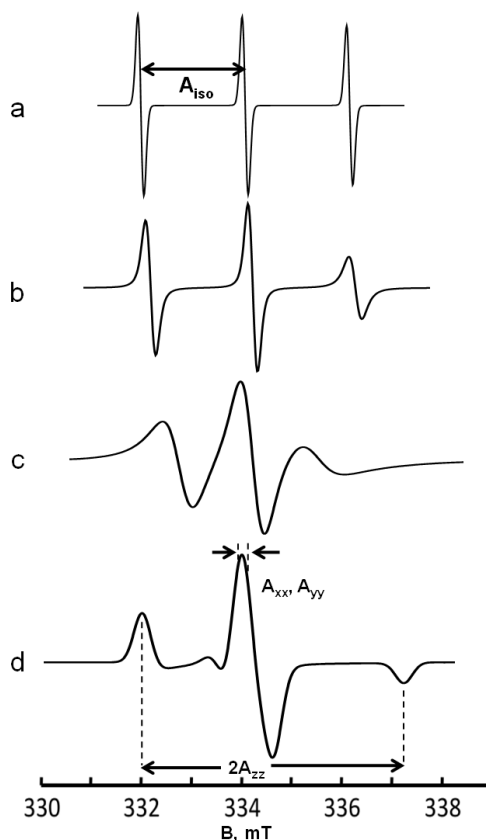


Figure 1.3 Simulation of the effect of the rotation-correlation time on the line-shape of the EPR spectrum of a nitroxide spin label. In the isotropic limit the three lines have equal intensities. a: liquid solution EPR spectrum of the nitroxide spin label with $\tau_r = 0.1$ ns. b: liquid solution EPR spectrum of the nitroxide spin label with $\tau_r = 0.4$ ns. c: liquid solution EPR spectrum of the nitroxide spin label with $\tau_r = 2.2$ ns. d: frozen solution EPR spectrum of the nitroxide spin label.

In the isotropic limit, the anisotropy is completely averaged due to the extremely fast tumbling of the molecules. The lines are symmetric and have an equal width and heights. In the fast-motion regime the rotation is fast enough to average the anisotropy, but the lines have different widths and heights. In the slow-motion regime, the rotation of the molecules is not fast enough to fully average the anisotropy. Therefore, the lines broaden and shift with respect to the isotropic limit. From the amount of spectral change, the rotation-correlation time can be obtained by simulation ^[20]. In the rigid limit, the molecules are randomly oriented with respect to the magnetic field and immobilized, and the EPR spectrum shows the full anisotropy. Line-shape analysis of EPR spectra reveals information about the local dynamics and possibly about the local structure elements of proteins ^[3,4,6].

1.1.4 Spin-spin interaction

Distance determination in biological molecules can be done by introducing spin labels at two positions and measuring the distance between the labels by EPR. The two labels can interact via two mechanisms: the exchange interaction, the magnitude of which is J , and the dipole-dipole interaction. The exchange interaction is related to the overlap of the orbitals that contain the two unpaired electrons. Depending on the magnitude of this orbital overlap, which is determined by the separation between the orbitals, the exchange interaction can cause multiplet spectra or line broadening. When the overlap is large, the two electron spins can be in two states: a singlet and a triplet state ($S = 0, 1$). The triplet state is lower in energy, thus we consider the two electron spins to be in the triplet state. In the presence of an external magnetic field the three $M_s = 1, 0, -1$ magnetic sublevels of the triplet state split up by the Zeeman interaction. In the case of two nitroxides, owing to the presence of two nuclear spins: $M_I^1 = 1, 0, -1$, and $M_I^2 = 1, 0, -1$, a further splitting results from the hyperfine interaction (figure 1.4). Considering the allowed transitions ($|\Delta M_s| = 1$ and $\Delta M_I = 0$), in the strong exchange limit, where the ratio of A_N/J is small, the spectrum contains five lines with intensities 1:2:3:2:1 with a spacing of one-half of the hyperfine coupling constant for the nitroxide spin label (figure 1.4). When the ratio of A_N/J is one-half, the transitions between the singlet and the triplet state can be observed as satellite lines. When the ratio of A_N/J increases, the transitions arrange into three groups of lines, and finally when the exchange interaction is weak, the three-line spectrum results, which is characteristic of a nitroxide spin label. Exchange interactions are usually negligible at distances beyond 1.5 nm.

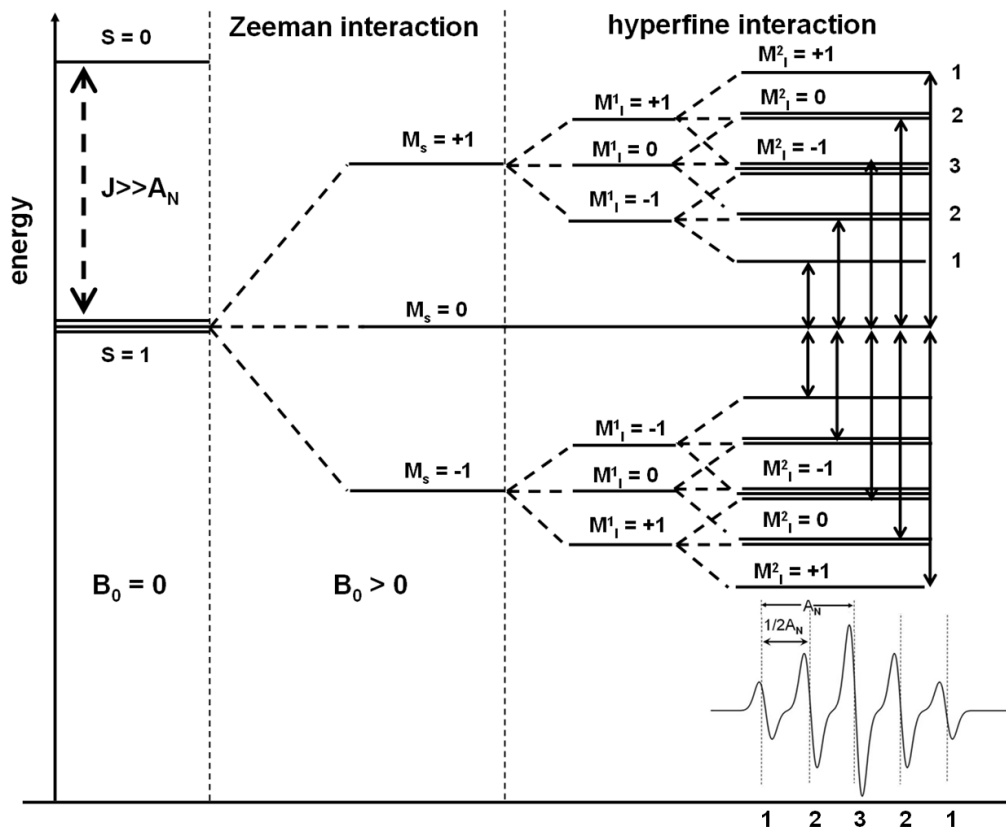


Figure 1.4 Energy level scheme for the two electron spins ($S = 1/2$) and two nitrogen (^{14}N , $I = 1$) nuclear spins for $J \gg A_N$. The spectrum contains five lines with intensities 1:2:3:2:1 with a spacing of one-half of the hyperfine coupling constant for the nitroxide spin label.

The dipole-dipole interaction is inversely proportional to the cube of the distance. The dipole-dipole interaction in frequency units, ν_{dd} , between two spins A and B is given by:

$$\nu_{dd} = -\frac{\mu_0 \beta_e^2}{8\hbar \pi^2} \frac{g_A g_B}{r_{AB}^3} (3\cos^2 \theta - 1) \quad (1.2)$$

Here g_A and g_B are the isotropic g factors of the two electron spins, r_{AB} is the magnitude of the vector that joins the two electrons, and θ is the angle between the magnetic field and the vector that joins the two electrons (figure 1.5). The dipole-dipole interaction causes line splitting or line broadening in cw EPR, which are resolved in nitroxides at spin-spin distances shorter than 1.5 nm ^[13,21].

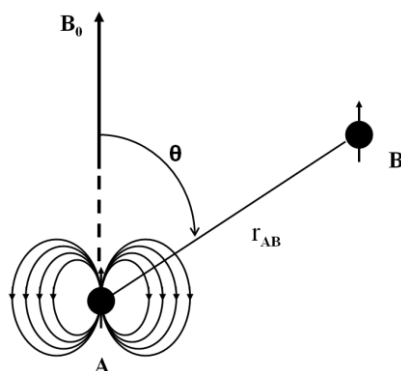


Figure 1.5 Schematic representation of the dipole-dipole interaction in a magnetic field between two electrons A and B represented as black circles.

For nitroxide spin labels at distances larger than 2 nm the dipole-dipole interaction is not resolved in the cw EPR spectra. Long-range distances (2 to 8 nm) can be measured with pulsed double electron-electron resonance spectroscopy (DEER), also called PELDOR^[22]. This technique is based on the detection of the modulation of the echo amplitude, caused by the dipolar interaction of two spins. Microwave pulses of two different microwave frequencies are used, where the two frequencies select different orientations or different spin states of the ^{14}N nucleus in the two radicals. The pulse sequence of the four-pulse DEER is shown in figure 1.6. At the observer frequency (mw_1), a refocused echo with a fixed position in time is detected for spins in resonance (spins A). Between the second and third pulse, an inversion pulse is applied at the pump frequency (mw_2), which flips the spins that are in resonance with the second frequency (spins B). Dipolar interaction between spins A and spins B results in the modulation of the amplitude of the refocused echo as a function of time, t (figure 1.7). The modulation frequency is given by equation 1.2. To determine the distance distribution for two sites within the same macromolecule, the contribution of the interactions of spins within the same molecule should be separated from the background contribution due to the interactions with spins in neighboring macromolecules. The echo signal is a multiplication of these two contributions.

Due to the flexibility of the macromolecules and conformational freedom of the spin label, the spin-spin distance is not always as sharply defined as in the rigid biradical shown in figure 1.7. In the case of proteins often broad distance distributions result, which will be addressed in chapters 5 and 6 of this thesis. The overall signal shows the superposition of modulations at different frequencies, rather than a single frequency. In that case separation of the background contribution from the modulation is improved by using an experimental background

function from the corresponding singly labeled protein (chapter 5). By means of regularization methods or model-based approaches, it is then possible to extract the distance distributions from the DEER time traces ^[23,24].

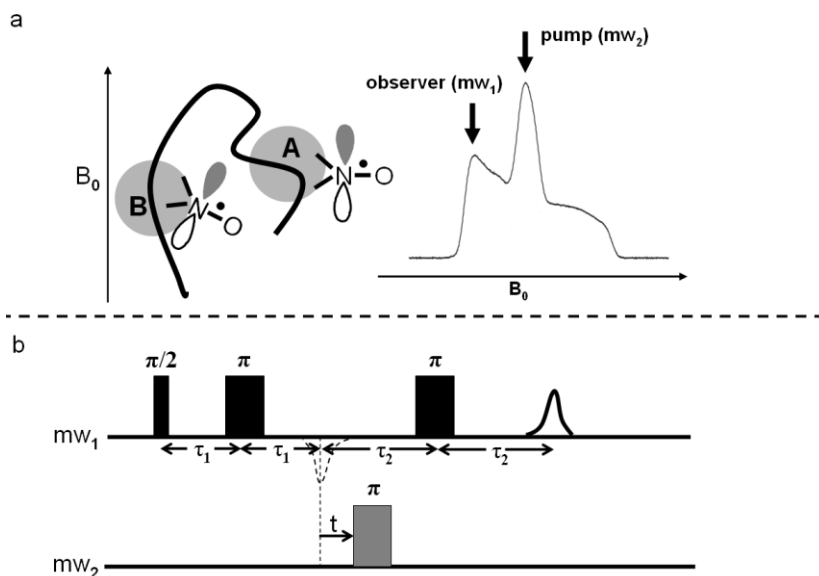


Figure 1.6 The principle of double electron-electron resonance (DEER) spectroscopy. a: Right: absorption type EPR spectrum showing resonances of observed and pumped spins. Left: a macromolecule with two nitroxide spin labels, A and B. The two spin label N-O groups have different orientations with respect to the magnetic field, B_0 . b: Pulse sequence of the DEER experiment consisting of the refocused echo sequence at frequency mw_1 that excites exclusively spins A and a pump pulse at frequency mw_2 that excites exclusively spins B. Delays τ_1 and τ_2 are fixed, and the amplitude of the echo is monitored while the time delay t is varied.

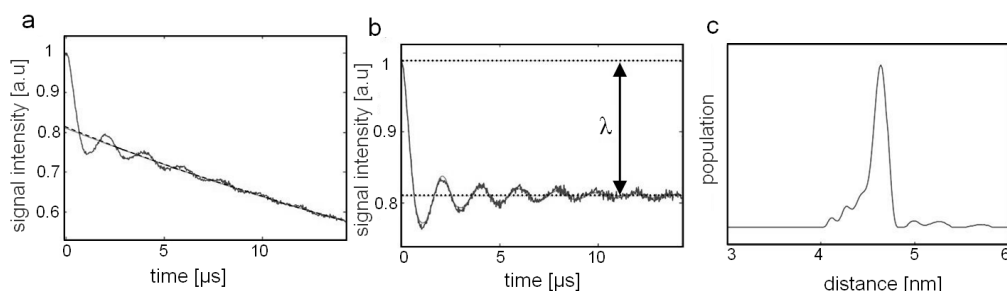


Figure 1.7 Analysis steps of DEER distance measurement on a rigid biradical. a: Raw DEER time trace. The dashed line is the background fit. b: The background corrected DEER time trace. The modulation depth, λ is related to the fraction of coupled spins. c: Distance distribution obtained by the Tikhonov regularization method ^[25]. Small features are probably artifacts of the regularization at distances longer than 5 nm.

1.2 The proteins and their properties

1.2.1 Structure of proteins

Proteins are composed of amino-acid residues. Each amino-acid residue is connected to the next one by a peptide bond and forms the polypeptide chain. The order of the amino-acid residues in the polypeptide chain determines the primary structure of the protein. The secondary structure of the protein refers to the polypeptide folding patterns, which are classified as α -helices, β -sheets, turns and random coils (figure 1.7).

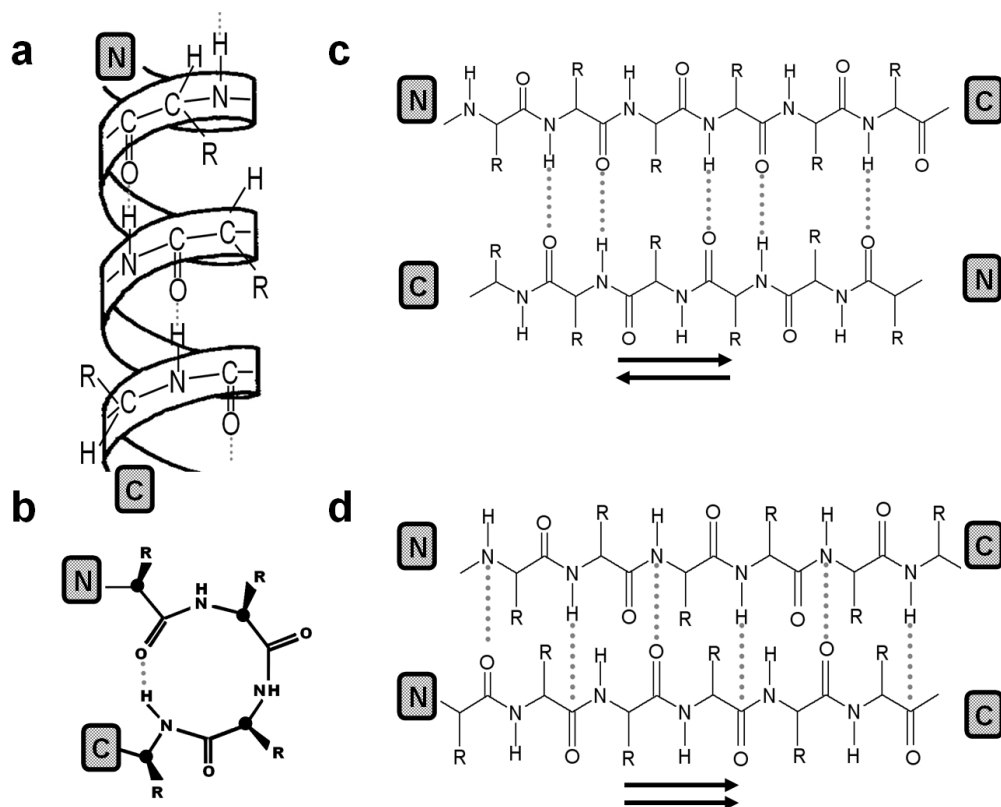


Figure 1.8 Secondary structure elements of proteins. a: α -helix, b: turn (the black-filled circles represent the C_α atoms in the turn) c: anti-parallel β -sheet, and d: parallel β -sheet. The dotted lines depict the hydrogen bonds. The N in a box corresponds to the N-terminus and the C in a box corresponds to the C-terminus of the proteins. Arrows show the direction of the β -strands in the β -sheets.

A typical α -helix is a right-handed helix with 3.6 amino-acid residues per turn, and a pitch (the distance the helix rises along its axis per turn) of 5.4 Å. In an α -helical structure the backbone hydrogen bonds are arranged such that the C=O bond of the i th amino-acid residue points along the helix axis towards the N-H group of the ($i +$

4)th amino-acid residue, which results in a strong hydrogen bond. The amino-acid side chains in an α -helix project either outward or downward from the helix. Like the α -helix, the β -sheet uses the full hydrogen-bonding capacity of the polypeptide backbone. However, in β -sheets hydrogen bonding occurs between neighboring polypeptide chains rather than within one chain (compare figure 1.8.a with c and/or d). The β -sheets can be grouped into two different classes: anti-parallel β -sheets, in which neighboring hydrogen-bonded polypeptide chains run in opposite directions (figure 1.8.c) and parallel β -sheets, in which polypeptide chains run in the same direction (figure 1.8.d). Turns are typically stretches of polypeptide chains that can easily change direction (figure 1.8.b). Turns join different α -helices and/or strands of β -sheets in proteins.

1.2.2 Misfolding and aggregation of proteins

Protein misfolding and aggregation occurs in biological processes, both in vital and disruptive processes ^[26]. In contrast to most of the protein aggregates, which are amorphous, some of the protein aggregates generate amyloid fibrils. Amyloid fibrils are about 10 nm in diameter, and are composed typically of 2 to 6 protofilaments ^[26-28]. Amyloid fibrils of all proteins share a common cross- β structure, wherein the β -strands (figure 1.9.a) are oriented perpendicular to the fibril axis. The β -sheets grow in the direction of the fibril axis by attaching proteins at the ends of the β -sheets (figure 1.9.b). Due to the large size, low solubility, and the noncrystalline nature of fibrils ^[29], understanding the molecular details of amyloid fibrils has remained a challenge. Amyloid fibrils play a role in neurodegenerative diseases, like Alzheimer's disease and Parkinson's disease ^[30].

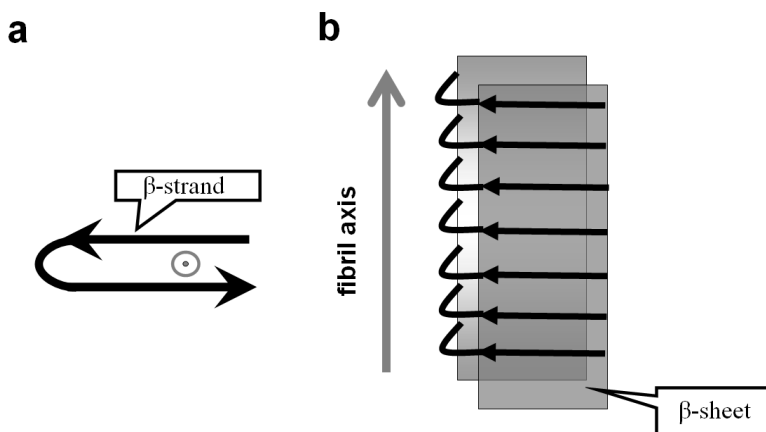


Figure 1.9 Schematic representation of the structure elements of amyloid fibrils. a: the black arrows show a β -strand and the grey dot shows the direction of the fibril axis, which is pointing out of the page. b: the grey arrow shows the direction of the fibril axis. The grey sheets are representative of β -sheets which are parallel to the fibril axis.

1.2.3 Diseases that involve protein misfolding and aggregation

1.2.3.1 Alzheimer's disease: the amyloid β peptide

Alzheimer's disease is the most common neurodegenerative disease in the aging population. Alzheimer's disease is associated with confusion, irritability, aggression, mood swings, trouble with language, progressive cognitive decline, and profound neuronal loss ^[31-35]. It is characterized by accumulation of intraneuronal neurofibrillary tangles and extracellular senile plaques in the brain tissue and ultimately neuronal and synaptic degeneration ^[31,33,36,37]. The senile plaques are formed from deposition of the amyloid β ($A\beta$) peptide in an aggregated fibrillar form.

The $A\beta$ peptide is the product of sequential proteolytic cleavage of the amyloid precursor protein (APP), a transmembrane protein located in the neuronal membrane ^[38,38,39]. The cleavage of APP is done by α -, β -, and γ -secretases via two distinct pathways: amyloidogenic and non-amyloidogenic ^[30] (figure 1.10). In the non-amyloidogenic pathway, APP is cleaved by α -secretases and subsequently cleaved by γ -secretases, whereas in the amyloidogenic pathway β -secretase cuts first, followed by γ -secretase cleavage resulting in the amyloid peptides with sequence length ranging from 38 to 43 amino-acid residues. There is evidence for other pathways, involving cleavage of the N-terminus of the $A\beta$ by both α - and β -secretases, which result in the production of several soluble, shorter $A\beta$ fragments in the cerebrospinal fluid ^[34,38,40,41]. Some of these fragments are up-regulated in Alzheimer's disease. The aggregation potential of two of these shorter peptides and their influence on the full-length $A\beta$ peptide is investigated in chapter 4.

Soluble $A\beta$ oligomers, rather than fully formed $A\beta$ fibrils and plaques are currently considered as the more likely culprits in cellular toxicity and play an essential role in the pathogenesis of Alzheimer's disease ^[29,42,43]. The potent pathologic effects of $A\beta$ oligomers provide a compelling reason for elucidating the mechanism(s) leading to the transformation of monomeric $A\beta$ into toxic oligomers and ultimately larger aggregates ^[44-46]. The hydrophobic part of $A\beta$ suggests a possible membrane activity of the peptide. In chapters 2 and 3 we study and monitor the aggregation process of $A\beta$ on the time scale of EPR in the presence of a membrane mimetic agent.

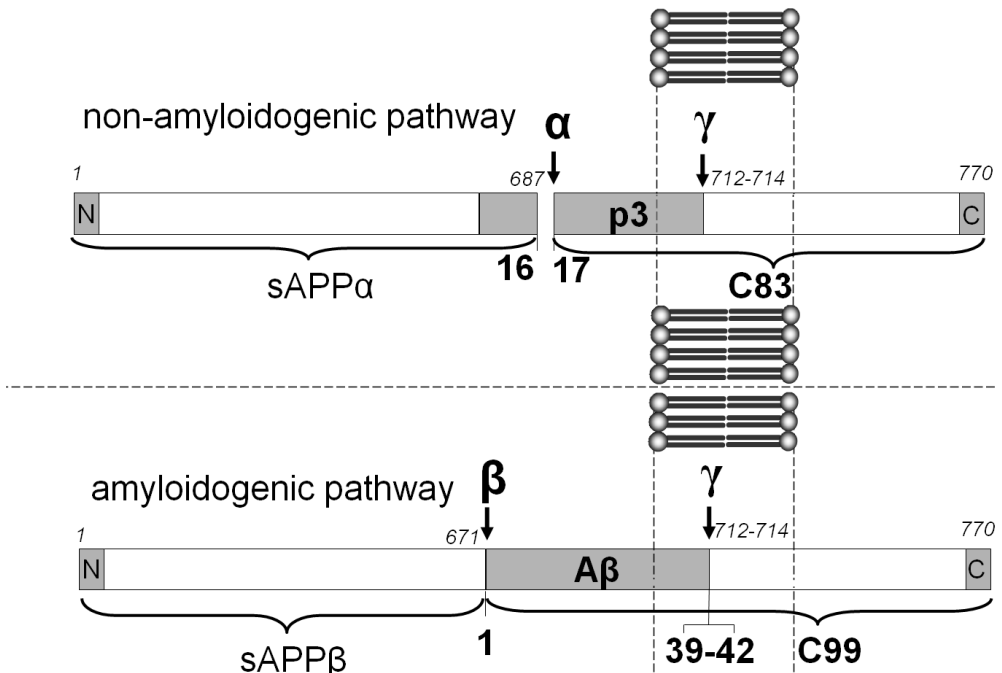


Figure 1.10 Schematic overview of processing of the amyloid precursor protein (APP). The top panel shows the non-amyloidogenic α -secretase pathway, in which soluble APP α -cleaved (sAPP α) and C83 are generated. Subsequent hydrolysis by the γ -secretase produces a p3 peptide that does not form amyloid deposits. The bottom panel represents the amyloidogenic pathway, in which cleavage of APP by the β -secretase followed by γ -secretase, liberates sAPP β and C99 and A β peptides (A β 39 to A β 42) that are found in plaque deposits. *Italics*: sequence numbers of APP protein.

1.2.3.2 Parkinson's disease: the α -synuclein protein

Parkinson's disease is the second-most frequent neurodegenerative disorder, which affects more than 1 % of the population above 60 years of age ^[47]. The most obvious symptoms in Parkinson's disease include tremor, stiffness, slowness of movement, difficulty with walking, and a specific gait. Parkinson's disease is characterized by the accumulation of a neuronal protein, α -synuclein (α S), in Lewy bodies, which are the pathological hallmark of Parkinson's disease. Misfolding and aggregation of the α S protein is accompanied by the loss of dopaminergic neurons in the substantia nigra, a region in the midbrain, and insufficient formation of dopamine, which is important for movement ^[30,48-50]. The name synuclein arises from the evidence that this protein localizes to synaptic vesicles and portions of the neuronal nucleus ^[30], but it has also been observed in the cytosol ^[51,52].

The α S protein (40 kDa) consists of 140 amino-acid residues, of which the N-terminus has a propensity to acquire α -helical structure ^[53,54]. The central region,

enclosed by amino-acid residues 61 to 95, the so-called NAC region, is hydrophobic and is crucial in the aggregation of α S^[55,56] (figure 1.11). The C-terminus of α S is negatively charged and mostly remains unstructured (amino-acid residues 100 to 140). When exposed to phospholipids, detergents or vesicles, α S forms an α 11/3 helix, which has 3.67 amino-acid residues per turn instead of 3.6 amino-acid residues per turn of an ideal α -helix^[57-60]. This amphiphatic helix allows the α S protein to associate with the surface of membranes^[57].

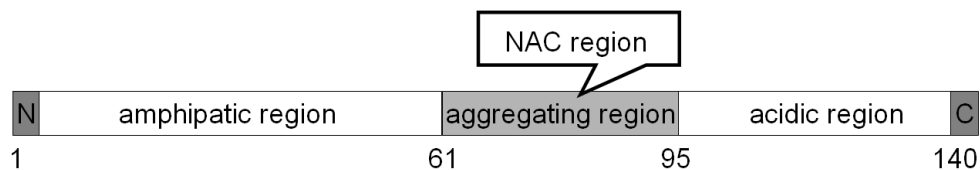


Figure 1.11 A schematic view of the α -synuclein protein. The highlighted region, amino-acid residues 61 to 95, is reported as the main part involved in the aggregation. The N in a box corresponds to the N-terminus and the C in a box corresponds to the C-terminus of the protein.

Under certain conditions in vitro^[58,60] (see chapter 5 of this thesis), α S forms oligomers and ultimately fibrils. The β -sheet core of the fibril starts at amino-acid residues 35-38 and ends around amino-acid residues 89-96^[21,61-64]. The fibrils have a cross- β -sheet structure, which is characterized by x-ray and electron diffraction, in which individual β -strands stack perpendicular to the fibril axis. However, the details of folding and arrangement of α S monomers in the fibrils are still unresolved. In chapter 5 we investigate the fold of α S in the fibril, using distance determination with pulsed EPR.

1.2.4 Proteins with disordered regions: the light-harvesting protein CP29

In plants, oxygenic photosynthesis, a process in which solar energy is converted into chemical energy, occurs in the membrane of thylakoids in chloroplasts (figure 1.12). The light-driven charge separation occurs in two chlorophyll-binding protein complexes, photosystem I and photosystem II. The light-harvesting protein CP29 is a member of the photosystem II protein complex machinery. It is located between the major light-harvesting complex LHCII and the core complex^[65]. Besides light-harvesting and energy transfer it has a photoprotective function. For light-regulation, CP29 seems to make use of its N-terminus, a stretch of about 100 amino-acid residues. In the recently solved crystal structure of CP29^[65], the N-terminus has no defined electron density. Site-directed spin labeling combined with

EPR enables us to investigate the structure of the disordered N-terminus of CP29. Our study involves two approaches: exploring the mobility of the spin label with continuous wave EPR and distance determination with pulsed EPR. From the present EPR investigation the presence of multiple conformations of the N-terminus is concluded.

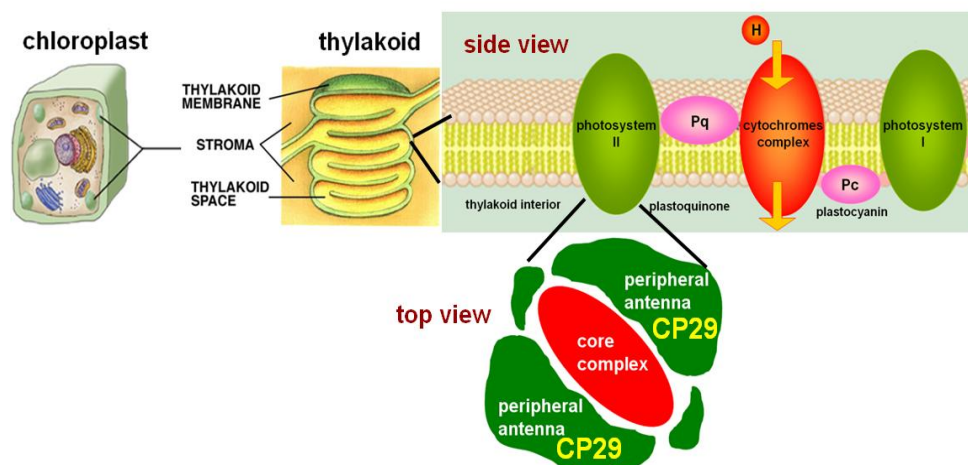


Figure 1.12 Schematic representation of the location of CP29 in a plant cell, chloroplast.

1.3 Thesis outline

This thesis is organized as follows. In chapters 2 and 3 continuous wave (cw) EPR is employed to examine the influence of a membrane-mimetic agent on the aggregation of the A β peptide. In chapter 4 the influence of shorter fragments of the A β peptide on the aggregation of the full-length A β is investigated. In chapter 5 we investigate the fibril fold of the α S protein with pulsed EPR. Chapter 6 describes the structure of the long flexible N-terminus of the light-harvesting antenna protein CP29. In the final chapter we present the EPR characterization of peptides with one or two rigidly-attached spin labels as models for studying spin-spin interaction in distance measurements.

Reference List

- [1] A. L. Lehninger, D. L. Nelson, Cox M.M., *Lehninger principles of biochemistry*, 4th ed. W.H. Freeman, New York, **2005**.
- [2] L.J.Berliner, J.Grunwald, H.O.Hankovszky, K.Hideg, *Analytical Biochemistry* **1982**, *119* 450-455.
- [3] W.L.Hubbell, C.Altenbach, *Current Opinion in Structural Biology* **1994**, *4* 566-573.
- [4] W.L.Hubbell, H.S.Mchaourab, C.Altenbach, M.A.Lietzow, *Structure* **1996**, *4* 779-783.
- [5] W.L.Hubbell, D.S.Cafiso, C.Altenbach, *Nat.Struct.Biol.* **2000**, *7* 735-739.
- [6] H.S.Mchaourab, M.A.Lietzow, K.Hideg, W.L.Hubbell, *Biochemistry* **1996**, *35* 7692-7704.
- [7] H.J.Steinhoff, *Frontiers in Bioscience* **2002**, *7* C97-C110.
- [8] P.P.Borbat, E.R.Georgieva, J.H.Freed, *J.Phys.Chem.Lett.* **2013**, *4* 170-175.
- [9] G.Jeschke, *Annu.Rev.Phys.Chem.* **2012**, *63* 419-446.
- [10] O.Schiemann, T.F.Prisner, *Q.Rev.Biophys.* **2007**, *40* 1-53.
- [11] P. G. Fajer, in *Encyclopedia of Analytical Chemistry* Ed.: R.A.Meyers, John Wiley & Sons Ltd, Chichester, 2000, **2000**, p. pp. 5725-5761.
- [12] P.G.Fajer, *Journal of Physics-Condensed Matter* **2005**, *17* S1459-S1469.
- [13] G.Jeschke, *Chemphyschem* **2002**, *3* 927-932.
- [14] Atherton N.M., *Principles of Electron Spin Resonance*, Hellis Horwood Limited: Chichester, **1993**.
- [15] John A.Weil, James R.Bolton, *Electron Paramagnetic Resonance, Elementary Theory and Practical Applications*, 2nd ed. Wiley-Interscience, A John Wiley & Sons, Inc., **2007**.
- [16] R.Owenius, M.Engstrom, M.Lindgren, M.Huber, *Journal of Physical Chemistry A* **2001**, *105* 10967-10977.
- [17] Heminga M.A., Berliner L.J., *ESR Spectroscopy in Membrane Biophysics*, Springer, **2007**.
- [18] V.Monaco, F.Formaggio, M.Crisma, C.Toniolo, P.Hanson, G.Millhauser, C.George, J.R.Deschamps, J.L.Flippen-Anderson, *Bioorg.Med.Chem.* **1999**, *7* 119-131.
- [19] V.Monaco, F.Formaggio, M.Crisma, C.Toniolo, P.Hanson, G.L.Millhauser, *Biopolymers* **1999**, *50* 239-253.
- [20] S.Stoll, A.Schweiger, *Journal of Magnetic Resonance* **2006**, *178* 42-55.
- [21] A.Der-Sarkissian, C.C.Jao, J.Chen, R.Langen, *J.Biol.Chem.* **2003**, *278* 37530-37535.
- [22] S.Bohme, H.J.Steinhoff, J.P.Klare, *Spectroscopy-An International Journal* **2010**, *24* 283-288.
- [23] G.Jeschke, A.Bender, H.Paulsen, H.Zimmermann, A.Godt, *J.Magn Reson.* **2004**, *169* 1-12.
- [24] G.Jeschke, G.Panek, A.Godt, A.Bender, H.Paulsen, *Applied Magnetic Resonance* **2004**, *26* 223-244.
- [25] G.Jeschke, V.Chechik, P.Ionita, A.Godt, H.Zimmermann, J.Banham, C.R.Timmel, D.Hilger, H.Jung, *Applied Magnetic Resonance* **2006**, *30* 473-498.
- [26] S.Kumar, S.K.Mohanty, J.B.Udgaonkar, *J.Mol.Biol.* **2007**, *367* 1186-1204.
- [27] J.Greenwald, R.Riek, *Structure* **2010**, *18* 1244-1260.
- [28] L.C.Serpell, C.C.Blake, P.E.Fraser, *Biochemistry* **2000**, *39* 13269-13275.
- [29] E.Herczenik, M.F.Gebbink, *FASEB J.* **2008**, *22* 2115-2133.
- [30] P.K.Auluck, G.Caraveo, S.Lindquist, *Annu.Rev.Cell Dev.Biol.* **2010**, *26* 211-233.
- [31] R.J.Caselli, T.G.Beach, R.Yaari, E.M.Reiman, *J.Clin.Psychiatry* **2006**, *67* 1784-1800.
- [32] K.Chopra, S.Misra, A.Kuhad, *Expert.Opin.Ther.Targets.* **2011**, *15* 535-555.
- [33] R.Jakob-Roetne, H.Jacobsen, *Angew.Chem.Int.Ed Engl.* **2009**, *48* 3030-3059.
- [34] E.Portelius, N.Mattsson, U.Andreasson, K.Blennow, H.Zetterberg, *Curr.Pharm.Des* **2011**, *17* 2594-2602.
- [35] D.J.Selkoe, *Ann.Intern.Med.* **2004**, *140* 627-638.
- [36] J.L.Cummings, *N.Engl.J.Med.* **2004**, *351* 56-67.
- [37] D.J.Selkoe, *Physiol Rev.* **2001**, *81* 741-766.
- [38] E.Portelius, G.Brinkmalm, A.Tran, U.Andreasson, H.Zetterberg, A.Westman-Brinkmalm, K.Blennow, A.Ohrfelt, *Exp.Neurol.* **2010**, *223* 351-358.
- [39] M.Gralle, S.T.Ferreira, *Prog.Neurobiol.* **2007**, *82* 11-32.
- [40] A.Awasthi, Y.Matsunaga, T.Yamada, *Exp.Neurol.* **2005**, *196* 282-289.

-
- [41] E.Portelius, H.Zetterberg, U.Andreasson, G.Brinkmalm, N.Andreasen, A.Wallin, A.Westman-Brinkmalm, K.Blennow, *Neurosci.Lett.* **2006**, *409* 215-219.
- [42] J.Hardy, D.J.Selkoe, *Science* **2002**, *297* 353-356.
- [43] H.A.Lashuel, D.Hartley, B.M.Petre, T.Walz, P.T.Lansbury, Jr., *Nature* **2002**, *418* 291.
- [44] N.Yamamoto, K.Hasegawa, K.Matsuzaki, H.Naiki, K.Yanagisawa, *J.Neurochem.* **2004**, *90* 62-69.
- [45] V.Rangachari, D.K.Reed, B.D.Moore, T.L.Rosenberry, *Biochemistry* **2006**, *45* 8639-8648.
- [46] V.Rangachari, B.D.Moore, D.K.Reed, L.K.Sonoda, A.W.Bridges, E.Conboy, D.Hartigan, T.L.Rosenberry, *Biochemistry* **2007**, *46* 12451-12462.
- [47] S.I.Shaikh, H.Verma, *Indian J.Anaesth.* **2011**, *55* 228-234.
- [48] A.Samii, J.G.Nutt, B.R.Ransom, *Lancet* **2004**, *363* 1783-1793.
- [49] L.L.Venda, S.J.Cragg, V.L.Buchman, R.Wade-Martins, *Trends Neurosci.* **2010**, *33* 559-568.
- [50] C.W.Hung, Y.C.Chen, W.L.Hsieh, S.H.Chiou, C.L.Kao, *Ageing Res.Rev.* **2010**, *9 Suppl 1* S36-S46.
- [51] P.J.Kahle, M.Neumann, L.Ozmen, V.Muller, H.Jacobsen, A.Schindzielorz, M.Okochi, U.Leimer, P.H.van Der, A.Probst, E.Kremmer, H.A.Kretzschmar, C.Haass, *J.Neurosci.* **2000**, *20* 6365-6373.
- [52] S.Yu, X.Li, G.Liu, J.Han, C.Zhang, Y.Li, S.Xu, C.Liu, Y.Gao, H.Yang, K.Ueda, P.Chan, *Neuroscience* **2007**, *145* 539-555.
- [53] W.S.Davidson, A.Jonas, D.F.Clayton, J.M.George, *J.Biol.Chem.* **1998**, *273* 9443-9449.
- [54] D.Eliezzer, E.Kutluay, R.Bussell, Jr., G.Browne, *J.Mol.Biol.* **2001**, *307* 1061-1073.
- [55] B.I.Giasson, I.V.J.Murray, J.Q.Trojanowski, V.M.Y.Lee, *Journal of Biological Chemistry* **2001**, *276* 2380-2386.
- [56] H.Miake, H.Mizusawa, T.Iwatsubo, M.Hasegawa, *J.Biol.Chem.* **2002**, *277* 19213-19219.
- [57] M.Mihajlovic, T.Lazaridis, *Proteins* **2008**, *70* 761-778.
- [58] M.Drescher, F.Godschalk, G.Veldhuis, B.D.van Rooijen, V.Subramaniam, M.Huber, *Chembiochem* **2008**, *9* 2411-2416.
- [59] M.Drescher, B.D.van Rooijen, G.Veldhuis, V.Subramaniam, M.Huber, *J.Am.Chem.Soc.* **2010**, *132* 4080-4082.
- [60] M.Drescher, M.Huber, V.Subramaniam, *Chembiochem* **2012**.
- [61] M.Chen, M.Margittai, J.Chen, R.Langen, *J.Biol.Chem.* **2007**, *282* 24970-24979.
- [62] G.Comellas, L.R.Lemkau, A.J.Nieuwkoop, K.D.Kloepper, D.T.Ladror, R.Ebisu, W.S.Woods, A.S.Lipton, J.M.George, C.M.Rienstra, *J.Mol.Biol.* **2011**, *411* 881-895.
- [63] H.Heise, W.Hoyer, S.Becker, O.C.Andronesi, D.Riedel, M.Baldus, *Proc.Natl.Acad.Sci.U.S.A* **2005**, *102* 15871-15876.
- [64] M.Vilar, H.T.Chou, T.Luhrs, S.K.Maji, D.Riek-Loher, R.Verel, G.Manning, H.Stahlberg, R.Riek, *Proc.Natl.Acad.Sci.U.S.A* **2008**, *105* 8637-8642.
- [65] X.Pan, M.Li, T.Wan, L.Wang, C.Jia, Z.Hou, X.Zhao, J.Zhang, W.Chang, *Nat.Struct.Mol.Biol.* **2011**, *18* 309-315.

CHAPTER 2

THE EFFECT OF A MEMBRANE MIMICKING DETERGENT ON AMYLOID β AGGREGATION

OVERVIEW AND THE REGIME OF HIGH DETERGENT CONCENTRATION

The aggregation of amyloid β ($A\beta$) peptide into fibrils and plaques is the chief indicator of Alzheimer's disease. Specific interest in oligomers stems from the suggestion that small, oligomeric aggregates and protofibrils, rather than the fully formed fibrils could be responsible for the toxicity of the $A\beta$ peptide. We investigate the potential of Electron Paramagnetic Resonance (EPR) spectroscopy to detect early stages of $A\beta$ peptide aggregation in the presence of the sodium dodecyl sulfate (SDS) detergent as a membrane mimicking agent. We have labeled the $A\beta_{40}$ peptide variant, which contains an N-terminal cysteine with the MTS spin label ((1-oxyl-2,2,5,5-tetramethylpyrroline-3-methyl) methanethiosulfonate) and monitor the effect of different concentrations of SDS on the aggregation of the $A\beta$ peptide. Continuous wave, 9 GHz EPR reveals that upon increasing the SDS concentration a transition from oligomers to a state in which a monomeric peptide binds to a micelle occurs. In the hitherto difficult to access area of low SDS concentrations we postulate a change from $A\beta$ oligomers to $A\beta$ -SDS complexes. The EPR approach enables us to monitor the changes occurring in the reaction mixture in the presence of different amounts of SDS on the time scale of aggregation.

2.1 Introduction

The amyloid β (A β) peptide is important in the context of Alzheimer's disease, where it is one of the major components of the fibrils forming amyloid plaques ^[1-6]. The peptide derives from misprocessing of the amyloid precursor protein (APP) and comprises a part of the presumed transmembrane section of APP ^[3,5-9]. In solution, the peptide is disordered and, especially at high concentration its tendency to aggregate into fibrils is high ^[10]. In the fibrils it adopts a parallel, β -sheet structure ^[3,11].

In vitro studies of the properties of A β are essential to understand its behavior at a molecular level. Such studies should also address the aggregation process, in particular, since early aggregates such as oligomers, rather than fully formed plaques, are discussed as toxic agents ^[5,8,12-16]. Furthermore, agents that can influence aggregation are important, and of those, membrane mimics are particularly relevant, because the hydrophobic part of A β suggests a possible membrane activity of the peptide. One such agent is the sodium dodecyl sulfate (SDS) detergent ^[17-21].

The aggregation of A β under the influence of SDS, and with respect to the SDS concentration has identified two regimes ^[20]. At low concentrations of SDS or low SDS to peptide ratios (D/P), evidence for aggregates was found. These aggregates appeared to have a β -sheet component ^[22-27], suggesting aggregates which possess the secondary structure element of A β in the fibrils. In this regime, solution NMR methods are plagued by the absence of signals ^[20], which together with the known heterogenic character of A β samples has precluded further structural characterization. At higher SDS concentrations, the picture becomes clearer. In the concentration range around the critical micelle concentration (CMC) of SDS in water ^[22-25,27] and above, A β is found to have an α -helical conformation. A detailed study, using solution NMR ^[20,28] revealed that A β could be monomeric and embedded in an SDS micelle, a model that is supported also by small-angle X-ray and neutron scattering, FTIR, and CD spectroscopy ^[16,17,20,28-34].

In the present study, we use spin-label EPR to learn more about the aggregation process in the presence of SDS. There are several reports about the use of spin-label EPR in A β research ^[35-37]. The most relevant in the present context is that signatures of the oligomeric A β peptide can be detected by the spin-label EPR methodology ^[38], suggesting this technique as a possible tool to detect the effect of SDS on the aggregation of A β peptide. We employ spin-label EPR in combination with diamagnetic dilution to avoid line broadening by spin-spin interactions ^[3,38,39]. Diamagnetic dilution refers to diluting the spin-labeled A β peptide (SL-A β) with

unlabeled A β peptide (wild type A β). We monitor the effect of SDS on the aggregation of the A β peptide at different D/P ratios. The ratios cover the entire range of SDS concentrations and were chosen to overlap with those employed by Wahlström et al. ^[20]. The present study shows that by EPR information about A β aggregation at a wide range of SDS concentrations can be obtained. We propose that A β aggregates, present in the absence of SDS, are successively replaced by peptide-detergent aggregates at low SDS concentrations. At SDS concentrations above the CMC only one species is present, which we assign to a monomeric, micelle bound form of A β .

2.2 Materials and methods

The A β 40 peptide and its cysteine-A β variant (H-Cys-Asp-Ala-...-Val-OH) were purchased from AnaSpec (purity > 95 %), the solvent DMSO was purchased from Biosolve (purity 99.8 %). The MTS spin label ((1-oxy-2,2,5,5-tetramethylpyrrolidine-3-methyl) methanethiosulfonate) was purchased from Toronto Research Chemicals Inc. (Brisbane Rd., North York, Ontario, Canada, M3J 2J8). Spin labeling was performed and the purified spin-labeled A β was analyzed by liquid chromatography as described previously ^[38]. The peptide was lyophilized and stored in the freezer (-20°C) until used.

2.2.1 Sample preparation protocol

Seven different A β sample conditions, differing in SDS concentrations were investigated. The total concentration of peptide was kept constant at 0.55 mM. The peptide was a mixture of wild type A β and SL-A β that contained 14 % SL-A β , resulting in diamagnetically diluted samples as reported before ^[38]. In contrast to the previous protocol ^[38], we prepared the A β samples using a procedure, which involves predissolution of the peptide in dilute base solution ^[20,40-42]. This procedure was designed to avoid peptide aggregation in the starting solution.

Accordingly, the A β peptides were predissolved in NaOH solution (10 mM, pH 11) with sonication for one minute in an ice bath at twice the desired final concentration, i.e., at 1.1 mM total A β concentration. The desired amount of SDS was dissolved in potassium phosphate buffer (20 mM, pH 7.4). The basic solution of A β peptides (1.1 mM) was combined with the potassium phosphate buffer solution (20 mM, pH 7.4) to reach the final desired peptide concentration and the proper D/P molar ratio for each sample (for D/P ratios see table 2.1). This step was followed by another one minute sonication in an ice bath. The final pH was adjusted to pH 7.4. The entire sample preparation was performed on ice. All samples were prepared and measured at least twice.

Table 2.1 Correspondence of SDS content of samples. Ratio of SDS detergent to A β peptide (D/P) and absolute SDS concentrations investigated.

D/P ratio	SDS [mM]
0	0
2.7	1.5
5.4	3
7.3	4
12.7	7
65.4	36
130.9	72

2.2.2 EPR experiments

For room temperature measurements, samples of 10-15 μ l peptide solution were drawn into Blaubrand 50 μ l capillaries. Often, a white precipitate was observed, indicating aggregation. In cases where a white precipitate was observed, the sample height was carefully adjusted in order to be sensitive to that part of the solution. The X-band continuous-wave (cw) EPR measurements have been performed using an ELEXSYS E680 spectrometer (Bruker, Rheinstetten, Germany) equipped with a rectangular cavity. A modulation frequency of 100 kHz was used. Measurements were done at temperature of 20°C, using 6.331 mW of microwave power and a modulation amplitude of 1.4 G. The large modulation amplitude helps to obtain a better signal-to-noise ratio for broad lines. The accumulation time for the spectra was 40 minutes per spectrum.

2.2.3 The amount of spin label in different samples

For a quantitative comparison of samples, we need to investigate the actual amount of spin label in each sample. This amount was determined by double integration of the first-derivative EPR spectrum, with the SL-A β stock solution as a reference. The amount of spin label for the samples with different concentrations of SDS was at least 86 % compared to the stock solution. The uncertainties of this method, determined by multiple independent analyses of the same data, are around 20 % due to difficulties with the base-line correction of the spectra. Within this error margin, the amount of spin-labeled peptides in all samples is identical.

2.2.4 Simulations of EPR spectra, interpretation of the rotation-correlation time

The spectra were simulated using Matlab (version 7.11.0.584, Natick, Massachusetts, U.S.A) and the EasySpin package^[43]. The following tensor values were used for all simulations: $g = [2.00906, 2.00687, 2.00300]$ ^[38,44] and $A_{xx} = A_{yy} = 13$ MHz in

buffer. For the fast and medium components, different A_{zz} values were used than for the slow component, as discussed before ^[38]. For each fraction over-modulation effects were taken into account in EasySpin. Usually a superposition of one to three components was required to simulate the spectra. In all cases, isotropic rotation of the spin label was sufficient to reproduce the line-shape observed. From the simulation of the EPR line-shape, the rotation-correlation time, τ_r , of the spin-labeled peptide as well as the corresponding amount of each spectral component was obtained ^[45].

We interpreted τ_r with the Stokes-Einstein equation, which implies a spherical approximation for the volume ^[38]:

$$\tau_r = \frac{4\pi\eta\alpha^3}{3kT} = \frac{\eta}{kT} V_{EPR} \quad (2.1)$$

The Boltzman constant, k , and solvent viscosity, η , at a specified temperature, T , are required to obtain the hydrodynamic radius, α . According to equation (2.1), the volume, V_{EPR} , of the particle is linearly correlated with the τ_r of the spin-labeled peptide. The volumes derived are referred to as V_{EPR} in the text. The volume V_{EPR} derived from τ_r is strongly affected by the mobility of the nitroxide group of the spin label and the rotation of the spin label around the linker bond can make this correlation time significantly smaller than that of the aggregate.

2.3 Results

We have applied X-band cw EPR to monitor the effects of the presence of SDS on the A β peptide. The main observable is the line-shape of the EPR spectra, which, under the conditions employed (diamagnetic dilution), reflects the mobility of the spin label attached to the cysteine variant of A β . Figure 2.1 shows the spectra of the monomeric SL-A β and of diamagnetically diluted SL-A β in three samples with different amounts of SDS measured at room temperature. In the following we refer to the diamagnetically diluted SL-A β as SL-A β unless otherwise stated.

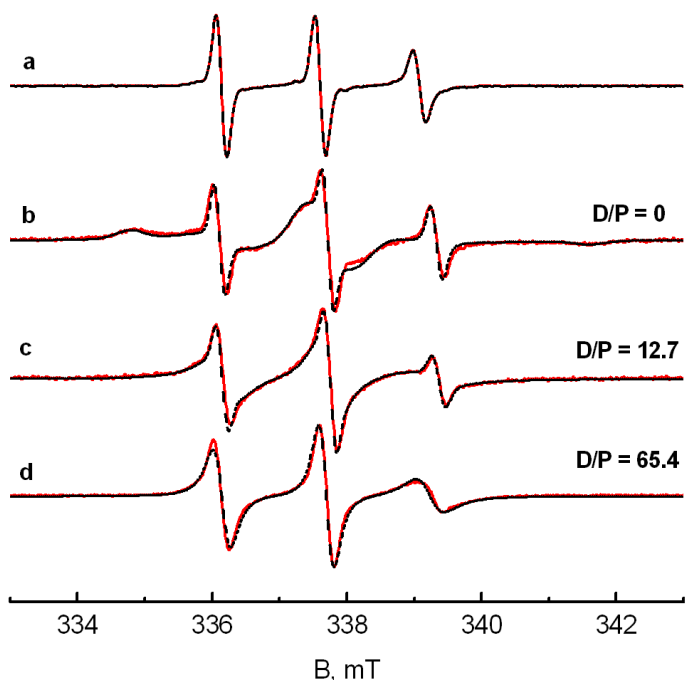


Figure 2.1 Room temperature EPR spectra of monomeric pure SL-A β in a: DMSO, and SL-A β obtained from samples with three different D/P ratios: b: D/P = 0, c: D/P = 12.7 and, d: D/P = 65.4. Black line: experiment, red line: simulation.

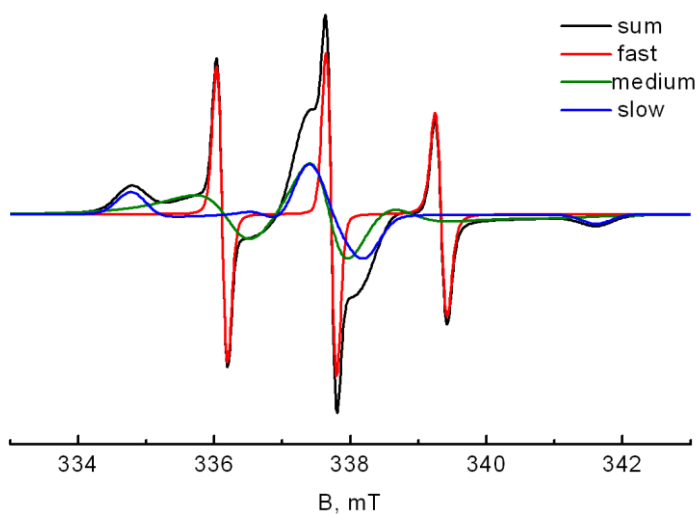


Figure 2.2 Simulation of the EPR spectrum of SL-A β at D/P = 0 with three components: red line fast, green line medium, and blue line slow component.

The EPR spectrum of monomeric A β (figure 2.1.a) has three narrow lines. Comparison of figure 2.1.a and b shows that in the absence of SDS (D/P = 0), the lines are broadened and additional lines are observed compared to the spectra of the monomeric peptide (figure 2.1.a), which suggests a superposition of different spectral components. Figure 2.2 shows these components as obtained from a simulation of the EPR spectrum that is shown in figure 2.1.b. The spectrum can be simulated by three components^[38], which, in the remainder of the text, we refer to as fast, medium and slow. The relative amount of these components (table 2.2) is similar to that obtained before^[38] except for an increase in the amount of the fast fraction from 5 % to 10 % (see Discussion). Each component is characterized by a rotation-correlation time and the amount by which this component contributes to the spectrum (table 2.2).

Table 2.2 EPR parameters obtained from the simulation of cw EPR spectra of SL-A β samples. Given are: τ_r , rotation-correlation time, A_{zz} , the hyperfine splitting along the z-direction, lw , the component line-width of the simulation, and % stands for the contribution of the component to the total spectrum.

	fast				medium				slow			
D/P	τ_r (ns)	A_{zz} (MHz)	lw (mT)	%	τ_r (ns)	A_{zz} (MHz)	lw (mT)	%	τ_r (ns)	A_{zz} (MHz)	lw (mT)	%
0	0.19 ± 0.02	110	0.14	10 ± 2.0	2.55 ± 0.35	110	0.32	51 ± 2	> 50	95	0.50	39.0 ± 2.0
2.7	0.43 ± 0.02	110	0.14	2.5 ± 0.5	4.80 ± 0.40	110	0.32	64 ± 4	> 50	95	0.50	33.5 ± 2.5
5.4	0.43 ± 0.02	110	0.14	2.5 ± 0.5	4.65 ± 0.55	110	0.32	75 ± 3	> 50	95	0.50	22.5 ± 2.5
7.3	0.19 ± 0.02	110	0.14	10.0 ± 2.0	1.76 ± 0.16	110	0.14	90 ± 2	-	-	-	-
12.7	0.19 ± 0.02	110	0.14	7.0 ± 2.0	1.55 ± 0.08	110	0.14	92 ± 3	-	-	-	-
65.4	-	-	-	-	0.93 ± 0.03	109	0.06	100	-	-	-	-
130.9	-	-	-	-	0.93 ± 0.03	109	0.06	100	-	-	-	-

Figure 2.1.c shows the spectrum of a sample with an intermediate ratio of D/P (D/P = 12.7). This spectrum was simulated using two components (fast and medium) with the parameters given in table 2.2. The slow component disappears gradually in the range of SDS concentrations from 3 to 7 mM, D/P = 5.4 to 12.7. At even higher concentrations of SDS (above 36 mM, D/P = 65.4) the simulation shows that the line-shape (figure 2.1.d) is fully described by a single species. The corresponding τ_r of this species is the same for the D/P ratios 65.4 and 130.9. The rotation-correlation time of the single species observed at high SDS concentrations ($\tau_r = 0.93$ ns) is larger than the τ_r of the fast component ($\tau_r = 0.19$ ns) and smaller than that of

the medium component in the absence of SDS ($D/P = 0$, $\tau_r = 2.55$ ns). In the following we refer to this species as the high-SDS species.

To test for spin-spin interaction we measured the high-SDS species in a pure SL-A β sample. The result is shown in figure 2.3. There is no difference between the diamagnetically diluted and the non-diluted sample, showing the absence of spin-spin interaction of A β in the high SDS regime.

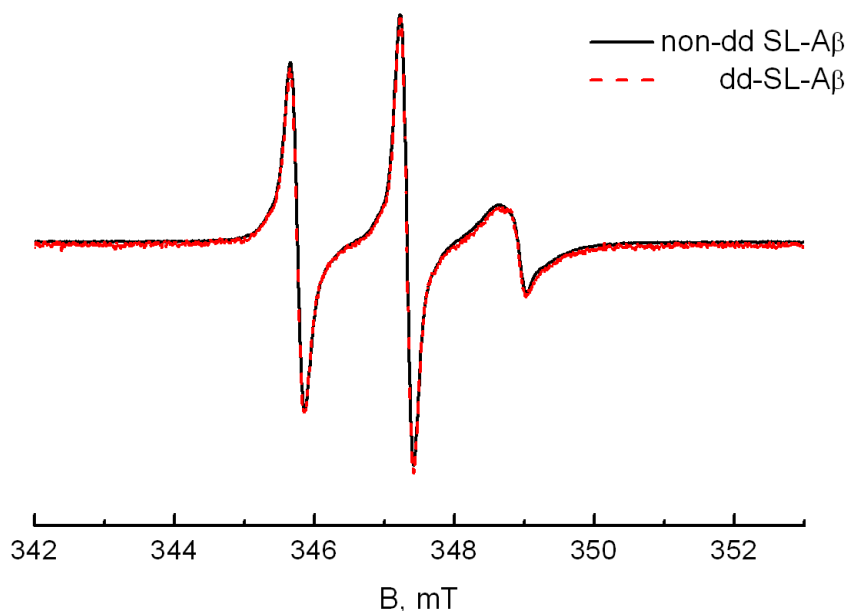


Figure 2.3 Room temperature EPR spectra of high-SDS-A β samples measured at a D/P ratio of 130.9. Black line: non-diluted A β sample: non-dd SL-A β . Red line: diamagnetically diluted A β sample: dd-SL-A β .

2.3.1 Effect of SDS on the amount of different components

An important parameter in the spectral simulation is the contribution of different components to each spectrum. In figure 2.4, the amount of different mobility components is plotted versus the D/P ratios ranging from 0 to 130.9. In the absence of SDS, at $D/P = 0$, the spectrum is composed of almost equal amounts of the slow and the medium component, and a small fraction (10 %) of the fast component. At low D/P ratios (between $D/P = 0$ and 12.7), the amount of the fast component fluctuates but never reaches more than 12 %. At D/P ratios larger than 12.7 the fast component disappears. There is a gradual increase in the amount of the medium component between $D/P = 0$ and 12.7. Above $D/P = 12.7$ (i.e., 7 mM SDS) which is

close to the critical micelle concentration of SDS ^[22-25,27], the medium component increases to its final value of 100 %. As shown in figure 2.4, upon increasing the D/P ratio to about D/P = 7.3, there is a drop in the amount of the slow component. At D/P ratios larger than 7.3 the slow component has disappeared.

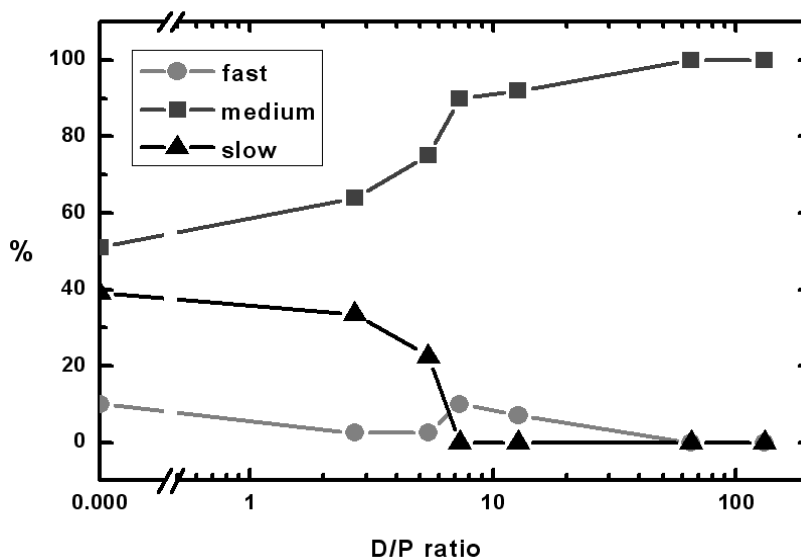


Figure 2.4 Amount of the spectral components as a function of the D/P ratios.

2.3.2 The size of aggregates at different concentrations of SDS

According to the Stokes-Einstein equation, equation (2.1), the volume of the particle has a linear dependence on τ_r (see materials and methods). From τ_r we can determine the EPR derived volume of the aggregates, V_{EPR} , (see materials and methods). For the volume of the slow component ($\tau_r > 50$ ns), only a lower limit of $5 \cdot 10^4 \text{ \AA}^3$ could be given because this component is immobile on the time scale of the EPR experiment. For the fast rotating fraction of the sample with D/P = 0, a τ_r of 0.19 ns is obtained. Using the viscosity of water of $\eta = 1.002 \cdot 10^{-3} \text{ (N}\cdot\text{s}\cdot\text{m}^{-2})$ at 20° C ^[46], a volume of 180 \AA^3 results, which is close to the volume of 126 \AA^3 obtained from the τ_r of A β in DMSO ($\eta = 1.996 \cdot 10^{-3} \text{ N}\cdot\text{s}\cdot\text{m}^{-2}$ ^[46], $\tau_r = 0.26$ ns) in which the peptide is in the monomeric form. Following Sepkhanova et al., the fast component is assigned to the monomeric peptide ^[38].

2.4 Discussion

In the present study we have used spin-label EPR to investigate the effect of SDS on the aggregation process of the A β peptide. In the absence of SDS, three components are found, which, according to their mobility characteristics, are referred to as the fast, medium, and slow components. We attribute the fast component to monomeric A β and the two others to aggregated forms of A β , as described before ^[38]. We ascribe the larger amount of monomeric A β (10 % vs 5 % in the previous study) observed in the present study to the different preparation protocol ^[20,40,42], a protocol that was designed to increase the amount of monomeric A β . The fraction of monomeric A β never reaches values higher than 12 %, even considering the sample-to-sample variation. From this observation, we conclude that the largest portion of the sample is aggregated. This observation is in good agreement with previous reports ^[10,20], which shows that at the A β concentrations used here aggregates are present.

2.4.1 The high SDS concentration species of A β

At high concentrations of SDS, well above CMC ^[22-27], the sample is composed of a single species, referred to as the high-SDS-species. This species makes up at least 80 % of the total peptide in the sample (see materials and methods) and is the only species we observe. In that state, the A β must be monomeric because of the absence of spin-spin interaction in the spectra of pure SL-A β samples (figure 2.3 and appendix A). This species has a molecular volume V_{EPR} that is larger than the V_{EPR} of the monomeric A β . The V_{EPR} of the high-SDS species is much smaller than the volume of an SDS micelle ^[22,47]. Previously, it was proposed that the species predominant at high SDS concentrations is a monomeric A β , solubilized in an SDS micelle ^[17,20,28,29,31,32,34,48]. This proposal is consistent with the data obtained by EPR. The finding that the size of the high-SDS species is larger than that of the monomeric A β is consistent with micelle binding, because the volume increases by the attachment of A β to the micelle. The fact that V_{EPR} is smaller than the volume of the SDS micelle is attributed to the local mobility of the spin label. Also, owing to the local mobility of the spin label, V_{EPR} is significantly smaller than the volume of the high-SDS species ($23 - 132 \cdot 10^3 \text{ \AA}^3$) derived from NMR results ^[20,32,34,48]. The last issue to be resolved for the high-SDS species is that EPR suggests the sample to be homogenous, whereas the NMR-titration data show that at similar D/P ratios, the sample is heterogeneous, and only a fraction of about 20 % of the sample is visible to the NMR, which shows that only that fraction is in the monomeric SDS-micelle bound form ^[20]. Several explanations are offered for the absence of NMR signals for the remaining 80 % of the peptide, amongst which peptide aggregates ^[20]. For

the EPR sample we can exclude a mixture of aggregates and monomers because only a single species is observed and A β -A β interaction is not detected (figure 2.3 and appendix A). Besides other explanations given for the heterogeneity of the high-SDS NMR samples ^[20], differences between the EPR and NMR results could be caused by the respective measurement conditions. It has been shown that the absolute concentrations of SDS and A β could influence the formation of the A β -micelle complex or peptide aggregation, because apparently there is competition between the association of A β with micelles and A β with A β to form aggregated peptide ^[17]. The peptide concentration in the EPR experiments is higher than in NMR. Consequently, the critical micelle concentration of SDS is reached at lower D/P ratios than in the NMR experiments. This could help to favorably influence the equilibrium between A β -A β and A β -SDS interaction and result in a larger fraction of monomeric A β bound to the micelle in the EPR experiment. Furthermore, in the EPR sample preparation the total amount of SDS is added directly to the peptide, rather than in titrating steps as in NMR ^[20]. Perhaps the presence of high concentrations of SDS under the conditions of the EPR measurement is more efficient to prevent peptide aggregation.

2.4.2 A β at intermediate SDS concentrations

In contrast to the interpretation of the high-SDS-species, much less is known so far about the state of peptide at intermediate concentrations of SDS. The disappearance of NMR signals and the β -sheet signatures found in CD and FTIR spectra were attributed to an aggregated form of A β ^[20]. By EPR, in the intermediate SDS concentration regime (D/P = 2.7), τ_r of the medium component (table 2.2) is larger than in the absence of SDS, which could be due to an increase in the size of existing aggregates or to detergent molecules that bind to A β . In the former case, such aggregates are most likely formed at the expense of the very large aggregates present in the slow mobility fraction. Such a redistribution would explain the decreasing amount of A β in the slow fraction with increasing SDS concentration, a fraction that at D/P ratios of 7.3, corresponding to 4 mM SDS, completely disappears. But concomitantly, also the character of the aggregate must change, as also suggested by the decrease in the β -sheet component observed by CD spectroscopy ^[20]. The rotation-correlation time of the medium-mobility fraction changes significantly at D/P ratios between 7.3 and 12.7 to 1/3 of its initial value, which indicates a change in the size of the aggregate and/or the local mobility of the spin label. We speculate that the aggregate changes from an A β -oligomer to a species in which A β interacts with several SDS molecules. The component observed is likely not the micelle bound species, because the transition occurs well

below the CMC of SDS. Almost coinciding with the CMC, at D/P ratios above 12.7 the high-SDS species prevails.

Overall, the present EPR investigation suggests that, starting from low SDS concentrations, a transition from an A β -oligomer to an A β -SDS complex seems to take place. Since this change is accompanied by a loss in β -sheet signature and an increase in α -helix character ^[20], we propose that this is the first step towards the micelle-bound state of A β , in which the peptide is supposed to have an α -helical structure.

The present investigation shows that because of the high sensitivity of EPR to the aggregation state of A β , we can monitor the changes occurring in the reaction mixture in the presence of different amounts of SDS on the time scale of aggregation. We propose an A β -SDS complex at SDS concentrations below the CMC and a micelle-bound monomeric A β state at higher SDS concentrations.

Reference List

- [1] F.Chiti, C.M.Dobson, *Annu.Rev.Biochem.* **2006**, 75 333-366.
- [2] D.G.Lynn, S.C.Meredith, *J.Struct.Biol.* **2000**, 130 153-173.
- [3] M.Margittai, R.Langen, *Q.Rev.Biophys.* **2008**, 41 265-297.
- [4] F.Panza, V.Solfrizzi, V.Frisardi, C.Capurso, A.D'Introno, A.M.Colacicco, G.Vendemiale, A.Capurso, B.P.Imbimbo, *Drugs Aging* **2009**, 26 537-555.
- [5] D.J.Selkoe, *Neuron* **1991**, 6 487-498.
- [6] D.J.Selkoe, *Physiol Rev.* **2001**, 81 741-766.
- [7] M.Gralle, S.T.Ferreira, *Prog.Neurobiol.* **2007**, 82 11-32.
- [8] J.Hardy, D.J.Selkoe, *Science* **2002**, 297 353-356.
- [9] S.Kumar, S.K.Mohanty, J.B.Udgaonkar, *J.Mol.Biol.* **2007**, 367 1186-1204.
- [10] A.Paivio, J.Jarvet, A.Gräslund, L.Lannfelt, A.Westlind-Danielsson, *Journal of Molecular Biology* **2004**, 339 145-159.
- [11] C.J.Barrow, M.G.Zagorski, *Science* **1991**, 253 179-182.
- [12] P.Cizas, R.Budvytyte, R.Morkuniene, R.Moldovan, M.Brocchio, M.Losche, G.Niaura, G.Valincius, V.Borutaite, *Arch.Biochem.Biophys.* **2010**, 496 84-92.
- [13] F.Dulin, I.Callebaut, N.Colloc'h, J.P.Mornon, *Biopolymers* **2007**, 85 422-437.
- [14] N.L.Fawzi, J.F.Ying, D.A.Torchia, G.M.Clore, *Journal of the American Chemical Society* **2010**, 132 9948-9951.
- [15] D.Losic, L.L.Martini, M.I.Aguilar, D.H.Small, *Biopolymers* **2006**, 84 519-526.
- [16] D.J.Tew, S.P.Bottomley, D.P.Smith, G.D.Ciccotosto, J.Babon, M.G.Hinds, C.L.Masters, R.Cappai, K.J.Barnham, *Biophysical Journal* **2008**, 94 2752-2766.
- [17] J.M.Lin, T.L.Lin, U.S.Jeng, Z.H.Huang, Y.S.Huang, *Soft Matter* **2009**, 5 3913-3919.
- [18] B.ONuallain, D.B.Freir, A.J.Nicoll, E.Risse, N.Ferguson, C.E.Herron, J.Collinge, D.M.Walsh, *J.Neurosci.* **2010**, 30 14411-14419.
- [19] V.Rangachari, B.D.Moore, D.K.Reed, L.K.Sonoda, A.W.Bridges, E.Conboy, D.Hartigan, T.L.Rosenberry, *Biochemistry* **2007**, 46 12451-12462.
- [20] A.Wahlström, L.Hugonin, A.Perálvarez-Marín, J.Jarvet, A.Gräslund, *FEBS J.* **2008**, 275 5117-5128.
- [21] S.S.S.Wang, K.N.Liu, T.C.Han, *Biochimica et Biophysica Acta-Molecular Basis of Disease* **2010**, 1802 519-530.
- [22] G.Duplatre, M.F.F.Marques, M.daGracaMiguel, *Journal of Physical Chemistry* **1996**, 100 16608-16612.
- [23] E.Fuguet, C.Rafols, M.Roses, E.Bosch, *Analytica Chimica Acta* **2005**, 548 95-100.
- [24] A.Helenius, K.Simons, *Biochim.Biophys.Acta* **1975**, 415 29-79.
- [25] G.D.Henry, B.D.Sykes, *Nuclear Magnetic Resonance, Pt C* **1994**, 239 515-535.
- [26] P.Mukerjee, K.J.Mysels, P.Kapauan, *Journal of Physical Chemistry* **1967**, 71 4166-&.
- [27] M.Sammalkorpi, M.Karttunen, M.Haataja, *J.Phys.Chem.B* **2007**, 111 11722-11733.
- [28] J.Jarvet, J.Danielsson, P.Damberg, M.Oleszczuk, A.Gräslund, *J.Biomol.NMR* **2007**, 39 63-72.
- [29] M.Coles, W.Bicknell, A.A.Watson, D.P.Fairlie, D.J.Craik, *Biochemistry* **1998**, 37 11064-11077.
- [30] T.A.Pertinhez, M.Bouchard, R.A.Smith, C.M.Dobson, L.J.Smith, *FEBS Lett.* **2002**, 529 193-197.
- [31] V.Rangachari, D.K.Reed, B.D.Moore, T.L.Rosenberry, *Biochemistry* **2006**, 45 8639-8648.
- [32] H.Y.Shao, S.C.Jao, K.Ma, M.G.Zagorski, *Journal of Molecular Biology* **1999**, 285 755-773.
- [33] D.V.Waterhous, W.C.Johnson, Jr., *Biochemistry* **1994**, 33 2121-2128.
- [34] M.G.Zagorski, L.M.Hou, *Abstracts of Papers of the American Chemical Society* **2002**, 223 C29.
- [35] M.Grimaldi, M.Scrima, C.Esposito, G.Vitiello, A.Ramunno, V.Limongelli, G.D'Errico, E.Novellino, A.M.D'Ursi, *Biochim.Biophys.Acta* **2010**, 1798 660-671.
- [36] F.Mito, T.Yamasaki, Y.Ito, M.Yamato, H.Mino, H.Sadasue, C.Shirahama, K.Sakai, H.Utsumi, K.Yamada, *Chemical Communications* **2011**, 47 5070-5072.
- [37] G.Vitiello, M.Grimaldi, A.Ramunno, O.Ortona, G.De Martino, A.M.D'Ursi, G.D'Errico, *Journal of Peptide Science* **2010**, 16 115-122.

- [38] I.Sepkhanova, M.Drescher, N.J.Meeuwenoord, R.W.A.L.Limpens, R.I.Koning, D.V.Filippov, M.Huber, *Applied Magnetic Resonance* **2009**, 36 209-222.
- [39] F.Scarpelli, M.Drescher, T.Rutters-Meijneke, A.Holt, D.T.Rijkers, J.A.Killian, M.Huber, *J.Phys.Chem.B* **2009**, 113 12257-12264.
- [40] Y.Fezoui, D.M.Hartley, J.D.Harper, R.Khurana, D.M.Walsh, M.M.Condron, D.J.Selkoe, P.T.Lansbury, Jr., A.L.Fink, D.B.Teplow, *Amyloid* **2000**, 7 166-178.
- [41] Y.Fezoui, D.M.Hartley, D.M.Walsh, D.J.Selkoe, J.J.Osterhout, D.B.Teplow, *Nat.Struct.Biol.* **2000**, 7 1095-1099.
- [42] L.Hou, H.Shao, Y.Zhang, H.Li, N.K.Menon, E.B.Neuhaus, J.M.Brewer, I.J.Byeon, D.G.Ray, M.P.Vitek, T.Iwashita, R.A.Makula, A.B.Przybyla, M.G.Zagorski, *J.Am.Chem.Soc.* **2004**, 126 1992-2005.
- [43] S.Stoll, A.Schweiger, *Journal of Magnetic Resonance* **2006**, 178 42-55.
- [44] S.Steigmler, M.Börsch, P.Gräber, M.Huber, *Biochim.Biophys.Acta* **2005**, 1708 143-153.
- [45] W.L.Hubbell, H.S.Mchaourab, C.Altenbach, M.A.Lietzow, *Structure* **1996**, 4 779-783.
- [46] L.M.Omota, O.Iulian, O.Ciocirlan, I.Nita, *Revue Roumaine de Chimie* **2008**, 53 977-+.
- [47] F.Bockstahl, E.Pachoud, G.Duplatre, I.Billard, *Chemical Physics* **2000**, 256 307-313.
- [48] H.Y.Shao, S.C.Jao, M.G.Zagorski, *Abstracts of Papers of the American Chemical Society* **1997**, 213 13-MEDL.

CHAPTER 3

INTERACTION OF THE AMYLOID β PEPTIDE WITH A MEMBRANE MIMICKING DETERGENT

THE REGIME OF SUB-MICELLAR DETERGENT CONCENTRATION

The amyloid β (A β) peptide is important in the context of Alzheimer's disease, where it is one of the major components of the fibrils forming amyloid plaques. Agents that can influence aggregation are important, and of those, membrane mimics are particularly relevant, because the hydrophobic part of A β suggests a possible membrane activity of the peptide. We employed spin-label EPR to learn about the aggregation process of A β in the presence of the sodium dodecyl sulfate (SDS) detergent as a membrane mimicking agent. In chapter 2 we focus on the overall effect of SDS on the A β using a spin label at the N-terminus as a probe. Thereby information on the state of A β at high-SDS concentration, i.e., above the critical micelle concentration (CMC) is obtained. In the present chapter we explore the aggregation behavior using two different positions of the spin label. By comparing the two label positions the effect of local mobility of the spin label is eliminated, thereby, we learn about the A β aggregation in the SDS concentration regime below the CMC. We demonstrate that at low SDS concentrations the N-terminus of A β participates in the solubilization by being located at the particle/water interface. At higher SDS concentrations an SDS-solubilized state that is a precursor to the one A β /micelle state above the CMC of SDS prevails. This study reveals the unique potential of EPR in studying the A β aggregation.

3.1 Introduction

The aggregation of the amyloid β (A β) peptide to fibrils and plaques is the chief indicator of Alzheimer's disease ^[1-7]. The potent pathologic effects of A β oligomers provide a compelling reason for elucidating the mechanism(s) leading to the transformation of monomeric A β into toxic oligomers and ultimately larger aggregates ^[8-10]. In this context agents that can influence aggregation are important, and of those, membrane mimics are particularly relevant, because the hydrophobic part of A β suggests a possible membrane activity of the peptide. One such agent is the sodium dodecyl sulfate (SDS) detergent ^[10-14]. Previous studies addressed the aggregation of A β under the influence of SDS ^[15-20]. At high concentrations of SDS, close to the critical micelle concentration (CMC) and above, A β is found to have an α -helical conformation ^[15-18,20]. At submicellar concentrations, SDS seems to accelerate the formation of spherical aggregates ^[21,22], however, detailed information is missing because samples are heterogeneous, which makes them difficult to study further ^[9,10,13,23,24]. We use EPR to address this problem ^[25-28]. Here we employ spin-label EPR to obtain local information about the different sections of the A β 40 peptide during the process of aggregation. To this aim, two cysteine variants of A β 40, bearing a nitroxide spin label at the N-terminus or in the middle of the sequence, are examined to study the effect of SDS at various concentrations. The present study suggests that at submicellar concentrations of SDS the A β 40/SDS aggregates have different shapes. We show that by spin-label mobility EPR local information about A β aggregation at a wide range of SDS concentrations can be obtained.

3.2 Materials and methods

The A β 40 peptide as well as two cysteine-A β variants: [cys26]-SL-A β (in short: SL26-A β) and [cys1]-SL-A β (in short: SL1-A β), differing in the position of the spin label, were purchased from AnaSpec (purity > 95 %), the solvent DMSO was purchased from Biosolve (purity 99.8 %), the MTS spin label ((1-oxyl-2,2,5,5-tetramethylpyrroline-3-methyl) methanethiosulfonate) was purchased from Toronto Research Chemicals Inc. (Brisbane Rd., North York, Ontario, Canada, M3J 2J8). Spin labeling was performed and the purified spin-labeled A β was analyzed by liquid chromatography as described previously ^[25]. The peptide was lyophilized and stored in the freezer (-20⁰ C) until used.

3.2.1 Sample preparation protocol

Two cysteine variants of the A β peptide, SL1-A β and SL26-A β , differing in the position of the spin label were used. From each A β peptide variant six different A β sample conditions, differing in SDS concentrations (1.5 mM, 3 mM, 4 mM, 7 mM,

36 mM, and 72 mM) were prepared and compared to a sample into which no SDS was added. The total peptide concentration was kept constant at 0.55 mM. The peptide was a mixture of wild type A β and SL-A β , which contained 14 % SL-A β resulting in diamagnetically diluted samples as reported before ^[25]. Samples were prepared as described in chapter two of this thesis. In the remainder of the text we use the detergent to peptide (D/P) ratio to refer to each sample condition, i.e., D/P = 0, 2.7, 5.4, 7.3, 12.7, 65.4, and 130.9, which refers to [SDS] = 0 mM, 3 mM, 4 mM, 7 mM, 36 mM, and 72 mM, respectively.

3.2.2 EPR experiments

The X-band cw EPR measurements have been performed at room temperature (20°C) using an ELEXSYS E680 spectrometer (Bruker, Rheinstetten, Germany) equipped with a rectangular cavity. Samples of 10-15 μ l peptide solution were drawn into Blaubrand 50 μ l capillaries. Measurements were performed using the following parameters: 6.31 mW of microwave power, a modulation amplitude of 1.4 G, and a modulation frequency of 100 kHz. The accumulation time for the spectra was 40 minutes per spectrum. All samples were prepared and measured at least twice.

3.2.3 Simulations of EPR spectra

Matlab (version 7.11.0.584, Natick, Massachusetts, U.S.A) and the EasySpin package ^[29] were used for the simulation of EPR spectra. For all simulations the following tensor values were used: $g = [2.00906, 2.00687, 2.00300]$ ^[25,30] and $A_{xx} = A_{yy} = 12$ and 13 MHz in DMSO and buffer, respectively. For the fast and medium components, different A_{zz} values were used than for the slow component, as discussed before ^[25]. For each fraction over-modulation effects were taken into account in EasySpin. Usually a superposition of one to three components was required to simulate the spectra. In all cases, isotropic rotation of the spin label was sufficient to reproduce the line-shape observed.

3.3 Results

The spectra of both SL-A β variants in DMSO, in which the A β peptide is in the monomeric form ^[31-33], have three narrow lines (figure 3.1). At low field, the first two lines of both SL-A β variants in DMSO have similar intensities, whereas the intensity of the third line at high field is larger for the sample of SL1-A β compared to that of SL26-A β .

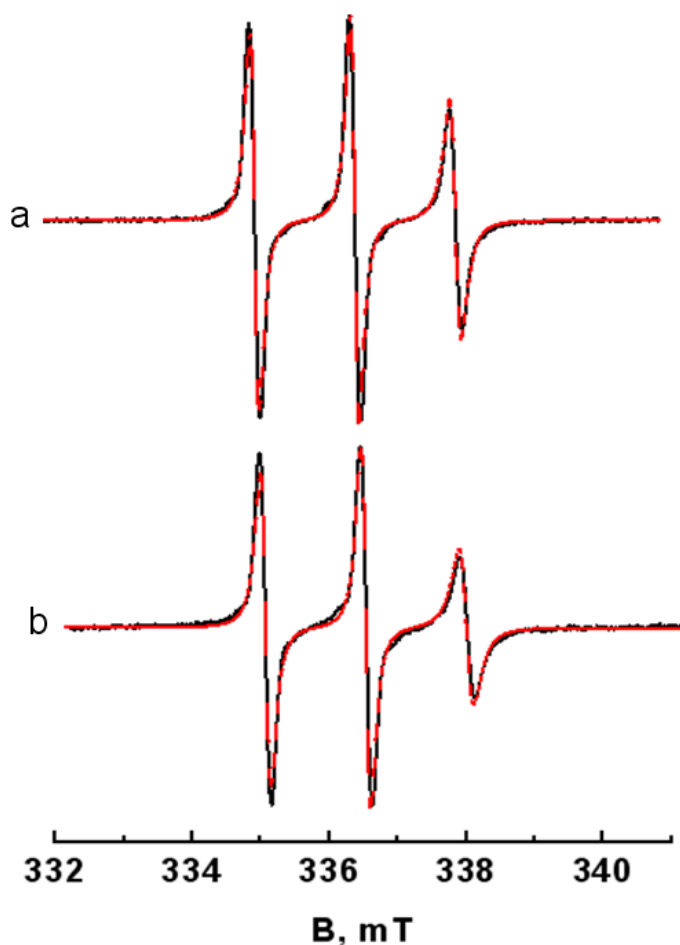


Figure 3.1 Room temperature EPR spectra of monomeric spin-labeled A β in DMSO. a: SL1-A β . Black line: experiment, red line: simulation. The rotation-correlation time τ_r is 0.19 ns. b: SL26-A β . Black line: experiment, red line: simulation. The rotation-correlation time τ_r is 0.27 ns.

Under aggregation conditions ^[25] (in buffer) and in the absence of SDS ($D/P = 0$), the lines of both SL-A β variants are broadened and additional lines are observed as reported before ^[25] (figure 3.2.a and 3.2.a'). In the presence of SDS, particularly at low concentrations of SDS ($D/P = 2.7, 5.4$), the spectra of SL1-A β differ from those of SL26-A β (figure 3.2.a-c and 3.2.a'-c'), whereas at higher concentrations (above 7 mM, $D/P = 12.7$), both SL-A β variants have identical spectra (figure 3.2.f and 3.2.f'). At D/P ratios of 7.3 and 12.7 the spectrum of SL1-A β has narrower lines compared to those of SL26-A β .

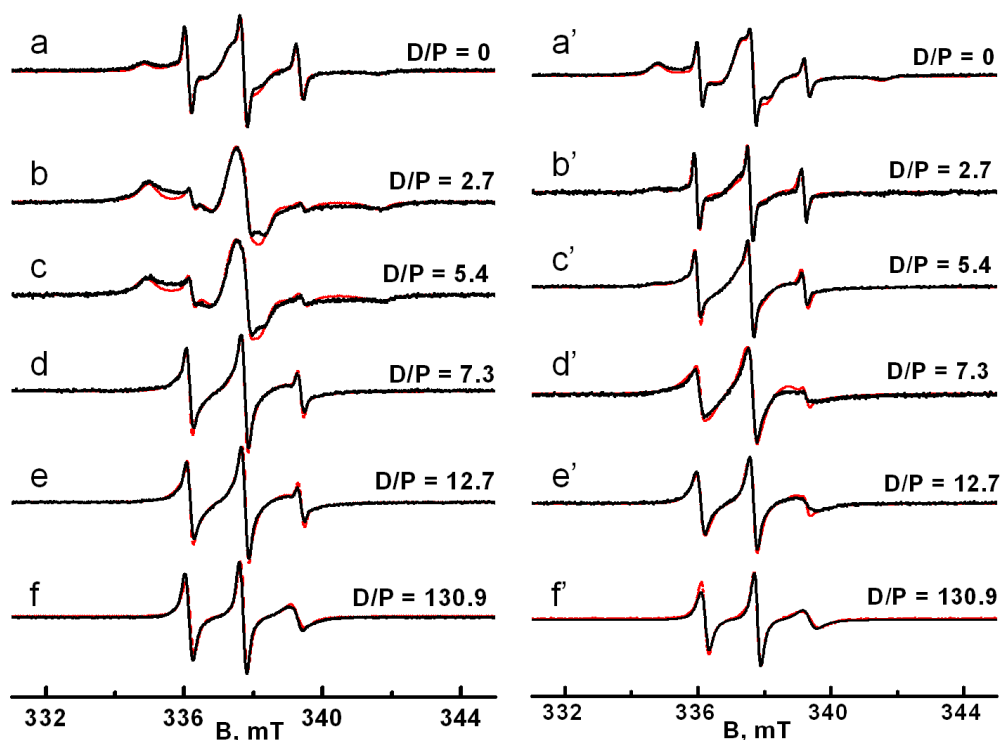


Figure 3.2 Room temperature EPR spectra of SL1-A β and SL26-A β in buffer for samples with different SDS detergent to peptide (D/P) ratios. a to f : Spectra for SL1-A β samples. From a to f the D/P ratio increases. a' to f' : Spectra for SL26-A β samples organized as in the left part of the figure. Black line: experiment, red line: simulation.

By means of simulation, we quantify the spectral changes. The spectra of both SL-A β variants in DMSO are simulated by a single component with a τ_r value of 0.19 ns for SL1-A β and 0.27 ns for SL26-A β . We attribute the difference in the τ_r values to a slightly lower local mobility of the spin label at position 26 compared to that at position 1. The spectra of both SL-A β variants in buffer in the absence of SDS detergent are simulated using three components^[25], which, in the remainder of the text, we refer to as fast, medium and slow. Each component is characterized by its τ_r value, and the amount by which this component contributes to the spectrum (table 3.1 and 3.2). We first describe the trends of the amount, and next the corresponding τ_r values.

Table 3.1 EPR parameters obtained from the simulation of cw EPR spectra of the SL1-A β samples. Given are: τ_r , rotation-correlation time, A_{zz} , the hyperfine splitting along the z-direction, lw , the component line-width of the simulation, and % stands for the contribution of the component to the total spectrum.

D/P	fast				medium				slow			
	τ_r (ns)	A_{zz} (MHz)	lw (mT)	%	τ_r (ns)	A_{zz} (MHz)	lw (mT)	%	τ_r (ns)	A_{zz} (MHz)	lw (mT)	%
0	0.19 ± 0.02	110	0.14	10 ± 2.00	2.55 ± 0.35	110	0.32	51 ± 2.00	> 50	95	0.50	39 ± 2.00
2.7	0.43 ± 0.02	110	0.14	2.5 ± 0.50	4.80 ± 0.40	110	0.32	64 ± 4.00	> 50	95	0.50	33.5 ± 2.50
5.4	0.43 ± 0.02	110	0.14	2.5 ± 0.50	4.65 ± 0.55	110	0.32	75 ± 3.00	> 50	95	0.50	22.5 ± 2.50
7.3	0.19 ± 0.02	110	0.14	10 ± 2.00	1.76 ± 0.16	110	0.14	90 ± 2.00	-	-	-	-
12.7	0.19 ± 0.02	110	0.14	7 ± 2.00	1.55 ± 0.08	110	0.14	92 ± 3.00	-	-	-	-
65.4	-	-	-	-	0.93 ± 0.03	110	0.06	100	-	-	-	-
130.9	-	-	-	-	0.93 ± 0.03	110	0.06	100	-	-	-	-

Table 3.2 EPR parameters obtained from the simulation of cw EPR spectra of the SL26-A β samples. Given are: τ_r , rotation-correlation time, A_{zz} , the hyperfine splitting along the z-direction, lw , the component line-width of the simulation, and % stands for the contribution of the component to the total spectrum.

D/P	fast				medium				slow			
	τ_r (ns)	A_{zz} (MHz)	lw (mT)	%	τ_r (ns)	A_{zz} (MHz)	lw (mT)	%	τ_r (ns)	A_{zz} (MHz)	lw (mT)	%
0	0.27 ± 0.02	110	0.14	6 ± 1.00	3.6 ± 0.10	110	0.32	52 ± 4.00	> 50	95	0.50	42 ± 4.00
2.7	0.26 ± 0.02	110	0.14	24 ± 1.00	2.1 ± 0.10	110	0.32	36 ± 4.00	> 50	95	0.50	40 ± 4.00
5.4	0.26 ± 0.02	110	0.14	13 ± 1.00	2.1 ± 0.10	110	0.32	74 ± 4.00	> 50	95	0.50	13 ± 4.00
7.3	0.26 ± 0.02	110	0.14	4 ± 1.00	2.1 ± 0.10	110	0.14	96 ± 1.00	-	-	-	-
12.7	0.27 ± 0.02	110	0.14	7 ± 1.00	1.4 ± 0.10	110	0.14	93 ± 1.00	-	-	-	-
65.4	-	-	-	-	0.93 ± 0.03	110	0.06	100	-	-	-	-
130.9	-	-	-	-	0.93 ± 0.03	110	0.06	100	-	-	-	-

3.3.1 Effect of SDS on the amount of different components

In the absence of SDS ($D/P = 0$), the spectra of both SL-A β variants are composed of almost equal amounts of the slow and the medium component and a small fraction (about 10 %) of the fast component. The amount of each mobility component at different D/P ratios is represented in figure 3.3. At low concentrations of SDS (between $D/P = 0$ and 5.4), the trend of the amount of fast and the medium component of SL26-A β is different from that of SL1-A β . For SL1-A β the amount of fast component decreases and the amount of medium component increases. This trend is not evident for SL26-A β (figure 3.3). In the same concentration region (between $D/P = 0$ and 5.4), the amount of slow component decreases in both SL-A β variants. Above a D/P ratio of 5.4 the slow component has disappeared leaving only the fast and medium components. At higher concentrations of SDS (above 7 mM SDS, i.e., $D/P = 12.7$), which is close to the critical micelle concentration of SDS only one component of medium mobility is left, which has the same parameters for both SL-A β variants.

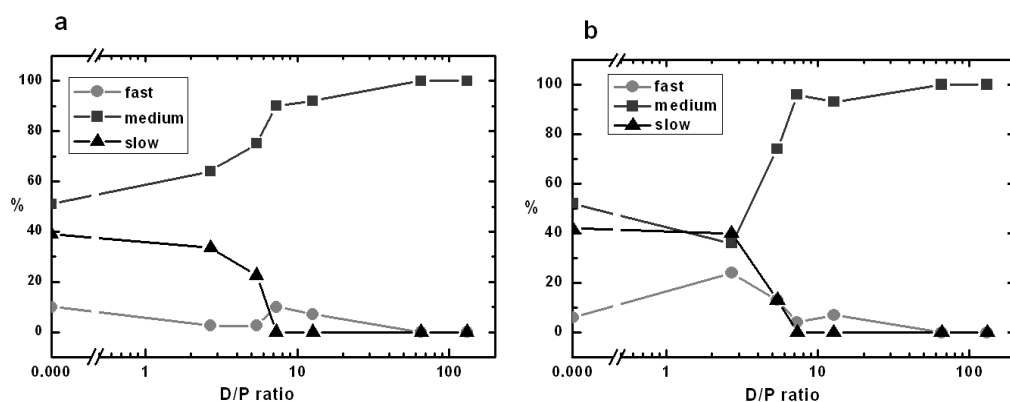


Figure 3.3 Amount of the spectral components as a function of the D/P ratios. a: SL1-A β . b: SL26-A β .

3.3.2 Effect of SDS on the rotation-correlation time

The τ_r values of the fast component of the EPR spectra of SL1-A β and SL26-A β in buffer are identical to those of the respective SL-A β variants in DMSO. We therefore assign the fast fraction to monomeric A β .

In the presence of SDS up to $D/P = 5.4$ the τ_r values of the fast and the medium component of SL1-A β are larger than those of SL26-A β . For SL1-A β , at $D/P < 7.3$, the τ_r values of both fast and medium components slightly increase with increasing SDS concentration, whereas those for SL26-A β remain constant over that range

($D/P < 7.3$). At higher values of D/P (above $D/P = 12.7$; i.e., 7 mM SDS) no fast component is detected in the spectra of both SL-A β variants. The τ_r values of the only observed component in both SL-A β variants are identical. This τ_r is longer than the τ_r of both SL-A β variants in DMSO, in which the A β peptide is in the monomeric form.

3.4 Discussion

We have investigated the aggregation of A β at different concentrations of SDS by monitoring two different positions in the A β chain; the N-terminal SL1-A β and the central SL26-A β . From the two label positions we can differentiate spectral changes due to local mobility, analyzing the parameters that differ for SL1-A β and SL26-A β . Spectral changes because of a change of the aggregation state of A β should be reflected in identical parameters for SL1-A β and SL26-A β .

Figure 3.4 shows the changes in aggregation state: the amount of slow component and the amount of combined fast and medium component. Both amounts agree within the experimental uncertainty for SL1-A β and SL26-A β . It stands to reason that the A β aggregation state changes in a continuous way with the SDS concentration: the amount of slow component decreases, whereas the amount of the more mobile components increases. Considering the mobility to reflect qualitatively the size of the aggregate, the A β changes from a more aggregated state with larger particles at low SDS concentrations to a state in which these larger aggregates almost disappear. Concomitantly, the amount of the smaller aggregates increases. Aggregation of A β at submicellar SDS concentrations was also concluded from the absence of monomer-NMR signal^[13] and from β -sheet signatures found in CD and FTIR spectra, which were attributed to aggregated forms of A β ^[10,13,34]. At higher SDS concentrations (above 7 mM, $D/P = 12.7$), i.e., close to the CMC, no larger aggregates remain and the sample appears uniform. The higher SDS concentration results agree with previous observations that the predominant species at high-SDS concentrations is a monomeric A β , solubilized in an SDS micelle^[9,11,13,23,24,35-37].

The difference between the EPR parameters of SL1-A β and SL26-A β in the submicellar SDS concentration regime far exceeds the sample to sample variation. These differences suggest that the regions of A β to which each spin label is attached behave differently in the presence of submicellar SDS concentrations. At the lowest SDS concentrations investigated ($D/P = 2.7$ and 5.4) the N-terminus goes through a phase of immobilization, as evidenced by the larger τ_r values of the fast and medium component at these SDS concentrations and the smaller amount of the fast component. The spectral parameters of SL26-A β reveal an almost inverse behavior, showing that the central part of the peptide becomes slightly more mobile at these

low SDS concentrations. The SL26-A β variant reveals an immobilization event of the central region of A β at higher SDS concentrations around D/P ratios of 7.3.

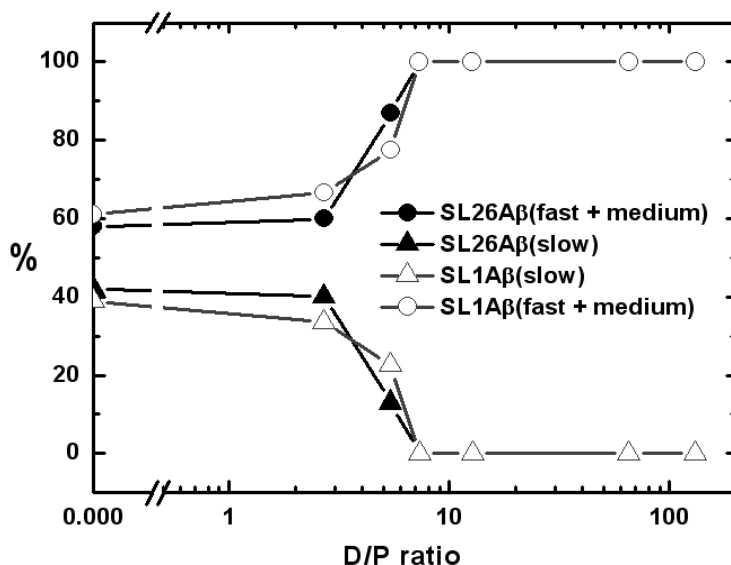


Figure 3.4 Amount of the spectral components as a function of the D/P ratios. The amount of the slow component of the SL1-A β and SL26-A β variants are shown with triangles, similar to figure 3.3 (filled triangles: SL26-A β , non-filled triangles: SL1-A β). The amount of the fast and the medium components of the SL1-A β and SL26-A β variants are shown together with circles (filled circles: SL26-A β , non-filled circles: SL1-A β). The values for the circles are obtained by adding the amount of the fast to the amount of the medium component at each D/P ratio. In both SL-A β variants, the amount of slow component decreases, whereas the amount of the more mobile components (fast plus medium) increases.

At low SDS to peptide ratios, aggregates should be dominated by A β -A β interactions and these apparently restrict the mobility of the N-terminus. Since this region is not considered to be part of the fibrilization domain of A β [38], the aggregates presumably differ from fibrils. Support for compaction involving the N-terminus also comes from Sambasivam et al. [13,39], where FRET distances between residues 1 and 10 suggest an α -helix or a β -turn of the N-terminus of A β at a 1.5 mM concentration of SDS, rather than an extended β -sheet. Wahlström et al. [13] interpret their CD data as two β -sheet-type structures, with a transition point around a D/P ratio of 11. This could suggest that at submicellar SDS concentrations (D/P = 2.7 and 5.4) A β is an oligomer [13,23] in which the N-terminus is trapped and the middle part is more flexible. Taking the β -sheet character into account [13], that would agree with a non-fibrillar type of β -sheet oligomer. We speculate that at these

low concentrations of SDS the A β peptide acts as a kind of detergent (figure 3.5). The hydrophilic N-terminus^[38] locates at the water/aggregate interface, which helps to solubilize the aggregate as long as there are not sufficient SDS molecules to perform this task. This position in the interface immobilizes the N-terminus. The SDS could help breaking up the hydrophilic interaction between the aggregation domains of A β (residues 25-35)^[40], which makes this central part of A β more mobile. Above D/P ratios of 5.4, there are sufficient SDS molecules to replace (some of) the A β N-termini at the water/aggregate interface. The N-terminus, which is hydrophilic^[38], becomes more exposed, as witnessed by the increase in the amount of the fast spectral component and the decrease in τ_r of the medium component. The central part of A β becomes buried. Most likely the headgroups of SDS face the aqueous phase and the tails interact with the central hydrophobic part of A β . At SDS concentrations above the CMC this form would then transform to the micellar, α -helical form of A β . The α -helical form was proposed to be a monomeric A β , solubilized in an SDS micelle^[9,11,13,23,24,35-37]. This proposal is consistent with the data presented in chapter 2 of this thesis, revealing a single, homogeneous form of A β in which A β -A β interactions are not detectable. Based on the model proposed by Jarvet et al.^[23] the N-terminus and the central part of the peptide are not part of the helical domain. Our results show that the N-terminus and central part of A β have similar mobilities, which suggests a similar location of these positions with respect to the micelle.

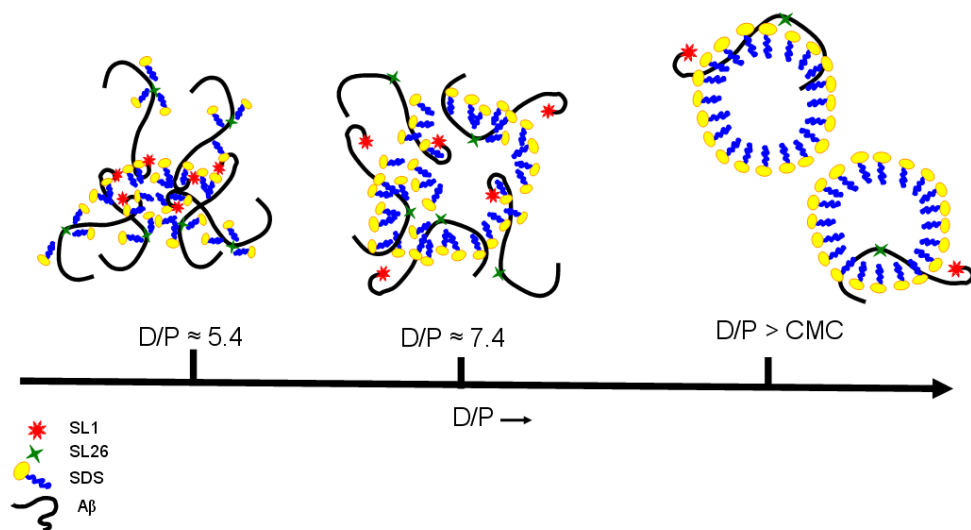


Figure 3.5 Cartoon of the A β aggregation at different D/P ratios. On the left side, the A β aggregate is shown at a D/P ratios of about 5.4, in which the hydrophilic N-terminus becomes immobilized at the aggregate/buffer interface. This helps to solubilize the aggregate. In the middle, the A β aggregate is shown at D/P ratios of about 7.3, where there are sufficient SDS molecules to replace (some of) the A β N-termini at the water/aggregate interface. On the right, the A β peptide is shown at D/P ratios above the CMC of SDS. Two possible models for A β interaction with a micelle are shown, in which both spin labels would have similar rotation correlation times.

In conclusion, we have shown that previously inaccessible detail of the low-SDS form of A β can be obtained by spin label EPR. A careful study of two labeling positions in A β and the sensitivity of this EPR approach to local mobility reveal a change in the aggregate state. From a particle, in which the N-terminus of A β participates in the solubilization by being located at the particle/water interface, the aggregate changes to an SDS-solubilized state that is a precursor to the one A β /micelle state above the CMC of SDS. We also demonstrate how from the local mobility parameters global properties of the A β -aggregation state are obtained, revealing the unique potential of EPR in studying the A β aggregation.

Reference List

- [1] F.Chiti, C.M.Dobson, *Annu.Rev.Biochem.* **2006**, 75 333-366.
- [2] J.Hardy, D.J.Selkoe, *Science* **2002**, 297 353-356.
- [3] D.G.Lynn, S.C.Meredith, *J.Struct.Biol.* **2000**, 130 153-173.
- [4] M.Margittai, R.Langen, *Q.Rev.Biophys.* **2008**, 41 265-297.
- [5] F.Panza, V.Solfrizzi, V.Frisardi, C.Capurso, A.D'Introno, A.M.Colacicco, G.Vendemiale, A.Capurso, B.P.Imbimbo, *Drugs Aging* **2009**, 26 537-555.
- [6] D.J.Selkoe, *Neuron* **1991**, 6 487-498.
- [7] D.J.Selkoe, *Physiol Rev.* **2001**, 81 741-766.
- [8] N.Yamamoto, K.Hasegawa, K.Matsuzaki, H.Naiki, K.Yanagisawa, *J.Neurochem.* **2004**, 90 62-69.
- [9] V.Rangachari, D.K.Reed, B.D.Moore, T.L.Rosenberry, *Biochemistry* **2006**, 45 8639-8648.
- [10] V.Rangachari, B.D.Moore, D.K.Reed, L.K.Sonoda, A.W.Bridges, E.Conboy, D.Hartigan, T.L.Rosenberry, *Biochemistry* **2007**, 46 12451-12462.
- [11] J.M.Lin, T.L.Lin, U.S.Jeng, Z.H.Huang, Y.S.Huang, *Soft Matter* **2009**, 5 3913-3919.
- [12] B.O'Nuallain, D.B.Freir, A.J.Nicoll, E.Risse, N.Ferguson, C.E.Herron, J.Collinge, D.M.Walsh, *J.Neurosci.* **2010**, 30 14411-14419.
- [13] A.Wahlström, L.Hugonin, A.Perálvarez-Marín, J.Jarvet, A.Gräslund, *FEBS J.* **2008**, 275 5117-5128.
- [14] S.S.S.Wang, K.N.Liu, T.C.Han, *Biochimica et Biophysica Acta-Molecular Basis of Disease* **2010**, 1802 519-530.
- [15] G.Duplatre, M.F.F.Marques, M.daGracaMiguel, *Journal of Physical Chemistry* **1996**, 100 16608-16612.
- [16] E.Fuguet, C.Rafols, M.Roses, E.Bosch, *Analytica Chimica Acta* **2005**, 548 95-100.
- [17] A.Helenius, K.Simons, *Biochim.Biophys.Acta* **1975**, 415 29-79.
- [18] G.D.Henry, B.D.Sykes, *Nuclear Magnetic Resonance, Pt C* **1994**, 239 515-535.
- [19] P.Mukerjee, K.J.Mysels, P.Kapauan, *Journal of Physical Chemistry* **1967**, 71 4166-&.
- [20] M.Sammalkorpi, M.Karttunen, M.Haataja, *J.Phys.Chem.B* **2007**, 111 11722-11733.
- [21] N.Sureshbabu, R.Kirubakaran, R.Jayakumar, *Eur.Biophys.J.* **2009**, 38 355-367.
- [22] N.Sureshbabu, R.Kirubakaran, H.Thangarajah, E.J.Malar, R.Jayakumar, *J.Mol.Neurosci.* **2010**, 41 368-382.
- [23] J.Jarvet, J.Danielsson, P.Damberg, M.Oleszczuk, A.Gräslund, *J.Biomol.NMR* **2007**, 39 63-72.
- [24] H.Y.Shao, S.C.Jao, K.Ma, M.G.Zagorski, *Journal of Molecular Biology* **1999**, 285 755-773.
- [25] I.Sepkhanova, M.Drescher, N.J.Meeuwenoord, R.W.A.L.Limpens, R.I.Koning, D.V.Filippov, M.Huber, *Applied Magnetic Resonance* **2009**, 36 209-222.
- [26] M.Grimaldi, M.Scrima, C.Esposito, G.Vitiello, A.Ramunno, V.Limongelli, G.D'Errico, E.Novellino, A.M.D'Ursi, *Biochim.Biophys.Acta* **2010**, 1798 660-671.
- [27] F.Mito, T.Yamasaki, Y.Ito, M.Yamato, H.Mino, H.Sadasue, C.Shirahama, K.Sakai, H.Utsumi, K.Yamada, *Chemical Communications* **2011**, 47 5070-5072.
- [28] G.Vitiello, M.Grimaldi, A.Ramunno, O.Ortona, G.De Martino, A.M.D'Ursi, G.D'Errico, *Journal of Peptide Science* **2010**, 16 115-122.
- [29] S.Stoll, A.Schweiger, *Journal of Magnetic Resonance* **2006**, 178 42-55.
- [30] S.Steigmiller, M.Börsch, P.Gräber, M.Huber, *Biochim.Biophys.Acta* **2005**, 1708 143-153.
- [31] K.Broersen, F.Rousseau, J.Schymkowitz, *Alzheimers Res.Ther.* **2010**, 2 12.
- [32] K.Broersen, W.Jonckheere, J.Rozenski, A.Vandersteen, K.Pauwels, A.Pastore, F.Rousseau, J.Schymkowitz, *Protein Eng Des Sel* **2011**, 24 743-750.
- [33] M.L.Giuffrida, F.Caraci, B.Pignataro, S.Cataldo, B.P.De, V.Bruno, G.Molinaro, G.Pappalardo, A.Messina, A.Palmigiano, D.Garozzo, F.Nicoletti, E.Rizzarelli, A.Copani, *J.Neurosci.* **2009**, 29 10582-10587.
- [34] D.J.Tew, S.P.Bottomley, D.P.Smith, G.D.Ciccotosto, J.Babon, M.G.Hinds, C.L.Masters, R.Cappai, K.J.Barnham, *Biophysical Journal* **2008**, 94 2752-2766.
- [35] M.Coles, W.Bicknell, A.A.Watson, D.P.Fairlie, D.J.Craik, *Biochemistry* **1998**, 37 11064-11077.

- [36] H.Y.Shao, S.C.Jao, M.G.Zagorski, *Abstracts of Papers of the American Chemical Society* **1997**, 213 13-MEDI.
- [37] M.G.Zagorski, L.M.Hou, *Abstracts of Papers of the American Chemical Society* **2002**, 223 C29.
- [38] A.Vitalis, A.Caflisch, *J.Mol.Biol.* **2010**, 403 148-165.
- [39] D.Sambasivam, S.Sivanesan, B.S.Ashok, J.Rajadas, *Neuropeptides* **2011**, 45 369-376.
- [40] R.Liu, C.McAllister, Y.Lyubchenko, M.R.Sierks, *J.Neurosci.Res.* **2004**, 75 162-171.

CHAPTER 4

THE AGGREGATION POTENTIAL OF 1-15 AND 1-16 FRAGMENTS OF THE AMYLOID β PEPTIDE AND THEIR INFLUENCE ON THE AGGREGATION OF A β 40

The aggregation of amyloid β (A β) peptide is important in Alzheimer's disease. Shorter A β fragments may reduce A β 's cytotoxicity and are used in diagnostics. The aggregation of A β 16 is controversial; Liu et al. (*J. Neurosci. Res.* **2004**, 72, 162-171) and Liao et al. (*FEBS Lett.* **2007**, 581, 1161-1165) find that A β 16 does not aggregate and reduces A β 's cytotoxicity, Du et al. (*J. Alzheimers Dis.* **2011**, 27, 401-413) reports that A β 16 aggregates and that A β 16 oligomers are toxic to cells. Here the aggregation potential of two shorter fragments, A β 15 and A β 16, and their influence on A β 40 is measured by Electron Paramagnetic Resonance (EPR) spectroscopy and the Thioflavin T fluorescence assay (ThioT). Continuous wave, 9 GHz EPR measurements and ThioT results reveal that neither A β 15 nor A β 16 aggregate by themselves and that they do not affect A β 40 aggregation.

M. Hashemi Shabestari, T. Plug, M.M. Motazacker, N.J. Meeuwenoord, D.V. Filippov, J.C.M. Meijers, M. Huber.

4.1 Introduction

Fibrillar plaques and aggregates of the 39 to 42 amino-acid residue amyloid β ($A\beta$) peptide in the brain have been recognized as major characteristics of Alzheimer's disease ^[1-4]. The $A\beta$ peptide originates from a proteolytic cleavage of the amyloid precursor protein (APP), a human transmembrane protein crucial for memory ^[3,5]. Recently, more than about 20 shorter $A\beta$ fragments, comprising residues 1-15, 4-15, 5-15, 14-15, 1-13, 1-14, etc. of the N-terminus of the full-length $A\beta$ (table 4.1), have been reported in the cerebrospinal fluid (CSF), in addition to the previously reported $A\beta$ 1-16 fragment ($A\beta$ 16) ^[6-9]. Some of these fragments are up-regulated in Alzheimer's disease ^[6,7]. The soluble $A\beta$ 16 fragment in the brain results from the cleavage between amino acids K₁₆ and L₁₇, the proposed α -secretase cleavage site in the $A\beta$ sequence. Amongst the 20 $A\beta$ fragments that are upregulated, 11 fragments with different length end at amino acid 15, one amino acid before the α -secretase cleavage site, which suggests a novel metabolic pathway for APP ^[6,7]. The short $A\beta$ fragments draw a lot of attention especially in the search for peptide or peptidomimetic inhibitors of $A\beta$ aggregation in the pathological context ^[8,10,11]. For example the $A\beta$ 1-15 fragment ($A\beta$ 15) can be used as a vaccine ^[12,13]. However, the precise sequence of events through which these short fragments form and their role in aggregation and toxicity of the full-length $A\beta$ are still under debate. Reports about the aggregation potential of the N-terminal $A\beta$ fragments by themselves are discrepant. According to Liu et al. ^[14] and Liao et al. ^[15], $A\beta$ 16 does not aggregate and reduces $A\beta$'s cytotoxicity in neuronal cells, whereas Du et al. ^[16] report that $A\beta$ 16 aggregates and that $A\beta$ 16 oligomers are toxic to cells. Du et al. ^[16] also show that $A\beta$ 15 forms aggregates, which are not toxic to cells. These conflicting results, obtained by NMR ^[17-19], FTIR, AFM, and CD ^[14-16] prompted us to investigate the behavior of these N-terminal $A\beta$ fragments by a different technique. We used spin-label EPR and ThioflavinT fluorescence assay to study the fragments $A\beta$ 15 and $A\beta$ 16 (for sequence see table 4.1). Earlier, it was shown that signatures of the oligomeric $A\beta$ peptide can be detected by the spin-label EPR methodology, which suggests this technique as a possible tool to detect the early stages of aggregation of the $A\beta$ peptide ^[20]. Here we employ spin-label EPR to investigate and compare the aggregation potential of $A\beta$ 15 and of $A\beta$ 16, and their influence on the aggregation of $A\beta$ 40. We combined spin-label EPR with diamagnetic dilution, in which the spin-labeled $A\beta$ peptide (SL- $A\beta$) is diluted with unlabeled $A\beta$ peptide (wild type $A\beta$ peptide) to avoid line broadening by spin-spin interaction ^[20-22].

Table 4.1 The amino-acid sequence of the full-length A β peptide (A β 40) and the two fragments, A β 15 and A β 16 studied here. Residues 15 and 16 of A β peptide are glutamine and lysine, respectively. The cysteine variants (Cys-A β) of each of the three peptides with an additional cysteine at the N-terminus are used for spin labeling.

A β peptide	amino-acid sequence
Cys-A β 15	CD ₁ A ₂ E ₃ F ₄ R ₅ H ₆ D ₇ S ₈ G ₉ Y ₁₀ E ₁₁ V ₁₂ H ₁₃ H ₁₄ Q ₁₅
Cys-A β 16	CD ₁ A ₂ E ₃ F ₄ R ₅ H ₆ D ₇ S ₈ G ₉ Y ₁₀ E ₁₁ V ₁₂ H ₁₃ H ₁₄ Q ₁₅ K ₁₆
Cys-A β 40	CD ₁ A ₂ E ₃ F ₄ R ₅ H ₆ D ₇ S ₈ G ₉ Y ₁₀ E ₁₁ V ₁₂ H ₁₃ H ₁₄ Q ₁₅ K ₁₆ L ₁₇ V ₁₈ F ₁₉ F ₂₀ A ₂₁ E ₂₂ D ₂₃ V ₂₄ G ₂₅ S ₂₆ N ₂₇ K ₂₈ G ₂₉ A ₃₀ I ₃₁ I ₃₂ G ₃₃ L ₃₄ M ₃₅ V ₃₆ G ₃₇ G ₃₈ V ₃₉ V ₄₀

By spin-label EPR, the mobility of the peptide is directly monitored enabling the detection of even small amounts (< 10 %) of aggregate, which would be difficult by the methods currently employed ^[23,24]. We demonstrate that under the conditions of our experiments neither A β 15 nor A β 16 aggregate and that they do not seem to affect full-length A β aggregation.

4.2 Materials and methods

The A β 40 peptide and its cysteine-A β variant (H-Cys-Asp-Ala-...-Val-OH) were purchased from AnaSpec (purity > 95 %). The A β 15 and A β 16 and their cysteine-A β variants were purchased from Peptide 2.0 Inc, Chantilly, VA (purity > 95 %), the solvent DMSO was purchased from Biosolve (purity 99.8 %). the MTS spin label ((1-oxyl-2,2,5,5-tetramethylpyrroline-3-methyl) methanethiosulfonate) was purchased from Toronto Research Chemicals Inc. (Brisbane Rd., North York, Ontario, Canada, M3J 2J8). Spin labeling was performed and the purified spin-labeled A β was analyzed by liquid chromatography as described previously ^[20]. The peptides were lyophilized and stored in the freezer (-20° C) until used.

4.2.1 Sample preparation protocol

The A β peptide samples in phosphate-buffered saline (PBS, 12 mM Na₂HPO₄, 137 mM NaCl, 2.7 mM KCl, 1.8 mM KH₂PO₄ at pH 7.4) were prepared as diamagnetically diluted (dd) samples according to the protocol reported before ^[20]. Typical samples contained a mixture of 86 % wild type A β and 14 % SL-A β . Two peptide concentrations (0.55 mM and 1.1 mM) were investigated. For the shorter peptides, the spin-labeled shorter peptides were mixed either with the respective wild type peptide or with the wild type A β 40. A typical sample of SL-A β 15 with wild type A β 40 had the following concentrations: 0.077 mM SL-A β 15, 0.47 mM wild type A β 15 (dd-SL-A β 15) and 0.55 mM wild type A β 40. To investigate the

effect of shorter peptides on the A β 40 peptide, either of the wild type shorter peptides was added to the SL-A β 40 sample.

4.2.2 EPR experiments

Samples of 10-15 μ l peptide solution were drawn into Blaubrand 50 μ l capillaries. The X-band continuous wave EPR measurements were performed using an ELEXSYS E680 spectrometer (Bruker, Rheinstetten, Germany) equipped with a rectangular cavity. A modulation frequency of 100 kHz was used for all measurements; the accumulation time for the spectra was 40 minutes per spectrum. Samples were measured at room temperature (20° C) using 6.331 mW microwave power and a modulation amplitude of 1.4 G. The large modulation amplitude ensured a better signal-to-noise ratio for broad lines. The measurements were made immediately after dissolving in PBS. Samples were kept at room temperature in these capillaries for 10 days without agitation and measured again after two, seven, and 10 days to monitor time dependent effects. In all cases, the spectra were identical to those measured initially (data not shown).

4.2.3 Simulations of EPR spectra

The spectra were simulated using Matlab and the EasySpin package ^[25]. For the simulation the following parameters were used: $g = [2.00906, 2.00687, 2.00300]$ ^[20,26] and $A_{xx} = A_{yy} = 12$ and 13 MHz in DMSO and buffer, respectively. Over-modulation effects were taken into account in EasySpin. According to the simulation, the EPR spectra were composed of three components of different mobilities. These components were referred to as fast, medium, and slow according to their rotation correlation times (τ_r) as reported before ^[20].

4.2.4 Ratio of the intensity of the “fast” and “slow” components in each spectrum

Another way to define the mobility of the spin label, rather than by the relatively time-consuming simulations, is to measure amplitude ratios directly from the spectra ^[20,27,28]. Here we use the amplitude ratio of the mobile component to the strongly immobilized component. The contribution of these two components was obtained by selecting specific positions in the EPR spectra ($B_{0slow} = 334.3 \pm 0.1$ mT; $B_{0fast} = 337.3 \pm 0.1$ mT) at which one component has a large amplitude and the other a small one. The ratio of the fast to slow component, i.e., the ratio of the amplitudes of the two selected spectral positions (see results) gives an indication of the aggregation state of the peptide. The larger the ratio, the smaller is the degree of aggregation in the sample. The values and the sample to sample variation of this ratio (standard deviation) were determined for three independent sets of samples.

4.2.5 Thioflavin T fluorescence assay

As there is a stoichiometric and saturable interaction between ThioT and amyloid fibrils, fluorescence from the amyloid-ThioT complex provides accurate quantification of amyloid fibril formation as a function of amyloid fibril number [29,30]. For the ThioT fluorescence assay, six different A β peptide samples, differing in A β peptide content were investigated. For the full-length peptide two peptide concentrations (0.55 mM and 1.1 mM) and for the shorter peptides one concentration (0.55 mM) was investigated. To examine the effect of shorter peptides on the A β 40 peptide, 1:1 mixtures of the shorter peptides with the full-length peptide (total peptide concentration of 1.1 mM) were prepared. For ThioT readings, the peptide was diluted with 10 μ M ThioT in 50 mM glycine/NaOH buffer, pH 8.6. The final concentration of peptide in the ThioT wells was 11 μ M or 27.5 μ M. Fluorescence was measured with the Fluostar Galaxy fluorometer, 96 well, Black, uClear–Plate Ref. 655090 Greiner (fluor plate). The settings were: excitation λ : 450 nm emission λ : 485 nm, 1 cycle, 10 flashes, and gain: 75. All samples were prepared and measured at least three times.

4.3 Results

Figure 4.1 shows the continuous-wave EPR spectra of SL-A β 15 in DMSO and in PBS measured at room temperature. The spectrum of the SL-A β 15 peptide under aggregation conditions (in PBS) is similar to the spectrum of the peptide in DMSO, a solvent in which amyloid peptides are in the monomeric form [31-33]. The same is true for the EPR spectra of SL-A β 16 in PBS and in DMSO (spectra not shown), which indicates that A β 15 and A β 16 are monomeric in PBS. The spectrum of the SL-A β 40 peptide under aggregation conditions has multiple components and broadened lines (figure 4.2) [20]. In figure 4.2, the spectra of the spin-labeled shorter peptides, SL-A β 15 and SL-A β 16, in PBS, are compared to that of the SL-A β 40 peptide at the same peptide concentration. The differences of aggregation in SL-A β 40 (broad lines, extra signals) are absent in the spectra of shorter peptides further emphasizing the absence of aggregation in SL-A β 15 and SL-A β 16.

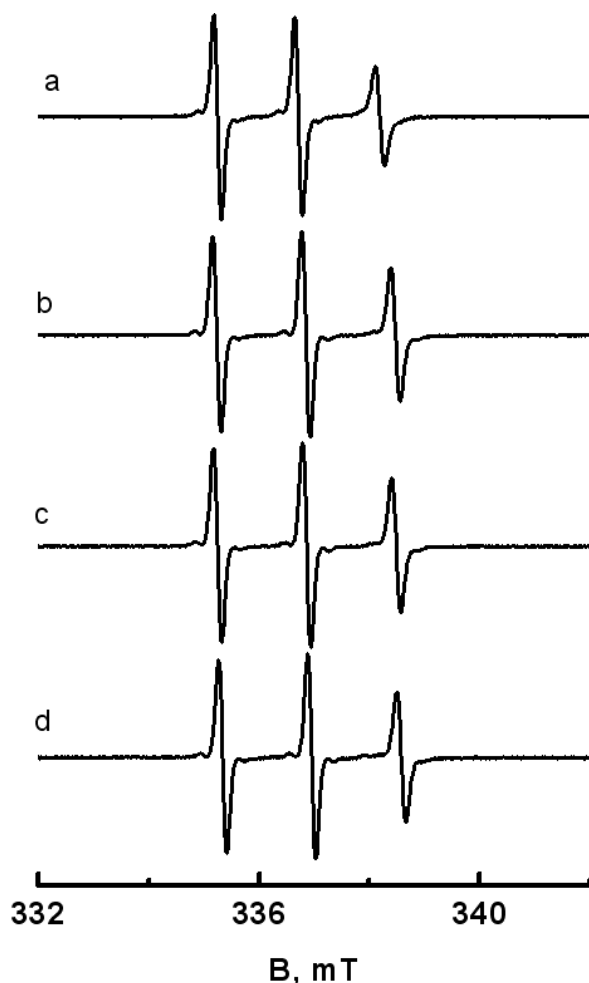


Figure 4.1 Room temperature EPR spectra of SL-A β 15 under different conditions. a: SL-A β 15 in DMSO. b: Mixture of the diamagnetically diluted SL-A β 15 (diamagnetically diluted SL-A β 15 (dd-SL-A β 15): a mixture of 86 % wild type A β 15 and 14 % SL-A β 15) with wild type A β 15 in PBS (dd-SL-A β 15: wild type A β 15, 1:1). Total peptide concentration is 1.1 mM. c: Mixture of dd-SL-A β 15 with wild type A β 40 in PBS (dd-SL-A β 15: wild type A β 40, 1:1). Total peptide concentration is 1.1 mM. d: Mixture of dd-SL-A β 15 with wild type A β 40 in PBS (dd-SL-A β 15: wild type A β 40, 1:2). Total peptide concentration is 1.65 mM.

The EPR spectra of the shorter peptides in the presence of A β 40 are similar to the spectra of the shorter peptides alone. Furthermore, the spectral line-shape of the shorter peptides did not change for the two concentrations of the A β 40 peptide used (0.55 mM and 1.1 mM), showing the absence of interaction of A β 15 and A β 16 with A β 40 (figure 4.1). These observations are confirmed by the similarity of the simulation parameters given in table 4.2.

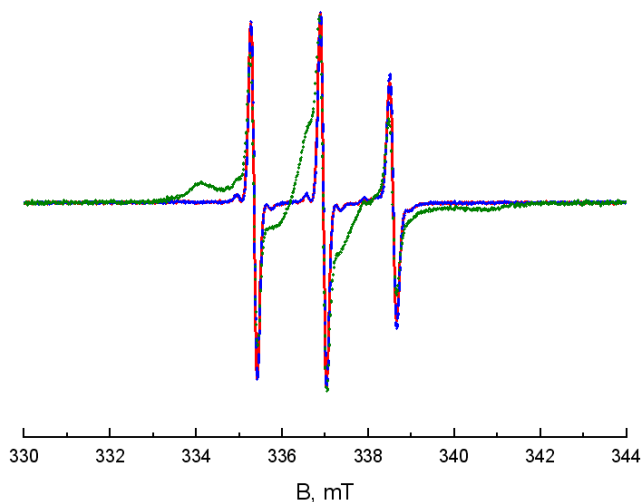


Figure 4.2 Room temperature EPR spectra of SL-A β 15, SL-A β 16, and SL-A β 40 under conditions, where A β 40 aggregates. Red line: diamagnetically diluted SL-A β 15, i.e., SL-A β 15: wild type A β 15 (14 % SL-A β 15: 86 % wild type A β 15). Blue line: diamagnetically diluted SL-A β 16, i.e., SL-A β 16: wild type A β 16 (14 % SL-A β 16: 86 % wild type A β 16). Green line: diamagnetically diluted SL-A β 40, i.e., SL-A β 40: wild type A β 40 (14 % SL-A β 40: 86 % wild type A β 40). Total peptide concentration is 0.55 mM for all samples.

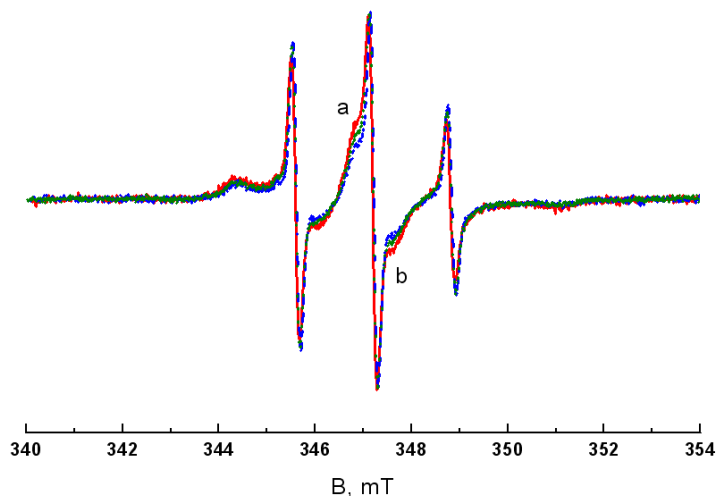


Figure 4.3 Room temperature EPR spectra showing the effect of A β 15 and A β 16 on A β 40. Red line: dd-SL-A β 15 (14 % SL-A β 15: 86 % wild type A β 15): wild type A β 40 (1:1). Blue line: dd-SL-A β 16 (14 % SL-A β 16: 86 % wild type A β 16): wild type A β 40 (1:1). Green line: dd-SL-A β 40 (14 % SL-A β 40: 86 % wild type A β 40): wild type A β 40 (1:1). Total peptide concentration is 1.1 mM for all samples. There is a small difference among the three spectra in regions a and b.

Table 4.2 EPR parameters obtained from simulation for the SL-A β 15 peptide and the SL-A β 16 peptide in PBS and in DMSO. Given are: τ_r , rotation-correlation time, A_{zz} is the hyperfine splitting along the z-direction, lw is the component line-width of the simulation.

sample	solvent	[total peptide] (mM)	τ_r (ns)	A_{zz} (MHz)	lw (mT)
SL-A β 15	DMSO	0.55	0.17 ± 0.02	100	0.09
SL-A β 15 + A β 15	PBS	0.55	0.10 ± 0.02	110	0.11
SL-A β 15 + A β 40	PBS	0.55	0.11 ± 0.02	110	0.10
SL-A β 15 + A β 40	PBS	1.10	0.15 ± 0.02	110	0.10
SL-A β 16	DMSO	0.55	0.18 ± 0.02	100	0.09
SL-A β 16 + A β 16	PBS	0.55	0.10 ± 0.02	110	0.11
SL-A β 16 + A β 40	PBS	0.55	0.11 ± 0.02	110	0.10
SL-A β 16 + A β 40	PBS	1.10	0.15 ± 0.02	110	0.10

The spectra of the SL-A β 40 peptide alone and of the SL-A β 40 peptide in the presence of the unlabeled shorter peptides are shown in figure 4.3. By means of simulation ^[20], we determined the τ_r values of each mobility component (see materials and methods) and their contribution to the total spectra (table 4.3). The τ_r values of the SL-A β 40 peptide in the presence or absence of shorter peptides as well as the amount of each mobility component are given in table 4.3. There is a small difference among the three spectra in regions “a” and “b”, also reflected in small differences of the τ_r values and their relative contributions (figure 4.3).

Table 4.3 EPR parameters obtained from simulation for the A β 40 peptide alone as well as in the presence of shorter peptides: A β 15 and A β 16. Given are: τ_r , rotation-correlation time, A_{zz} is the hyperfine splitting along the z-direction, lw is the component line-width of the simulation and % stands for the contribution of the component to the total spectrum.

sample	fast				medium				slow			
	τ_r (ns)	A_{zz} (MHz)	lw (mT)	%	τ_r (ns)	A_{zz} (MHz)	lw (mT)	%	τ_r (ns)	A_{zz} (MHz)	lw (mT)	%
SL-A β 40	0.19 ± 0.04	110	0.14	12 ± 2	2.50 ± 0.35	110	0.32	52 ± 2	> 50	94	0.50	36 ± 2
SL-A β 40 + A β 15	0.19 ± 0.04	110	0.14	11 ± 2	2.50 ± 0.35	110	0.32	53 ± 2	> 50	94	0.50	36 ± 2
SL-A β 40 + A β 16	0.19 ± 0.04	110	0.14	15 ± 2	2.50 ± 0.35	110	0.32	47 ± 2	> 50	94	0.50	37 ± 2

To determine whether these differences are significant with respect to the sample-to-sample variation we analyzed the ratios of the intensities of the fast to the slow component in each spectrum (figure 4.4) for a large set of samples. Although there is a difference in the intensity ratios of the fast to the slow component of the samples of the SL-A β 40 peptide alone and those containing SL-A β and the shorter

peptides, the differences are not significant, in view of the sample-to-sample variation.

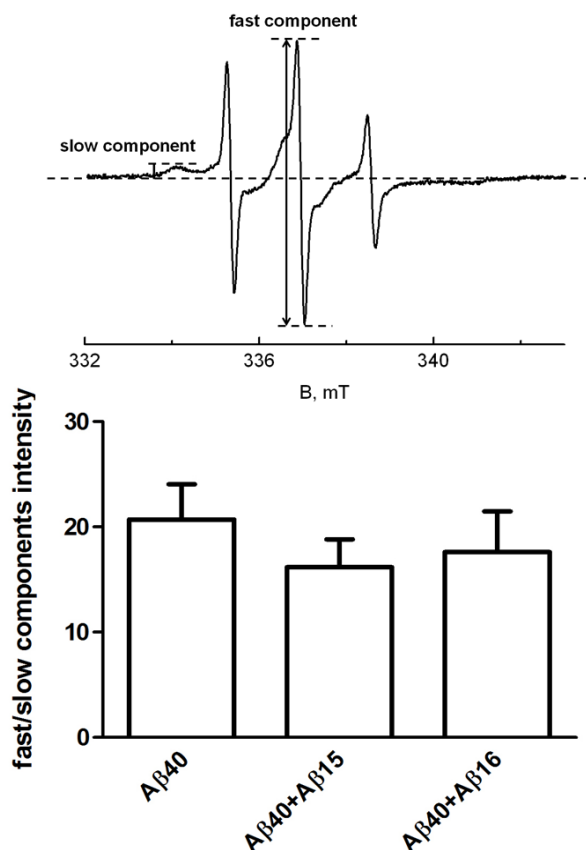


Figure 4.4 Effect of short A β peptides (A β 15 and A β 16) on the aggregation of A β 40. Intensity ratios of the fast/slow components of three A β samples; A β 40, A β 40 + A β 15 and A β 40 + A β 16 are represented as mean \pm SEM of three sets of samples, i.e., each A β sample was fibrillized and measured under the same conditions three times.

An increase in fluorescence of the fibril-specific dye ThioT, compared to the fluorescence of the free ThioT in PBS buffer, is a marker for fibril formation. Relative fluorescence levels for the samples are shown in figure 4.5. The fluorescence level increased in the samples with the full-length peptide, while no fluorescence increase is observed in the samples which contained only the shorter peptides. Samples containing an equivalent amount of shorter peptides and the full-length A β (0.55 mM: 0.55 mM), have a fluorescence level similar to that of pure 0.55 mM full-length A β samples, whereas the fluorescence in a sample with 1.1

mM full-length A β is significantly higher compared to that of 0.55 mM full-length A β .

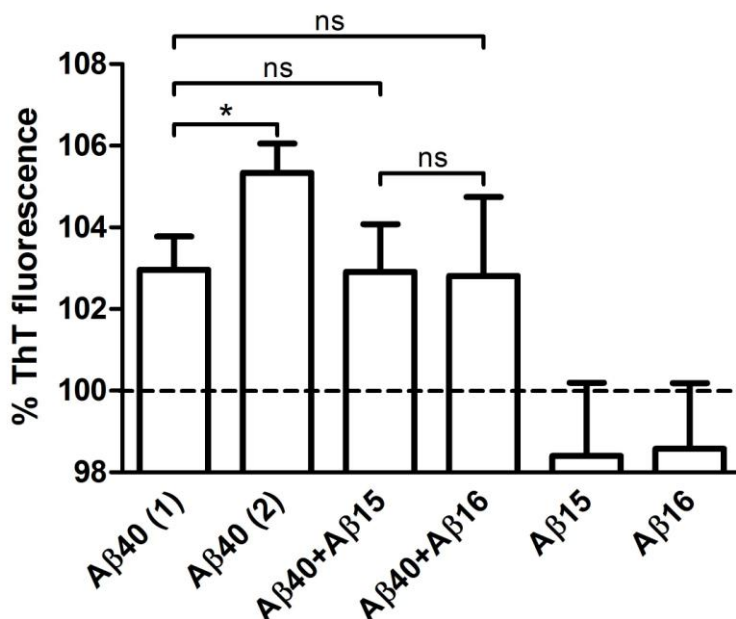


Figure 4.5 ThioT fluorescence (%) of six A β samples; A β 40 (1) (0.55 mM), A β 40 (2) (1.1 mM), A β 40 + A β 15 (0.55 mM), A β 40 + A β 16 (0.55 mM), A β 15 (0.55 mM), A β 16 (0.55 mM). For ThioT readings the peptide was diluted to concentrations of 11 or 27.5 μ M. Values for ThioT fluorescence of ThioT alone were set to 100 % and the ThioT fluorescence of all samples is reported relative to this value (mean \pm SEM of three experiments, i.e., each A β sample was fibrillized and measured under the same conditions three times; * p < 0.05 unpaired t test, ns: not significant).

4.4 Discussion

The aim of this study was to investigate and compare the aggregation potential of the two shorter N-terminal A β peptides A β 15 and A β 16 and to determine if the shorter peptides had an effect on the aggregation of the A β 40 peptide. To monitor the aggregation we used spin-label EPR by which, previously, the aggregation of the A β 40 peptide was studied^[20,34]. In the present study either the short peptides (SL-A β 15 or SL-A β 16) or the A β 40 (SL-A β 40) peptide was spin labeled. By measuring the spin-label mobility of the SL-A β 15 and the SL-A β 16 in the absence/presence of the wild type A β 40 or measuring the spin-label mobility of SL-A β 40 in the presence of either wild type short peptides, the properties of each of the components of the aggregating samples was monitored individually.

For the short A β fragments, A β 15 and A β 16, the ThioT results show the absence of fibril formation. The same is true for the EPR results, where an observed trend towards larger τ_r values at higher concentrations of A β (given in table 4.2 and results) most likely is not a sign of aggregation, but an effect of the increasing viscosity of the solution.

The behavior of A β 15 and A β 16 is not affected by the presence of A β 40, which reveals that the full-length A β does not induce aggregation in A β 15 or A β 16. Furthermore, no evidence for interaction of A β 15 or A β 16 with A β 40 is observed. The A β 40, on the other hand does aggregate under these conditions as is demonstrated in the experiments where SL-A β 40 was monitored in the presence of unlabeled A β 15 and A β 16. In these experiments the difference between the EPR spectra is not significant (figure 4.3), revealing that the shorter peptides also do not inhibit or promote aggregation of full-length A β (table 4.3).

Previous reports about the aggregation of A β 15 and A β 16 had differing outcomes. As in the present study, NMR investigations at high concentrations of A β 16 showed the absence of aggregation ^[17-19]. Similarly, Liu ^[14] and Liao ^[15] conclude from CD, AFM, and ThioT that A β 16 does not aggregate. In contrast, a recent study ^[16] proposes that A β 16 can assemble into a novel type of toxic oligomers and fibrils. These findings cannot be reconciled with the present study unless only a small fraction of the peptide (< 10 %) was in the oligomeric state in the AFM samples.

In summary, we find that the short peptides A β 15 or A β 16 do not directly influence the aggregation of A β 40. This reveals that the effects that these short peptides show in neurotoxicity essays cannot derive from a direct influence of A β 15 and A β 16 on the aggregation of full-length A β . An alternative pathway for their action could be related to the metal-binding site in the N-terminus of A β ^[27,35-49]. The fragments A β 15 and A β 16 contain all ligands that were proposed for binding Cu (II) and Zn (II) ions that were suggested to increase A β aggregation. The short fragments could reduce A β aggregation, because they scavenge the metal ions making the full-length A β less prone to aggregation.

Overall, the present EPR investigation suggests that the short peptides A β 15 or A β 16 do not influence the aggregation of A β 40 directly, supporting the view that physiological effects of these shorter fragments occur via a different route, possibly via metal-ion interactions. Therefore, examining the effect of metal ions on the aggregation of A β 40 in the presence of the short peptides A β 15 or A β 16 is suggested as a future line of investigation.

Reference List

- [1] K. Chopra, S. Misra, A. Kuhad, *Expert.Opin.Ther.Targets*. **2011**, 15 535-555.
- [2] R. Jakob-Roetne, H. Jacobsen, *Angew.Chem.Int.Ed Engl*. **2009**, 48 3030-3059.
- [3] F. Panza, V. Solfrizzi, V. Frisardi, C. Capurso, A. D'Introno, A. M. Colacicco, G. Vendemiale, A. Capurso, B. P. Imbimbo, *Drugs Aging* **2009**, 26 537-555.
- [4] D. J. Selkoe, *Ann.Intern.Med*. **2004**, 140 627-638.
- [5] D. J. Selkoe, *Neuron* **1991**, 6 487-498.
- [6] E. Portelius, G. Brinkmalm, A. Tran, U. Andreasson, H. Zetterberg, A. Westman-Brinkmalm, K. Blennow, A. Ohrfelt, *Exp.Neurol*. **2010**, 223 351-358.
- [7] E. Portelius, N. Mattsson, U. Andreasson, K. Blennow, H. Zetterberg, *Curr.Pharm.Des* **2011**, 17 2594-2602.
- [8] A. Awasthi, Y. Matsunaga, T. Yamada, *Exp.Neurol*. **2005**, 196 282-289.
- [9] E. Portelius, H. Zetterberg, U. Andreasson, G. Brinkmalm, N. Andreassen, A. Wallin, A. Westman-Brinkmalm, K. Blennow, *Neurosci.Lett*. **2006**, 409 215-219.
- [10] C. Soto, G. P. Saborio, B. Permanne, *Acta Neurol.Scand.Suppl* **2000**, 176 90-95.
- [11] Y. Matsunaga, A. Fujii, A. Awasthi, J. Yokotani, T. Takakura, T. Yamada, *Regul.Pept*. **2004**, 120 227-236.
- [12] J. F. Leverone, E. T. Spooner, H. K. Lehman, J. D. Clements, C. A. Lemere, *Vaccine* **2003**, 21 2197-2206.
- [13] H. Li, J. Zou, Z. Yao, J. Yu, H. Wang, J. Xu, *J.Neuroimmunol*. **2010**, 219 8-16.
- [14] R. Liu, C. McAllister, Y. Lyubchenko, M. R. Sierks, *J.Neurosci.Res*. **2004**, 75 162-171.
- [15] M. Q. Liao, Y. J. Tzeng, L. Y. Chang, H. B. Huang, T. H. Lin, C. L. Chyan, Y. C. Chen, *FEBS Lett*. **2007**, 581 1161-1165.
- [16] X. T. Du, L. Wang, Y. J. Wang, M. Andreasen, D. W. Zhan, Y. Feng, M. Li, M. Zhao, D. Otzen, D. Xue, Y. Yang, R. T. Liu, *J.Alzheimers Dis*. **2011**, 27 401-413.
- [17] A. N. Istrate, P. O. Tsvetkov, A. B. Mantsyzov, A. A. Kulikova, S. A. Kozin, A. A. Makarov, V. I. Polshakov, *Biophys.J*. **2012**, 102 136-143.
- [18] P. O. Tsvetkov, A. A. Kulikova, A. V. Golovin, Y. V. Tkachev, A. I. Archakov, S. A. Kozin, A. A. Makarov, *Biophys.J*. **2010**, 99 L84-L86.
- [19] S. Zirah, S. A. Kozin, A. K. Mazur, A. Blond, M. Cheminant, I. Segalas-Milazzo, P. Debey, S. Rebuffat, *J.Biol.Chem*. **2006**, 281 2151-2161.
- [20] I. Sepkhanova, M. Drescher, N. J. Meeuwenoord, R. W. A. L. Limpens, R. I. Koning, D. V. Filippov, M. Huber, *Applied Magnetic Resonance* **2009**, 36 209-222.
- [21] M. Margittai, R. Langen, *Q.Rev.Biophys*. **2008**, 41 265-297.
- [22] F. Scarpelli, M. Drescher, T. Rutters-Meijneke, A. Holt, D. T. Rijkers, J. A. Killian, M. Huber, *J.Phys.Chem.B* **2009**, 113 12257-12264.
- [23] D. C. Rambaldi, A. Zattoni, P. Reschiglian, R. Colombo, L. E. De, *Anal.Bioanal.Chem*. **2009**, 394 2145-2149.
- [24] A. L. Cloe, J. P. Orgel, J. R. Sachleben, R. Tycko, S. C. Meredith, *Biochemistry* **2011**, 50 2026-2039.
- [25] S. Stoll, A. Schweiger, *Journal of Magnetic Resonance* **2006**, 178 42-55.
- [26] S. Steigmiller, M. Börsch, P. Gräber, M. Huber, *Biochim.Biophys.Acta* **2005**, 1708 143-153.
- [27] Q. F. Ma, J. Hu, W. H. Wu, H. D. Liu, J. T. Du, Y. Fu, Y. W. Wu, P. Lei, Y. F. Zhao, Y. M. Li, *Biopolymers* **2006**, 83 20-31.
- [28] M. N. Oda, T. M. Forte, R. O. Ryan, J. C. Voss, *Nat.Struct.Biol*. **2003**, 10 455-460.
- [29] H. LeVine, III, *Protein Sci*. **1993**, 2 404-410.
- [30] H. Naiki, K. Higuchi, M. Hosokawa, T. Takeda, *Analytical Biochemistry* **1989**, 177 244-249.
- [31] K. Broersen, F. Rousseau, J. Schymkowitz, *Alzheimers Res.Ther*. **2010**, 2 12.
- [32] K. Broersen, W. Jonckheere, J. Rozenski, A. Vandersteen, K. Pauwels, A. Pastore, F. Rousseau, J. Schymkowitz, *Protein Eng Des Sel* **2011**, 24 743-750.
- [33] M. L. Giuffrida, F. Caraci, B. Pignataro, S. Cataldo, B. P. De, V. Bruno, G. Molinaro, G. Pappalardo, A. Messina, A. Palmigiano, D. Garozzo, F. Nicoletti, E. Rizzarelli, A. Copani, *J.Neurosci*. **2009**, 29 10582-10587.

- [34] A. Paivio, J. Jarvet, A. Gräslund, L. Lannfelt, A. Westlind-Danielsson, *Journal of Molecular Biology* **2004**, 339 145-159.
- [35] O. N. Antzutkin, *Magnetic Resonance in Chemistry* **2004**, 42 231-246.
- [36] C. S. Atwood, R. C. Scarpa, X. Huang, R. D. Moir, W. D. Jones, D. P. Fairlie, R. E. Tanzi, A. I. Bush, *J.Neurochem.* **2000**, 75 1219-1233.
- [37] C. C. Curtain, F. Ali, I. Volitakis, R. A. Cherny, R. S. Norton, K. Beyreuther, C. J. Barrow, C. L. Masters, A. I. Bush, K. J. Barnham, *J.Biol.Chem.* **2001**, 276 20466-20473.
- [38] P. Dorlet, S. Gambarelli, P. Faller, C. Hureau, *Angew.Chem.Int.Ed Engl.* **2009**, 48 9273-9276.
- [39] J. A. Duce, A. Tsatsanis, M. A. Cater, S. A. James, E. Robb, K. Wikhe, S. L. Leong, K. Perez, T. Johanssen, M. A. Greenough, H. H. Cho, D. Galatis, R. D. Moir, C. L. Masters, C. McLean, R. E. Tanzi, R. Cappai, K. J. Barnham, G. D. Ciccotosto, J. T. Rogers, A. I. Bush, *Cell* **2010**, 142 857-867.
- [40] E. House, J. Collingwood, A. Khan, O. Korchazkina, G. Berthon, C. Exley, *J.Alzheimers.Dis.* **2004**, 6 291-301.
- [41] X. Huang, C. S. Atwood, R. D. Moir, M. A. Hartshorn, R. E. Tanzi, A. I. Bush, *J.Biol.Inorg.Chem.* **2004**, 9 954-960.
- [42] D. Jiang, X. Li, L. Liu, G. B. Yagnik, F. Zhou, *J.Phys.Chem.B* **2010**, 114 4896-4903.
- [43] T. Kowalik-Jankowska, M. Ruta, K. Wisniewska, L. Lankiewicz, *J.Inorg.Biochem.* **2003**, 95 270-282.
- [44] T. Kowalik-Jankowska, M. Ruta, K. Wisniewska, L. Lankiewicz, M. Dyba, *J.Inorg.Biochem.* **2004**, 98 940-950.
- [45] S. A. Kozin, Y. V. Mezentsev, A. A. Kulikova, M. I. Indeykina, A. V. Golovin, A. S. Ivanov, P. O. Tsvetkov, A. A. Makarov, *Mol.Biosyst.* **2011**, 7 1053-1055.
- [46] B. K. Shin, S. Saxena, *Biochemistry* **2008**, 47 9117-9123.
- [47] C. D. Syme, R. C. Nadal, S. E. J. Rigby, J. H. Viles, *Journal of Biological Chemistry* **2004**, 279 18169-18177.
- [48] P. O. Tsvetkov, I. A. Popov, E. N. Nikolaev, A. I. Archakov, A. A. Makarov, S. A. Kozin, *Chembiochem* **2008**, 9 1564-1567.
- [49] H. Yu, J. Ren, X. Qu, *Chembiochem* **2008**, 9 879-882.

CHAPTER 5

ELUCIDATING THE α -SYNUCLEIN FIBRIL FOLD WITH PULSED EPR

Amyloid fibrils are constituents of the plaques that are the hallmarks of neurodegenerative diseases. In Parkinson's disease, these plaques (Lewy bodies) consist predominantly of the α -synuclein (α S) protein. To understand how the aggregation occurs and to interfere with the process of aggregation, the structure of the fibrils needs to be known. Here we study the molecular architecture of the fibrils of α S by measuring distances between pairs of residues in the protein using double electron-electron paramagnetic resonance (DEER). Site-specific spin labeling was employed to create nine doubly labeled α S variants, which were investigated in the fibrillar state. Diamagnetic dilution with wild type α S suppressed inter-molecular interactions. The intra-molecular distances provide constraints for the fold of the protein inside the fibril. Intra-molecular distances were unambiguously determined for four pairs 41/69, 56/69, 56/90, and 69/90. Three of these distances provide the constraints to suggest a model for the fold between residues 56 and 90 in the fibril.

Maryam Hashemi Shabestari, Ine M.J. Segers-Nolten, Mireille M.A.E. Claessens, Bart D. van Rooijen, Vinod Subramaniam, Martina Huber.

5.1 Introduction

Alpha-synuclein (α S) is a protein of 140 amino-acid residues. The α S protein is implicated in Parkinson's disease and is the major component of the Lewy Bodies characteristic of Parkinson's disease^[1]. The α S protein is natively disordered with no distinct secondary structure in solution. It acquires an α -helical structure on membranes. When α S forms fibrils, individual β -strands stack perpendicular to the fibril axis and form a cross β -sheet structure^[2,3]. It is important to understand the architecture of the fibril and to identify the residues that are crucial for the fibrillization. As yet, detailed information about the structure and fold of the protein in the fibrils is missing. Results from solid state NMR and EPR studies have identified residues involved in the β -sheet^[4,5] and proposals for the fold of stretches of residues in close contact were made^[6,7]. Owing to the absence of long-range constraints, modeling the exact extent of the stretches is difficult. In this work, we focus on the fold of α S in the fibril, by measuring intra-molecular distances in fibrillized doubly labeled α S with a pulsed EPR method, DEER. Recently, distance constraints involving residues located at the external β -strands were reported using the same approach^[8].

We investigate nine doubly labeled α S variants, α S9/69, α S9/90, α S18/69, α S18/90, α S27/56, α S41/69, α S56/69, α S56/90, and α S69/90. From the set of nine mutants, four, α S41/69, α S56/69, α S56/90, and α S69/90, have intra-molecular distances within the measurement range of the experiment. Based on the DEER distance data and combined with a triangulation approach, we construct a model of the fold of α S in the fibril using a set of three intra-molecular distances: α S56/69, α S56/90, and α S69/90.

The present study shows that even for such challenging repetitive protein structures a few long-distance constraints from DEER experiments are sufficient to obtain structural detail of fibrils that comprises most of the strands considered in the present models.

5.2 Materials and methods

5.2.1 Expression and purification of cysteine variants of α S

Single and double cysteine mutations were introduced into the α S gene by site directed mutagenesis. Mutants were expressed in *Escherichia coli* strain BL21(DE3) and subsequently purified in the presence of 1 mM DL-Dithiothreitol (DTT)^[9,10]. Prior to labeling, α S mutant proteins were reduced with a six-fold molar excess (per cysteine) of DTT for 30 minutes at room temperature. Subsequently, samples were desalted on Pierce Zeba 5 mL desalting columns,

followed by an immediate addition of a six-fold molar excess (per cysteine) of the MTS spin label ((1-oxyl-2,2,5,5-tetramethylpyrroline-3-methyl) methanethiosulfonate) and incubated for one hour in the dark at room temperature. Free label was removed using two additional desalting steps. Protein samples were applied onto Microcon YM-100 spin columns to remove any precipitated and/or oligomerized proteins and diluted into 10 mM Tris-HCl, pH 7.4 to typical protein concentrations of approximately 0.25 mM ^[11].

5.2.2 Preparation and harvesting of fibrillar α S

Fibrils of α S were formed by incubating monomer solutions at a total protein concentration of 100 μ M. Due to the stacking of proteins along the fibril axis, discrimination between intra- and inter-molecular distances is necessary. Therefore, the spin-labeled variants were co-fibrillized with the wild type α S protein (diamagnetic dilution). Different diamagnetic dilution ratios ranging from 1 in 5 to 1 in 20 were employed to ensure that the obtained distances represent the intra-molecular distances. Fibrils of all mutants were prepared using a diamagnetic dilution of 10 μ M MTS labeled α S (SL- α S) in the presence of 90 μ M wild type α S (1 in 10). For selected mutants, fibrillization of the double cysteine mutants was carried out in a 1 in 20 diamagnetic dilution, using 5 μ M doubly labeled SL- α S together with 95 μ M wild type protein. The corresponding single cysteine mutants were fibrillized in a 1 in 10 ratio, to keep the spin-label concentrations comparable. For the diamagnetic dilution series, fibrils were prepared with 20 μ M α S56/69 and 80 μ M wild type (1 in 5), 10 μ M α S56/69 and 90 μ M wild type (1 in 10) and 5 μ M α S56/69 and 95 μ M wild type (1 in 20). The aggregations were performed in 10 mM Tris-HCl, 50 mM NaCl, pH 7.4 buffer at 37° C in 2 ml LoBind Eppendorf tubes with constant shaking at 1000 rpm in a Thermo mixer (Eppendorf). The time evolution of α S aggregation was monitored by the standard Thioflavin T (ThioT) fluorescence assay ^[12,13]. The fibrillization was generally completed in three to four days. The α S fibrils were harvested by centrifuging for 90 minutes at 18,000 g in an Eppendorf microcentrifuge. The supernatant was carefully removed, leaving a fibril pellet typically with a volume of 80-100 μ l. The fibril pellet was used in the cw EPR and DEER measurements. Every mutant was fibrillized at least two times.

5.2.3 Atomic force microscopy (AFM)

The formation of α S fibrils was confirmed by tapping mode AFM in air. Aggregation aliquots were diluted in 10 mM Tris, 50 mM NaCl, pH 7.4, adsorbed onto mica, washed twice with 100 μ l MilliQ water and gently dried under nitrogen gas. Tapping mode AFM height images were made on a custom built instrument

[9,14]. SPIP software (Image Metrology A/S, Lyngby, Denmark) was used for visualization.

5.2.4 Continuous-wave EPR at 80 K and at room temperature

The X-band cw EPR measurements were performed using an Elexys E680 spectrometer (Bruker, Rheinstetten, Germany) with a rectangular cavity, using a modulation frequency of 100 kHz. For measurements at 80 K a helium gas-flow cryostat (Oxford Instruments, United Kingdom) with an ITC502 temperature controller (Oxford Instruments, United Kingdom) was used. For the measurements in frozen solution, 3 mm outer diameter quartz sample tubes were used. To obtain a frozen glass 20 % glycerol was added to the samples before freezing them in liquid nitrogen. The frozen samples were inserted in the pre-cooled helium gas-flow cryostat. The EPR spectra were recorded using a modulation amplitude of 2 G and a microwave power of 0.159 mW. Typical accumulation times were 40 minutes. For room temperature measurements, 10-15 μ l samples of α S fibrils were drawn into Blaubrand 50 μ l capillaries. The accumulation time for the spectra was 40 minutes per spectrum. Measurements were done at 20° C, using 6.331 mW of microwave power and a modulation amplitude of 1.4 G.

5.2.5 DEER measurements

The DEER measurements were performed at X-band (9.5 GHz) on an Elexsys E680 spectrometer (Bruker, Rheinstetten, Germany) using a 3 mm split-ring resonator (ER 4118XMS-3-W1). The temperature was kept at 40 K with a helium gas stream using a CF935 (Oxford Instruments, United Kingdom) cryostat with an ITC502 temperature controller (Oxford Instruments, United Kingdom). Samples, to which 20 % glycerol was added, were prepared in 3 mm outer diameter quartz tubes and were frozen in liquid nitrogen before inserting them into pre-cooled helium gas-flow cryostat. The pump and observer frequencies were separated by 70 MHz and adjusted as reported before [11]. The pump-pulse power was adjusted to invert the echo maximally [15]. The lengths of the pulses at the observer frequencies were 16 and 32 ns for $\pi/2$ - and π -pulses, respectively. The pump pulse length was 12 ns. All the DEER measurements were performed as two-dimensional experiments, in order to suppress the proton modulation. The DEER time traces were measured for ten different τ_1 -values spaced by 8 ns starting at $\tau_1 = 200$ ns. The typical accumulation times per sample were 16 hours. DEER data were analyzed using the “DeerAnalysis” program 2011 [16], which is available from www.epr.ethz.ch/software/index. After background correction of the data using the experimental background,

obtained from the singly labeled α S samples, the distance distribution was determined by Tikhonov regularization ^[15,16].

5.2.6 General structure parameters of fibrils

Generally accepted parameters ^[17] of the parallel β -sheet architecture of amyloid fibrils are the intra-sheet distance d of 1.09 nm, and the distance between two neighbors in the sequence within a strand l of 0.35 nm ^[17] (see results). From the distance l and the number of intervening residues between a pair of spin labeled residues, the distance expected between two labeled residues on the same strand was determined. For the model of the fibril, three orientations of the linker were considered per residue, each 120° apart with the linker in the same plane as the protein. Nine unique relative linker orientations are possible in that case.

5.3 Results

We have investigated nine doubly labeled α S variants, α S9/69, α S35/60, α S18/69, α S18/90, α S27/56, α S41/69, α S56/69, α S56/90, and α S69/90. These proteins are fibrillized in the presence of wild type α S (diamagnetic dilution) under the conditions explained in materials and methods.

The rate of formation of the α S fibrils is checked by the thioflavin T fluorescence assay ^[12,13]. No significant difference in the rate of fibril formation is observed for all samples, irrespective of the spin-label position and the degree of diamagnetic dilution. The morphology of the fibrils is checked by atomic force microscopy (AFM). As seen by AFM (figure 5.1) the morphology of the wild type and the spin-labeled mutants is similar, revealing that the spin label does not affect the fibrillization. The α S fibrils are investigated with continuous-wave and pulsed EPR.

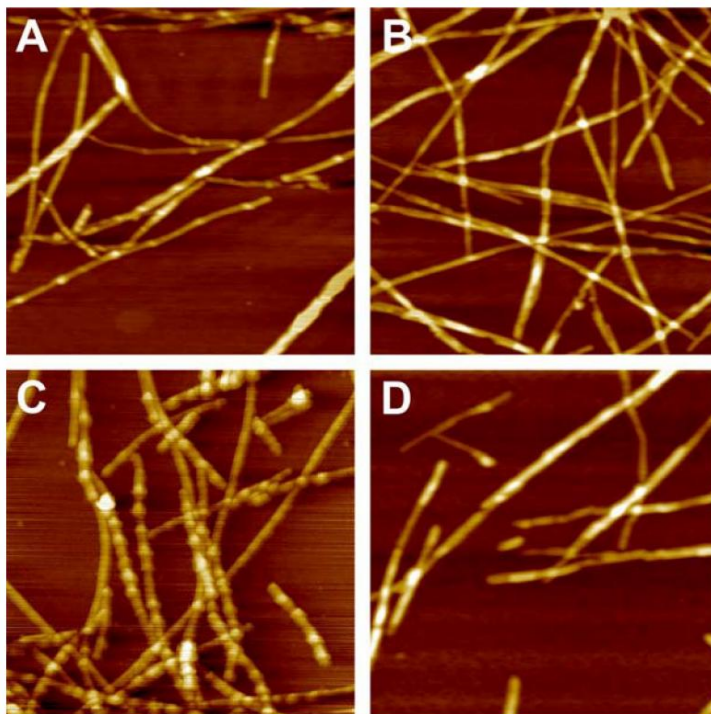


Figure 5.1 AFM images (A-D) of fibrils. A: α S56, at diamagnetic dilution 1 in 20, B: α S56/69 at 1 in 10, C: α S56/90 at 1 in 10, D: α S69/90 at 1 in 20. All images are $2.5 \times 2.5 \mu\text{m}^2$. Height information is rendered by the density of the color. Range: 0 to 10 nm.

5.3.1 Continuous-wave EPR

The continuous wave EPR spectra of the harvested fibrils of the α S56/69, α S56/90, and α S69/90 mutants with their singly labeled counterparts, α S56, α S69, and α S90 in liquid solution (left) and in frozen solution (right) are shown in figure 5.2. The liquid solution spectra have broadened lines with respect to those of the non-fibrillized α S protein. Simulation shows that the line-shape is fully explained by a reduced mobility of the spin label. This indicates that the broadening is caused by partial immobilization of the spin label due to fibrillization rather than spin-spin interaction. The narrow lines marked in figure 5.2 are indicative of the presence of monomers in the fibril sample. According to the simulation, the harvested fibrils contain less than 10 % of non-fibrillized protein.

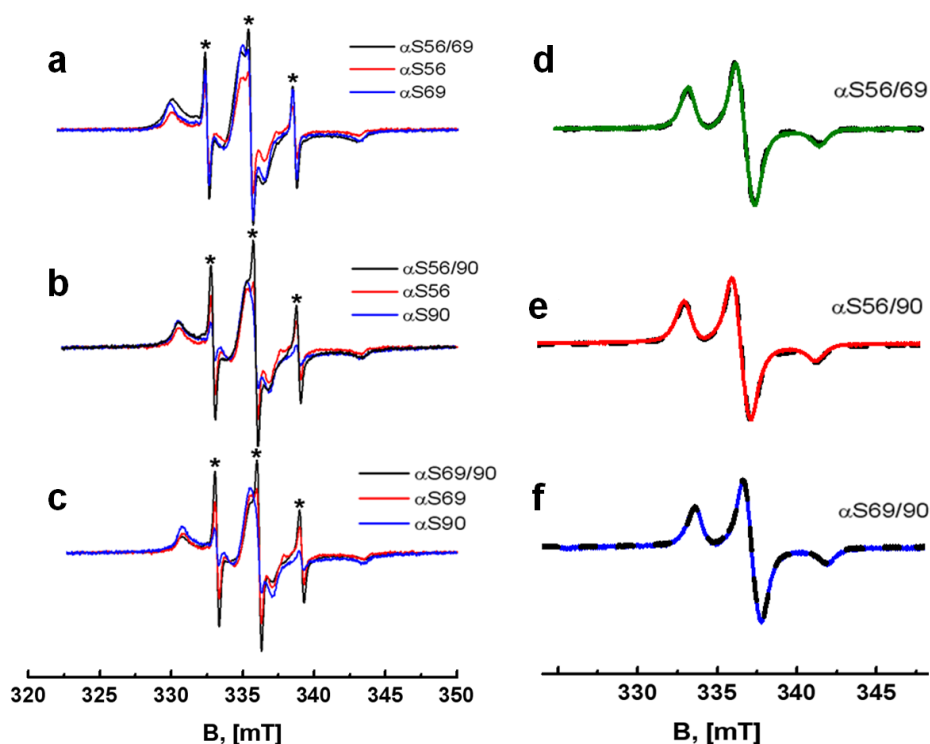


Figure 5.2 Continuous wave EPR spectra of the harvested fibrils of α S in a 1 in 10 diamagnetic dilution. a to c: Room temperature spectra of fibrils of doubly labeled α S with the corresponding singly labeled counterparts. Narrow lines, marked by an asterisk, stem from a small (less than 10 %) contribution of non-fibrillized proteins. a: α S56/69 superimposed with α S56 and α S69, b: α S56/90 superimposed with α S56 and α S90, c: α S69/90 superimposed with α S69 and α S90. d to f: Frozen solution EPR spectra of the doubly labeled α S proteins with the 1:1 added spectra of the respective singly labeled counterparts. d: α S56/69 (green) superimposed with α S56 plus α S69 (black), e: α S56/90 (red) superimposed with α S56 plus α S90 (black), f: α S69/90 (blue) superimposed with α S69 plus α S90 (black).

Frozen solution cw EPR spectra are superimposed with the 1:1 added spectra of the respective singly labeled counterparts. The absence of line broadening in the frozen solution spectra of the samples of fibrils with doubly labeled proteins compared to those of the singly labeled samples is evidence for the absence of distances shorter than 1.5 nm^[4,5].

5.3.2 Pulsed EPR

The DEER time traces of all mutants are shown in figure 5.3. The DEER time traces of α S9/69, α S18/69, and α S18/90 have a shallow decay, i.e., small modulation depth, which is an indication that a large fraction of the population has distances outside the measurement range, i.e., shorter than 1.8 nm or longer than 5

nm. The absence of line broadening in frozen solution, cw EPR shows that there are no distances shorter than 1.5 nm. Therefore, the majority of the population with distances outside the measurement range must have distances longer than 5 nm. The DEER time traces of the other mutants have a larger modulation depth. Some of those traces show signatures of DEER modulation, for example the steep decay at about 0.35 μ s for α S56/69.

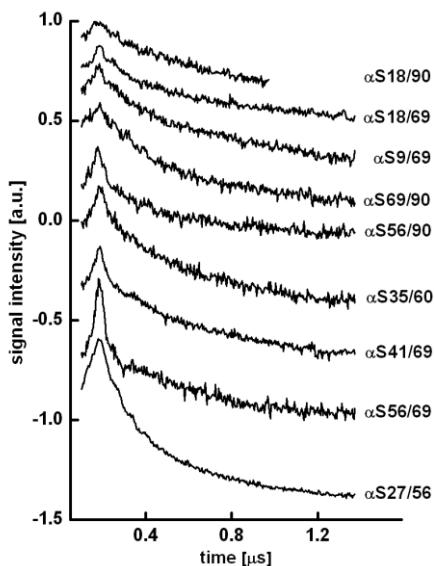


Figure 5.3 The DEER time traces for α S18/90, α S18/69, α S9/69, α S69/90, α S56/90, α S35/60, α S41/69, α S56/69, and α S27/56. All samples are in a 1 in 10 (spin-labeled α S in total α S) diamagnetic dilution, except for the α S35/60 mutant in which the dilution is 1 in 20. The maximum intensity of the DEER traces is normalized to one, by dividing the trace by the maximum of its intensity. DEER time traces are vertically shifted with respect to each other for better visibility.

Of the mutants analyzed, we focus the description on those with a large modulation depth, mutants α S56/69, α S56/90, α S69/90, and α S41/69. The α S18/69 is used as a reference for the mutants with low modulation depth. Figure 5.4 shows the steps in the analysis of the DEER time traces. All traces are background corrected with a 1:1 ratio of the background derived from the DEER curves of the respective singly labeled α S variants, which were fibrillized under the same conditions as the doubly labeled counterparts (for details see figure caption). Distances below 2 nm cannot be reliably determined under the conditions of the DEER experiments ^[18].

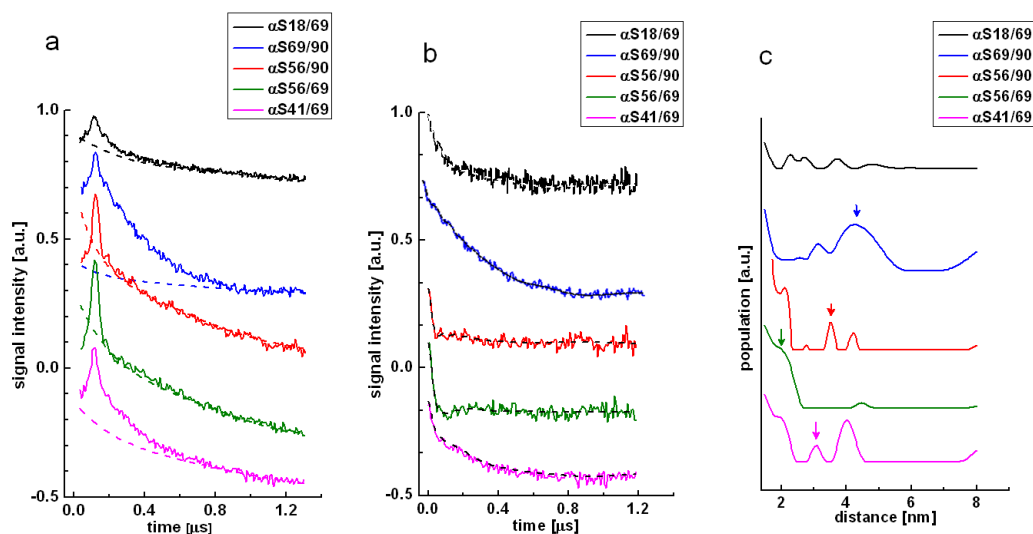


Figure 5.4 The DEER time traces for mutants α S18/69, α S69/90, α S56/90, α S56/69, and α S41/69. Shown are: a: DEER time traces. The background is shown as a dotted line. Backgrounds are the 1:1 added background traces of fibrils of the respective singly labeled α S. The background correction is done by dividing the data by the experimental background. Spin-label dilutions are 1 in 20 (spin-labeled α S in total α S) except for α S18/69 and α S41/69, which are 1 in 10. The maximum intensity of the DEER time traces is normalized to 1 and the traces are vertically shifted for better visibility. b: Baseline corrected DEER time traces and fit of the modulations to the data corresponding to the distance distributions shown in c. c: Distance distributions derived from the data. Arrows mark the distances identified as intra-molecular distances. Distributions were individually scaled to improve visibility.

To discriminate between intra- and inter-molecular distances, a set of diamagnetic dilutions is measured for the α S56/69 mutant (figure 5.5). The relative intensity of the peaks at 2.7 nm, 3.9 nm, and 4.5 nm compared to the 2.1 nm distance peak diminishes with increasing diamagnetic dilution, showing that the former peaks are due to inter-molecular interactions. These inter-molecular peaks are also found in the distance distributions of the corresponding singly labeled mutants, which confirm the inter-molecular character of these distances. As outlined below (see discussion) the intermolecular interactions should be independent of the mutant. Therefore, the inter-molecular distances identified for α S56/69 are also used in the interpretation of the distance distributions of the other mutants. Considering the signal-to-noise ratio of the time traces for the diamagnetic dilution of 1:20, higher dilutions do not seem feasible. The first screen of all mutants was performed at a 1:10 dilution to obtain a good signal-to-noise ratio. For selected mutants, α S56/69,

α S56/90, and α S69/90 the measurements were repeated at 1 in 20 dilution to improve the discrimination of intra- and inter-molecular distances.

Table 5.1 Distances from DEER experiments in nm compared to the expected distances for residues on the same β -strand.

mutants	intra-molecular DEER distances	distances expected for residues on the same β -strand
α S56/69	2.1	4.5
α S56/90	3.4	11.9
α S69/90	≥ 4.0	7.3
α S41/69	3.1	9.8

Figure 5.4.c shows the distance distributions for the mutants analyzed in detail. Intra-molecular distances are marked as arrows in figure 5.4.c. The α S18/69 mutant shows distances with similar intensities all over the accessible distance range. The same is true for α S27/56 (data not shown). The α S69/90 mutant shows two peaks, one around 2.6 nm and one around 4.2 nm. The second peak of the α S69/90 mutant corresponds to a larger population than the first peak. The α S56/90 mutant has a contribution at short distances (≤ 2.5 nm) that is very similar to the inter-molecular contribution in figure 5.5. The same is true for the lower intensity peak at 4 nm. This leaves the peak at 3.4 nm as an intra-molecular distance. The α S56/69 mutant shows a dominant distance peak around 2 nm, which is intra-molecular (see above). The α S41/69 mutant, which was fibrillized at a 1 in 10 diamagnetic dilution ratio, shows three peaks: one at distances longer than 4 nm, one around 2 nm, and one around 3 nm. The distance peaks at 2 nm and 4 nm are close to inter-molecular distance peaks as observed for α S56/69 at 1 in 10 diamagnetic dilution (figure 5.5). We therefore consider only the distance peak at 3 nm as intra-molecular. The α S27/56 mutant (with 1 in 10 diamagnetic dilution, data not shown) has a broad continuous distance distribution from 2 to 4 nm.

The intra-molecular distances are collected in table 5.1. They are compared to expected distances for residues on the same strand, which are calculated from the distance between two neighbors in the sequence within a strand, l ^[17] and the number of intervening residues (see materials and methods). The distances determined for all mutants listed in table 5.1 are shorter than the distances expected for residues on the same strand.

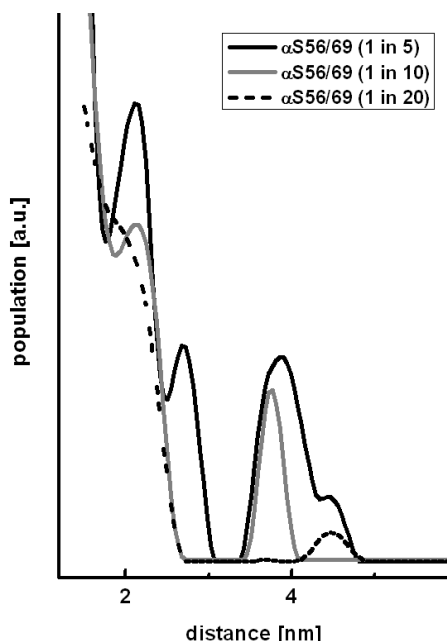


Figure 5.5 Distance distributions for the α S56/69 mutant with different diamagnetic dilutions.

5.4 Fibril fold model

Figure 5.6.a shows the schematic view of the protein in a plane perpendicular to the fibril axis as used in the model. In figure 5.6.b the β -sheets are shown in a side view of the protein fibril. The mutants α S56/69, α S56/90, and α S69/90 provide a set of three intra-molecular distances that define the corners of a triangle in a plane perpendicular to the fibril axis (figure 5.6.c). In a view along the fibril axis, the β -sheets appear as parallel strands. The triangle is rotated in the plane perpendicular to the fibril axis until each corner is as close as possible to one of the parallel strands. Thereby several orientations of the triangle are found. Arrangements in which residues are not sequential on successive parallel strands are excluded. We exclude these arrangements because such an arrangement would require that the protein exhibits too many turns for the distance. Also the solutions that involve residues on the same strand are excluded on the basis of the distances measured (table 5.1).

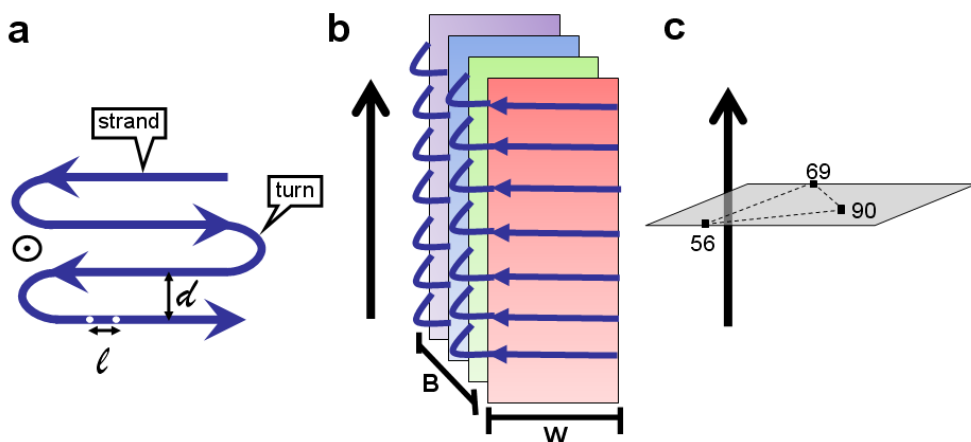


Figure 5.6 The cross- β -sheet structure of fibrils. a: View along fibril axis (fibril axis: black arrow that is pointing out of the page). Dark blue: protein. Strands and turns that connect the strands are labeled. l : distance between residues (dots) within the strand and d : distance between sheets. b: Fibril side view (fibril axis: black arrow), colored planes: β -sheets. Dark blue arrows: proteins making up the fibril. c: Location of residues 56, 69, and 90 assumed to make the model of the fibril.

Different spin-label linker orientations are considered to take the length of 0.5 nm from the protein C_β atom to the nitroxide group of the spin label into account (see materials and methods). We first describe the case in which all linkers point in the same direction. In total four solutions are found. In two of these solutions, residues 56 and 69 or 69 and 90 are on the same strand. Consequently, these solutions are discarded. The remaining two solutions are equivalent but they reflect different threading of the protein through the points (compare figure 5.7a to b). Starting at residue 56, the protein can be threaded on strand II in the direction away from the position of 69 (figure 5.7a). In this case, turns at residues 58 to 62, 70 to 74, and 85 to 89 (residue i and residue $i + 4$) are predicted. If the protein sequence is threaded on strand II in the direction towards the position 69 rather than away from that, a turn involving residues 74 to 78 and a strand of two residues followed by a turn at residues 80 to 84 is predicted (figure 5.7b). This leaves a stretch of residues from 86 to 90 uncomplemented by an opposite β -sheet. This scenario seems unlikely, and is therefore discarded.

The other set of linker orientations produce solutions shown in figure 5.8, depicted as orange, pink, purple, and green dots. For the solutions shown in orange and pink all three linkers point towards the same side of their respective strand, e.g. towards strand I. A fibril model similar to figure 5.7 results, although with shifted turn

positions (figure 5.9). If the linkers at residues 69 and 90 point into a direction, which is opposite to that of residue 56, i.e., to the other side of their strand than 56, an alternative fold is possible (figure 5.10). The main difference is that there is only one turn between residues 69 and 90. This solution is possible for two sets of orientations of linkers (green and purple dots in figure 5.10). The two solutions in figure 5.10 result from the two ways of threading the protein through the points. In this scenario, a stack of three β -sheets between residues 56 and 90 would result. The complete protofibril from residue 38 to 90 would have three or four stacked β -sheets leading to a thickness B (figure 5.6b) of the protofibril of 2.18 nm respectively 3.27 nm, smaller than the dimension B of protofibrils (about 5 nm) ^[7]. Therefore, the fold shown in figure 5.10 is not reasonable.

Considering the distances reported by Karyagina et al. ^[8] we extended the model shown in figure 5.7a towards residue 41. The distance we measured for α S41/69 (3.1 nm, table 5.1) suggests that residue 41, on strand I, could be facing residues 56 or 57 on strand II, (figure 5.7a) thus yielding a distance between residues 41 and 69 of 2.8 nm or 3.0 nm, respectively. For those arrangements of residue 41, the predicted separation between residues 41 and 90 would be about 4 nm, in good agreement with the result of 4.5 ± 0.5 nm reported by Karyagina et al. ^[8]. A stack of five β -sheets would have a B value of 4.36 nm, in good agreement with predicted protofibril dimensions ^[7].

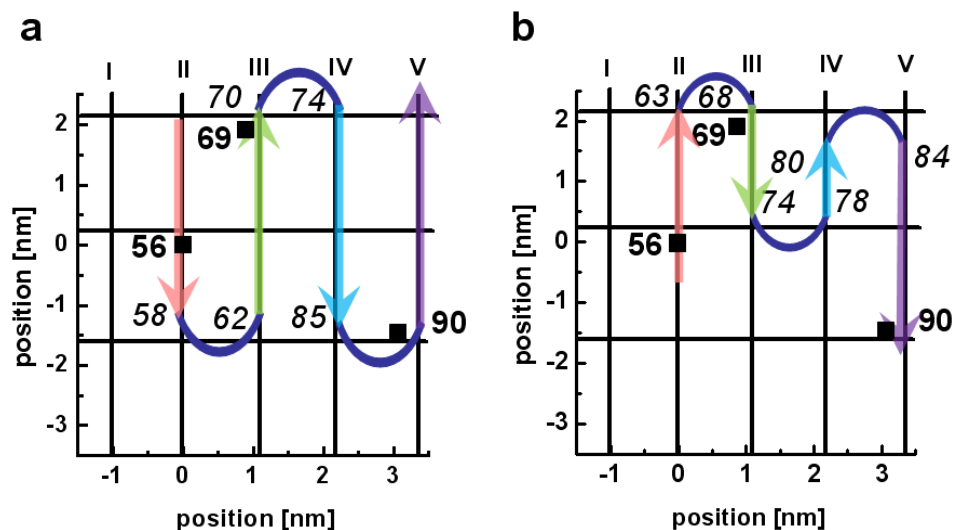


Figure 5.7 Models of the fold of α S in the fibril for all linkers pointing into the same direction. Strands are labeled I to V. Colored arrows indicate successive β sheets, and dark blue bent lines indicate turns. Italic numbers: residues at the start and the end of the turn. a: If the protein is threaded on strand II in the direction away from the position of 69, turns at residues 58 to 62, 70 to 74, and 85 to 89 are predicted. b: If the protein is threaded on strand II in the direction towards the position 69, a turn at residues 74 to 78 and a two-residue strand followed by a turn at residues 80 to 84 are predicted.

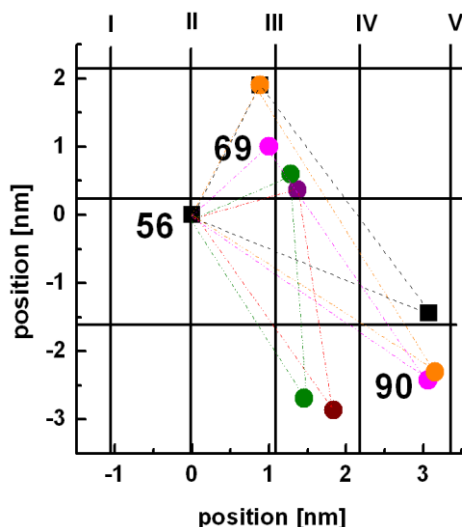


Figure 5.8 Effect of linker orientation on the position of residues 56, 69, and 90 with respect to the strands I to V. Dots in different colors show optimal positions found as acceptable solutions for the nine relative linker orientations. Lines joining positions (triangles) resulting for different linker orientations are given in the color used for the corresponding linker orientation. For details, see text.

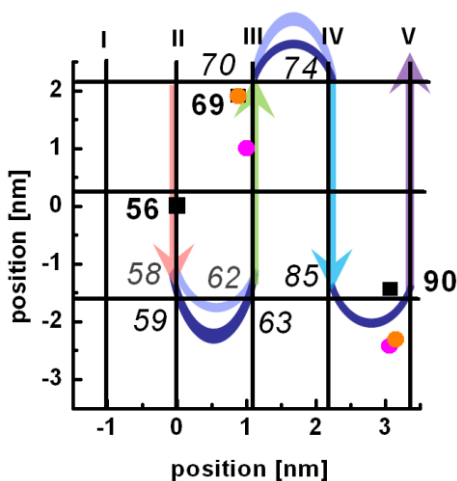


Figure 5.9 Effect of linker orientation on the model shown in figure 5.7.a. Pink and orange dots give the positions of residues 69 and 90 for two other orientations that are compatible with the fold obtained for parallel linkers. Orange dots show the position of residues if one or both linkers at 69 and 90 are almost parallel to the strand, but pointing towards the same side of the strands as the linker at residue 56. Black squares: positions shown in figure 5.7. The threading model is shown for the pink positions. Light-blue turns indicate the shift in the turn positions where strand IV is shifted by 2 residues relative to strand II, and turn positions differ by one (turn between strand II and III) and two residues (turn between strand IV and V). For position 69, the black square overlaps the orange dot.

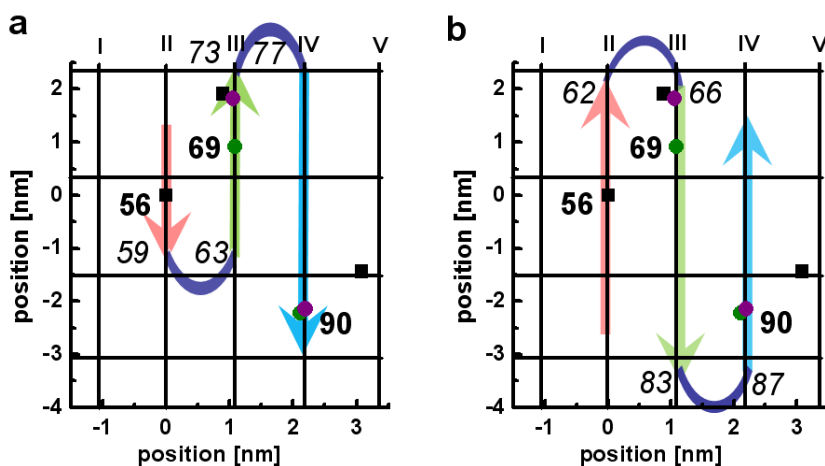


Figure 5.10 Alternative model of the α S fibril. a: Fold for linker orientations with the linker at residue 56 opposite to those at residues 69 and 90 for two different linker orientations (green and purple dots). b: Alternative way of threading the protein for the positions shown in a. The purple dot and the green dot labeled 69 are the alternative positions of residue 69. The black squares show the positions of residues 56, 69, and 90 in the model shown in figure 5.7.

5.5 Discussion

The morphology of the fibrils and the fibril growth are not affected by spin-label position or diamagnetic dilution as evidenced by the AFM and ThioT results. We therefore conclude that all mutants report on the same fibril morphology and that all distances can be used to derive a common model of the fold of the protein within the fibril. Fibrils of α -synuclein are in-register, parallel β -strand fibrils. Inter-molecular interactions of spin labels are therefore parallel to the fibril axis. This parallelism makes that inter-molecular distances reflect the inter-strand separation or multiples thereof and do not depend on the mutant, i.e., the residue of α -synuclein to which the spin label is attached. Therefore, inter-molecular distances identified from the diamagnetic-dilution series of α S56/69 are used also for the other double mutants. The best compromise between signal-to-noise and discrimination of intra- and inter-molecular distances is a diamagnetic dilution of 1 in 20.

For the mutants α S9/69, α S18/69, α S18/90, and α S27/56 one of the labeled positions is outside the region typically associated with the β -sheets of the α S fibrils, which ranges from residue 35-38 to 89-96 according to previous studies^[4,7,19]. All these mutants, with the exception of α S27/56, have a majority population with distances longer than 5 nm (see results). This shows that the non-fibril, N-terminal part of α S at least up to residue 18 extends away from the fibril core. Residue 27 behaves differently. The mutant α S27/56 has a broad, continuous distance distribution, revealing that the region close to residue 27 is disordered. Distances of the α S27/56 mutant, which are extending from 2 to 4 nm, suggest that the region around residue 27 is closer to the fibril core than residues at the N-terminus around residue 18. The information obtained from the mutants α S9/69, α S18/69, α S18/90, and α S27/56 suggests the picture of an unstructured N-terminus that extends away from the fibril core.

The experimentally determined distances for α S56/69, α S69/90, α S56/90, and α S41/69 are significantly shorter than the distances expected for residues on the same strand (table 5.1). These experimentally determined distances reveal that there must be minimally one turn between residues 41 and 56, 56 and 69 and between 69 and 90, i.e., there are at least three turns separating residue 41 and 90. This leads to the picture that there are at least four strands of β -sheets, where the first strand contains residue 41 and the last residue 90.

The model described in section 5.4 shows how the distances can be converted to a picture of the fibril fold. We stress that this model derives from the present set of

constraints. To prove or disprove the model additional distance restraints would be needed.

The model of the fold of α S in the fibril (figure 5.7.a), derived from the situation in which all linkers are pointing into the same direction, suggests that the protofibril consists of five stacked β -sheets (I to V), spanning residues 41 (not directly determined, but inferred to be located on strand I) to 90. This model is also robust for a series of spin-label linker orientations, in which linkers are pointing into different directions. At most, extreme linker orientations shift strands with respect to each other, by up to three residues (figure 5.9). Nevertheless, there are linker orientations that could result in a fold in which the protofibril from residue 41 to 90 consists of four rather than five stacked β -sheets. In figure 5.10.a and b only three of these strands (residue 56 to 90) are shown. Such a model would disagree with the outside fibril dimensions and is therefore excluded.

Overall the fold shown in figure 5.10.a is similar to that proposed by Vilar et al. ^[7], in that three turns separate the strands containing residue 56 and 90. In this model, the first turn, 56-62 agrees with our results, whereas the second turn, 66-68 is four residues earlier in sequence, and thus suggests that there is an intervening strand between residues 56 and 69. Because this arrangement aligns residues 56 and 69 in a direction perpendicular to the strand, it would not violate the 56-69 distance constraint obtained in the present study. However, the model proposed by Vilar et al. would disagree with the distance we determine between residues 56 and 90, suggesting it to be longer than the distance between 69 and 90. The scenario of Vilar et al. ^[7] in which the distance between residues 56 and 90 is longer than the distance between 69 and 90 is therefore not compatible with our data.

The model of Heise et al. ^[19], with turns at 65-69 and 82-87 again is compatible with the distance between 56 and 69, but not with the other distances. Unfortunately, the very recent model proposed by Comellas et al. ^[6], in which long and short β -strands alternate, cannot be checked against our data, because the overall arrangement of strands is not reported ^[6].

We show that a series of nine doubly labeled mutants of α S enables us to determine the fold of α S in the fibril, starting from the disordered N-terminus to the fibril core. We show that the N-terminus, presumably up to residue 27 is disordered and extends away from the fibril core. The β -sheet core from residue 41 to 90 comprises most likely five strands, leading to protofibril dimensions in agreement with previous results. This is the first step towards an atomic-resolution picture of the fibril core.

Reference List

- [1] V. V. Shvadchak, L. J. Falomir-Lockhart, D. A. Yushchenko, T. M. Jovin, *J.Biol.Chem.* **2011**, 286 13023-13032.
- [2] K. A. Conway, J. D. Harper, P. T. Lansbury, Jr., *Biochemistry* **2000**, 39 2552-2563.
- [3] L. C. Serpell, J. Berriman, R. Jakes, M. Goedert, R. A. Crowther, *Proc.Natl.Acad.Sci.U.S.A* **2000**, 97 4897-4902.
- [4] M. Chen, M. Margittai, J. Chen, R. Langen, *J.Biol.Chem.* **2007**, 282 24970-24979.
- [5] A. Der-Sarkissian, C. C. Jao, J. Chen, R. Langen, *J.Biol.Chem.* **2003**, 278 37530-37535.
- [6] G. Comellas, L. R. Lemkau, A. J. Nieuwkoop, K. D. Kloepper, D. T. Lador, R. Ebisu, W. S. Woods, A. S. Lipton, J. M. George, C. M. Rienstra, *J.Mol.Biol.* **2011**, 411 881-895.
- [7] M. Vilar, H. T. Chou, T. Luhrs, S. K. Maji, D. Riek-Loher, R. Verel, G. Manning, H. Stahlberg, R. Riek, *Proc.Natl.Acad.Sci.U.S.A* **2008**, 105 8637-8642.
- [8] I. Karyagina, S. Becker, K. Giller, D. Riedel, T. M. Jovin, C. Griesinger, M. Bennati, *Biophys.J.* **2011**, 101 L1-L3.
- [9] M. E. van Raaij, I. M. Segers-Nolten, V. Subramaniam, *Biophys.J.* **2006**, 91 L96-L98.
- [10] G. Veldhuis, I. Segers-Nolten, E. Ferlemann, V. Subramaniam, *Chembiochem* **2009**, 10 436-439.
- [11] M. Drescher, G. Veldhuis, B. D. van Rooijen, S. Milikisyants, V. Subramaniam, M. Huber, *J.Am.Chem.Soc.* **2008**, 130 7796-7797.
- [12] H. LeVine, III, *Protein Sci.* **1993**, 2 404-410.
- [13] H. Naiki, K. Higuchi, M. Hosokawa, T. Takeda, *Analytical Biochemistry* **1989**, 177 244-249.
- [14] K. O. Vanderwerf, C. A. J. Putman, B. G. Degrooth, F. B. Segerink, E. H. Schipper, N. F. Vanhulst, J. Greve, *Review of Scientific Instruments* **1993**, 64 2892-2897.
- [15] G. Jeschke, *Chemphyschem* **2002**, 3 927-932.
- [16] G. Jeschke, V. Chechik, P. Ionita, A. Godt, H. Zimmermann, J. Banham, C. R. Timmel, D. Hilger, H. Jung, *Applied Magnetic Resonance* **2006**, 30 473-498.
- [17] M. Margittai, R. Langen, *Q.Rev.Biophys.* **2008**, 41 265-297.
- [18] J. E. Banham, C. M. Baker, S. Ceola, I. J. Day, G. H. Grant, E. J. Groenen, C. T. Rodgers, G. Jeschke, C. R. Timmel, *J.Magn Reson.* **2008**, 191 202-218.
- [19] H. Heise, W. Hoyer, S. Becker, O. C. Andronesi, D. Riedel, M. Baldus, *Proc.Natl.Acad.Sci.U.S.A* **2005**, 102 15871-15876.

CHAPTER 6

EXPLORING THE STRUCTURE OF THE N-TERMINUS OF THE PLANT ANTENNA PROTEIN CP29

Recently, the crystal structure of the light-harvesting protein CP29 of plants was determined using X-ray crystallography (Pan et al., *Nat.Struct.Mol.Biol.* **2011**, 18, 309-315). However, the structure of the unusually long N-terminal domain of this membrane protein (about 100 amino-acid residues) remained elusive. We have studied the N-terminus with the use of electron paramagnetic resonance, EPR. Our study involves two approaches: exploring the mobility of the spin label with continuous wave EPR and distance determination with a pulsed EPR method. We demonstrate that the N-terminus of CP29 is relatively structured and five regions have been recognized that differ considerably in their dynamics. Two regions are relatively immobile and one of them shows alpha-helical character and is in contact with the bulk of the protein. This immobile part is flanked by highly dynamic and rather unstructured regions (loops) and we speculate that they may be important for the interaction with other light-harvesting proteins. A small part at the end of the N-terminus around residue 4 appears to be immobilized, presumably because it attaches non-covalently to the protein. This section of the N-terminus is close to a phosphorylation site (Thr-6) in related proteins (Fristedt et al., *PLoS One.* **2011**, 6, e24565), for example those encoded by the Lhcb4.2 gene. Phosphorylation might influence the interaction with other antenna complexes, thereby regulating the supramolecular organization in the thylakoid membrane.

Maryam Hashemi Shabestari, Cor J.A.M. Wolfs, Ruud B. Spruijt, Herbert van Amerongen, Martina Huber.

6.1 Introduction

In higher plants, photosynthesis is performed by two multiprotein complexes, photosystem (PS) I and II, which are composed of a core complex and an outer antenna part ^[1,2]. In PSII, the outer antenna system is built from a large number of complexes out of which the most relevant here are LHCII, the major antenna subunit, and three minor complexes, CP24, CP26, and CP29 ^[1,3]. Amongst the minor complexes, CP29 is the largest one and believed to collect, conduct, and possibly quench electronic excitation energy in photosynthesis ^[1,3-12]. Moreover, CP29 is essential for the proper assembly of PSII and its absence leads to a large drop in the average rate of excitation trapping in the reaction centers of PSII ^[10]. The membrane protein CP29 has five main membrane helices, helices A-E, three of which are trans-membrane and a long N-terminal domain with about 100 amino-acid residues (figure 6.1). The N-terminus contains a phosphorylation site which might be involved in the events occurring under high-light conditions ^[7] and its phosphorylation leads to a conformational change that can be detected with the use of circular dichroism ^[13]. The crystal structure of CP29 has recently been solved ^[14], with the exception of the N-terminal part, which lacked well-defined electron density. Sequence alignment suggests that the related antenna protein LHCII has a shorter N-terminus, in particular, it lacks the residues 58 to 97 that are present in the N-terminus of CP29 ^[15]. Therefore the better-characterized LHCII cannot be used as a model for the N-terminus of CP29.

Previous studies targeting the structure of the N-terminus of CP29 by FRET ^[8,10] and EPR ^[9] indicate that the N-terminus is folded back onto the protein and suggest the presence of some structural heterogeneity in the N-terminal part. In the present study, we employ spin-label EPR to learn more about the structure and dynamics of the N-terminus. Our study involves two approaches. Singly spin-labeled variants were used to study the mobility of the spin label by continuous-wave (cw) EPR and doubly spin-labeled variants were used to determine distances by double electron-electron resonance (DEER), a pulsed EPR method. To this aim, amino-acid residues were mutated one-by-one to a cysteine, spin labeled with a nitroxide spin label (i.e., site-directed spin labeling, SDSL), and reconstituted with the chlorophylls and carotenoids to form the holoprotein. In all cases this holoprotein was investigated. The present study demonstrates that the N-terminus of CP29 is relatively structured and consists of at least five different regions that differ in their secondary structure.

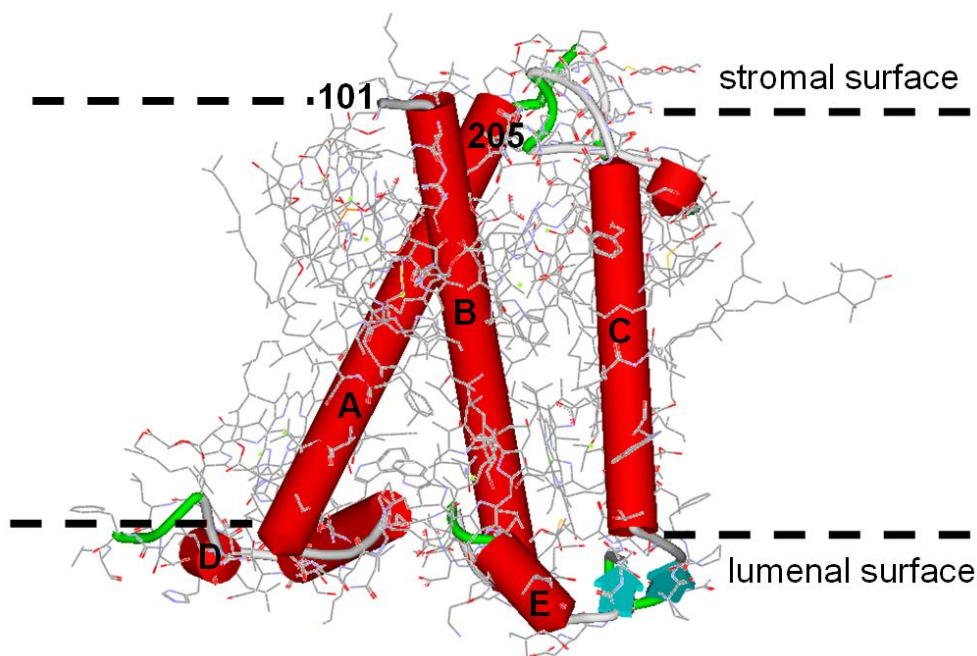


Figure 6.1 Schematic structural model of CP29 based on the X-ray structure of CP29. The five main helices (A-E) are shown in red. The N-terminus, consisting of residues 1-100, is not defined in the structure. Residue 101 is localized at the stromal surface of the protein, at the start of the helix B.

6.2 Materials and methods

6.2.1 Mutagenesis, labeling, and pigment reconstitution

The construction and isolation of overexpressed CP29 apoprotein from Lhcb4.1 cDNA of *Arabidopsis thaliana* (*A. Thaliana*) (from *Arabidopsis* Biological Resource Center DNA Stock Center) were performed as reported before ^[8,9]. The naturally occurring cysteine (position 108) was replaced by alanine. The mutant protein (C108A) was used to estimate the amount of nonspecific spin labeling ^[8,9]. Single cysteine mutants were introduced at 55 different positions in the N-terminus of the CP29 apoprotein using this template, resulting in the following mutants: G4C, G6C, A10C, A11C, S15C, A16C, T19C, V20C, T21C, T22C, P29C, G30C, A31C, I32C, S33C, G39C, S40C, L41C, V42C, G43C, G46C, F50C, G51C, L52C, G53C, A56C, E57C, Y58C, L59C, Q60C, F61C, S65C, Q68C, N69C, L70C, A71C, N73C, L74C, A75C, G76C, G80C, T81C, T83C, E84C, A85C, A86C, A88C, S90C, T91C, P92C, F93C, Q94C, S97C, G101C, C108C.

In the DEER experiments six different double cysteine mutants were investigated: G4C/S97C, G4C/G101C, G4C/A205C, A56C/S65C, A56C/T81C, and A56C/S97C.

Pigment isolation, labeling, and reconstitution of CP29 pigment complexes were performed as described before^[8,9]. Solutions of the spin-labeled CP29 samples were washed and concentrated in sucrose-free β -D-maltoside (DM) buffer (0.03 % W/V + 10 mM Na₂HPO₄, pH 7.6) just before the EPR measurements. Integrity of the holoprotein samples was checked by fluorescence excitation and emission measurements, showing the complete absence of free chlorophylls and carotenoids in all preparations.

6.2.2 Continuous-wave EPR measurements

The room temperature EPR measurements were performed on an X-band Bruker Elexsys E-500 EPR system (Bruker, Rheinstetten, Germany) equipped with a super-high-Q cavity ER 4122SHQE in combination with a SuperX X-band microwave bridge type ER 049X. Temperature was controlled with a quartz variable-temperature Dewar inset (Eurotherm, Leesburg, VA). Samples were transferred to 50 μ l capillaries and placed in a standard 4-mm quartz EPR tube. Spectra were recorded with 10 mT scan width, a microwave power of 5 mW, a modulation amplitude of 0.1 mT, and a scan time of 82 s at 279 K. Up to 150 scans were recorded to improve the signal/noise ratio^[9].

The measurements at 80 K were performed using an Elexsys E680 spectrometer (Bruker, Rheinstetten, Germany). A rectangular cavity, equipped with a helium gas-flow cryostat (Oxford Instruments, United Kingdom) with an ITC502 temperature controller (Oxford Instruments, United Kingdom) was used. For the measurements in frozen solution, 3 mm outer diameter quartz tubes were used. To obtain a frozen glass 20 % glycerol was added to the samples before freezing them in liquid nitrogen. The frozen samples were inserted in the pre-cooled helium gas-flow cryostat. The EPR spectra were recorded using a modulation amplitude of 0.2 mT, a modulation frequency of 100 kHz, and a microwave attenuation of 0.159 mW. Typical accumulation time was 40 minutes.

6.2.3 Simulation of the cw EPR spectra

Information on the mobility of the spin label is encoded in the line-shape of the EPR spectra. In case of a non-restricted spin label, the lines are narrow, whereas for a restricted spin label the lines are broad. A spectrum consists of different components, corresponding to fractions of the samples in which spin labels have different mobility. Each component in a spectrum is defined by a rotation correlation time, τ_r , of the spin label. Simulation enabled us to define the τ_r as well as the amount of each component. The spectra were simulated using Matlab and the EasySpin package^[16]. For all components the following parameters were used: $g = [2.00906, 2.00687, 2.003]$ ^[17] and $A_{xx} = A_{yy} = 13$ MHz. The value used for A_{zz} was

similar for the fast and medium component but different for the slow component, as discussed before ^[17]. Over-modulation effects were taken into account in EasySpin. The quality of the agreement between the experimental and the simulated lines was checked by visual inspection.

6.2.4 Assessment of the cw EPR spectra

A quick method to define the mobility of the spin label, rather than performing the relatively time-consuming simulations, was to measure amplitude ratios directly from the spectra ^[18,19]. Here we used the ratio of the mobile (R) component to the strongly immobilized (L) component (R/L). The contribution of these two components was obtained by selecting specific positions in the EPR spectra B_{0L} (the magnetic field value at the outermost left peak = 329.4 ± 0.1 mT) and B_{0R} (the magnetic field value at the second peak from the left = 330.5 ± 0.1 mT) at which one component has a large amplitude and the other a small one. The ratio of the amplitudes of the two selected spectral positions (R/L) gives an indication of the mobility. The larger the ratio, the higher the mobility is. Certain periodicities in the mobility of sequential residues indicate secondary-structure elements: a periodicity of 2.0 a β -sheet and a periodicity of 3.6 a regular α -helix.

Another measure of the mobility was obtained using the inverse of the central line width (ΔB^{-1} , mT^{-1}) ^[19,20] and the inverse of the second moment ($\langle \Delta B^2 \rangle^{-1}$, $\langle \text{mT}^2 \rangle^{-1}$) ^[21-23]. The ΔB^{-1} parameter ^[19,24] is the higher the more mobile the spin label is. A more detailed analysis ^[21-23] defines the main topographic regions of a protein in a plot of the ΔB^{-1} vs. the $\langle \Delta B^2 \rangle^{-1}$: loop/surface sites, loop/contact sites, helix/surface sites, and helix/buried sites. We refer to this plot as the Hubbell plot (see Results).

6.2.5 Parameters to estimate the length of protein regions

The distance between two successive C_α atoms, C_{ai} - C_{ai+1} , in a protein in the random-coil conformation is reported to be 0.38 nm, assuming that all amide groups are restricted to the trans conformation ^[25]. So if the N-terminus of the CP29 (about 100 amino-acid residues) was in a random coil conformation, it would have a length of about 38 nm. For comparison, the largest dimension of the stromal surface of the CP29 protein is about 3.2 nm (distance between the farthest two residues e.g. 164-188 or 88-180), which is about 1/10 of the maximum total length of the N-terminus. So the N-terminus is not likely to be in an extended conformation. The distance separating each turn of a helix in the direction of the cylindrical axis is 0.54 nm, which results in a distance of 0.15 nm/residue for the length of the α -helix. For loops, two extreme situations are considered, a fat and a thin loop, which are maximally extended horizontally and vertically with respect to the stromal surface, respectively. Assuming a minimal turn diameter of 0.8 nm, the horizontally

extended loop has a height of 0.8 nm covering at least two residues at both ends, which leaves for a loop of n_L residues, $n_L - 4$ residues for the width of the horizontal loop. For the vertically extended loop, the height and the width of a loop of n_L residues would be $\frac{1}{2} * n_L - 2$ and 0.8 nm, respectively. From these numbers the length of different sections of the protein can be estimated (see results).

6.2.6 Pulsed EPR measurements

The DEER measurements were performed at X-band on an Elexsys E680 spectrometer (Bruker, Rheinstetten, Germany) at frequencies of about 9.3 GHz using a 3 mm split-ring resonator. The temperature was kept at 40 K with helium gas in a CF935 (Oxford Instruments, United Kingdom) cryostat with an ITC502 temperature controller (Oxford Instruments, United Kingdom). Samples were prepared in 3 mm outer diameter quartz tubes and were frozen in liquid nitrogen before insertion into a pre-cooled helium gas-flow cryostat. The pump and observer frequencies were separated by 70 MHz and adjusted as reported before ^[26]. The power of the pump-pulse was adjusted to invert the echo maximally ^[27]. The lengths of the pulses at the observer frequency were 16 and 32 ns for the $\pi/2$ - and π -pulses. The length of the pump pulse was 12 ns. All DEER measurements were performed as two-dimensional experiments, in order to suppress the proton modulation ^[27]. The DEER time traces were measured for ten different τ_1 -values spaced by 8 ns starting at $\tau_1 = 200$ ns. The typical accumulation time per sample was 16 hours. The DEER data were analyzed using the “DeerAnalysis” program 2011 ^[28], which is available from www.epr.ethz.ch/software/index. After background correction of the data, the distance distribution was determined by Tikhonov regularization with an optimum regularization parameter determined by the L curve criterion ^[27,28]. Significance of features at long distances was checked with the validation tool in “DeerAnalysis”.

6.3 Results

6.3.1 Continuous-wave EPR

The cw EPR spectra of the reconstituted holoproteins in the detergent-micelle solution are shown in figure 6.2. The spectra differ substantially from each other. Some of them have particularly broad lines (e.g. the spectra of S33C and G101C). Others have sharp lines (e.g. the spectra of A10C and A86C). As seen from the residue numbers, broader lines occur throughout the N-terminus.

More detailed information is obtained by spectral simulation, performed for selected spectra. For each spectrum (figure 6.3) at least two components are required that differ in rotation-correlation time τ_r (table 6.1). The broad-line spectra of the spin label at residues 4, 40, and 101 are simulated with three components.

Each spectrum has a substantial slow component (at least 18 %) with a τ_r longer than 50 ns, and maximally 5 % of a fast component (τ_r of about 1 ns). In the spectra of the spin label at residues 11 and 86, the slow component is absent, which indicates the more mobile character of these positions. The spectra have almost equal contributions of a fast component with a τ_r of about 1 ns, and a medium component with a τ_r of about 4 ns. Also, the spectrum of the spin label at residue 70 consists of two components, only in this case the amount of the medium component (τ_r of about 4 ns) is significantly larger than that of the fast component (τ_r of about 1 ns) (table 6.1).

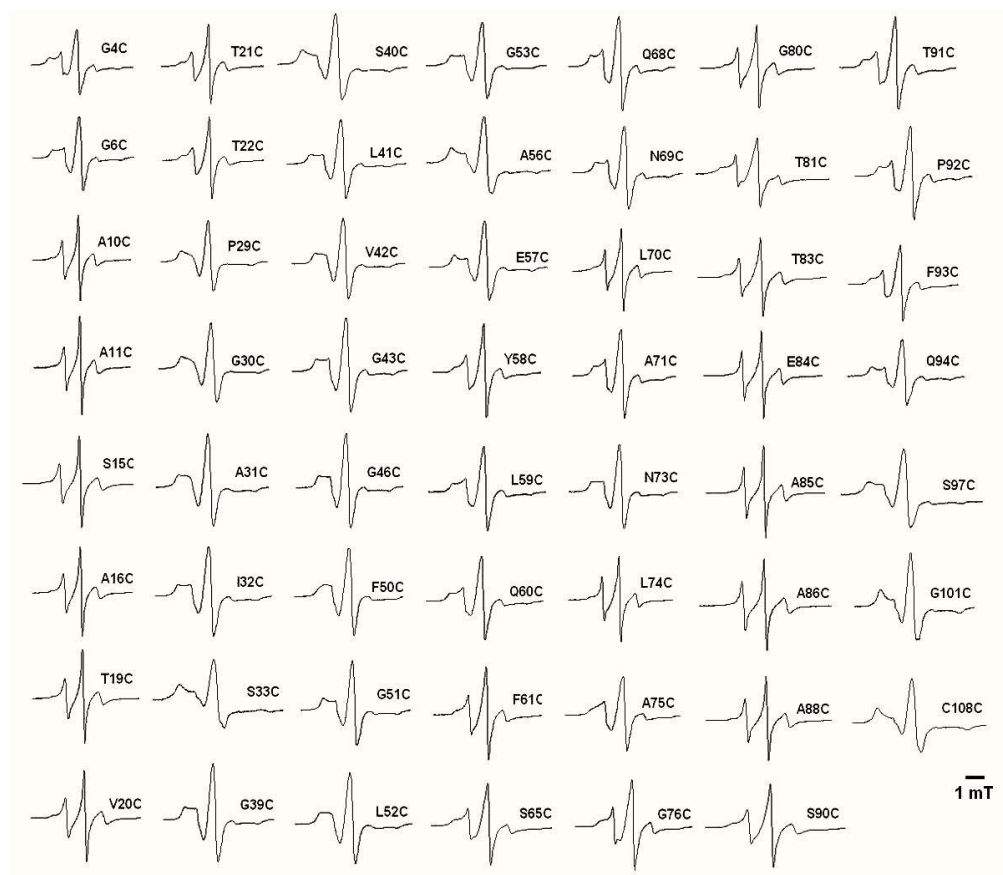


Figure 6.2 Room temperature EPR spectra of 55 singly labeled CP29 protein samples. In each spectrum the position of the nitroxide spin label is indicated.

Because of the multicomponent character of these spectra an easier approach, rather than the time-consuming simulation, is to compare the spectral intensities, R/L. The intensity at position R (figure 6.4 insert) derives from the fast and medium

components and at position L from the slow component. The higher the R/L ratio, the more mobile the spin label. The dependence of the R/L ratio is illustrated in figure 6.4 as a function of the residue number. It gives qualitative information, i.e., relative mobility of the stretch of protein investigated. Amongst the investigated residues (55 out of 110) about 40 % appeared to be immobile/ restricted, 35 % have intermediate mobility and only 25 % are highly mobile. Ultimately, also including the further analysis (see below), five distinct mobility regions are determined within the N-terminus: I: residues 10 to 22, II: residues 23 to 57, III: residues 58 to 81, IV: residues 82 to 91, and V: residues 92 and 108 (figure 6.4). Region V includes a stretch of residues (101-108) assigned to the transmembrane helix B, which extends from residue 101 onwards. The borders between regions are not precisely defined.

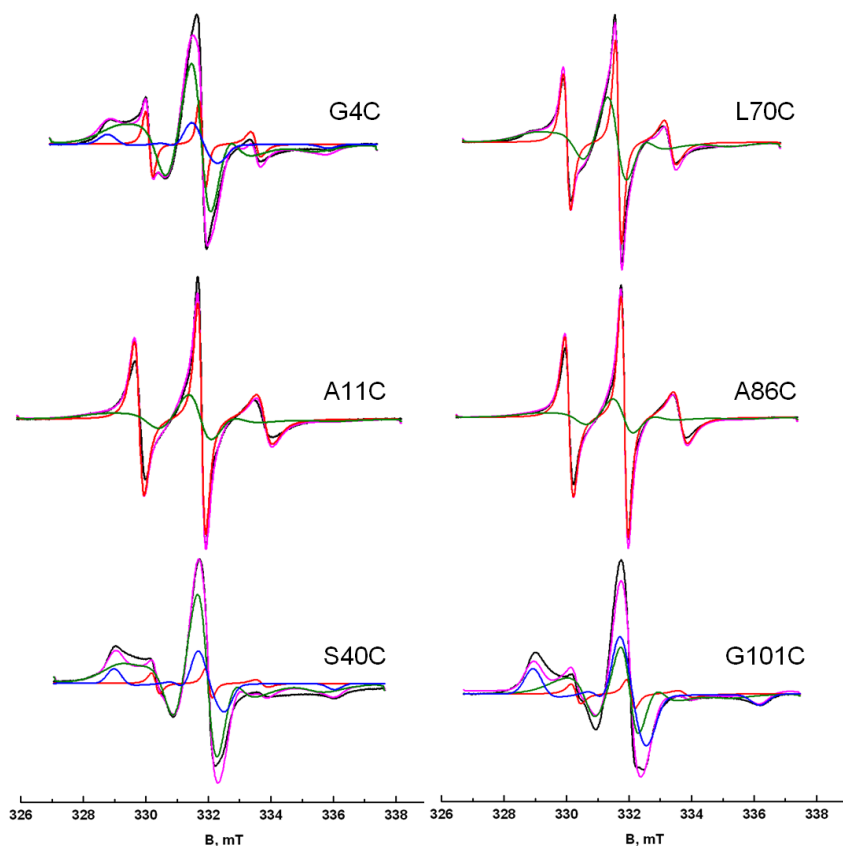


Figure 6.3 Room temperature EPR spectra of CP29 singly labeled at positions 4, 11, 40, 70, 86, and 101. The experimental spectra are shown in black. The simulated spectra are shown in magenta. The simulated spectra are adjusted to fit the intensity in the low field of the spectra to account for the asymmetry in the experimental spectra. Each simulated spectrum is a sum of multiple components. The fast, medium and slow components are shown in red, green and blue, respectively.

Table 6.1 The EPR parameters derived from the simulation of the EPR spectrum of singly labeled CP29 proteins. Given are: τ_r , rotation-correlation time, A_{zz} , hyperfine splitting along the z-direction, lw , the component line-width, and (%), the contribution of the given component to the total spectrum.

residue	fast				medium				slow			
	τ_r (ns)	A_{zz} (MHz)	lw (mT)	%	τ_r (ns)	A_{zz} (MHz)	lw (mT)	%	τ_r (ns)	A_{zz} (MHz)	lw (mT)	%
4	0.67 ± 0.01	109	0.14 ± 0.01	5	4.00 ± 0.10	109	0.32 ± 0.03	72	>50	94	0.60 ± 0.05	18
11	1.05 ± 0.01	109	0.08 ± 0.01	47	4.00 ± 0.10	109	0.32 ± 0.03	53	-	-	-	-
40	0.83 ± 0.01	109	0.14 ± 0.01	2	4.30 ± 0.10	109	0.32 ± 0.03	78	>50	94	0.60 ± 0.05	20
70	0.95 ± 0.01	109	0.08 ± 0.01	26	4.20 ± 0.10	109	0.32 ± 0.03	74	-	-	-	-
86	1.05 ± 0.01	109	0.08 ± 0.01	55	4.00 ± 0.10	109	0.32 ± 0.03	45	-	-	-	-
101	1.15 ± 0.01	109	0.14 ± 0.01	4	4.30 ± 0.10	109	0.32 ± 0.03	40	>50	94	0.60 ± 0.05	56

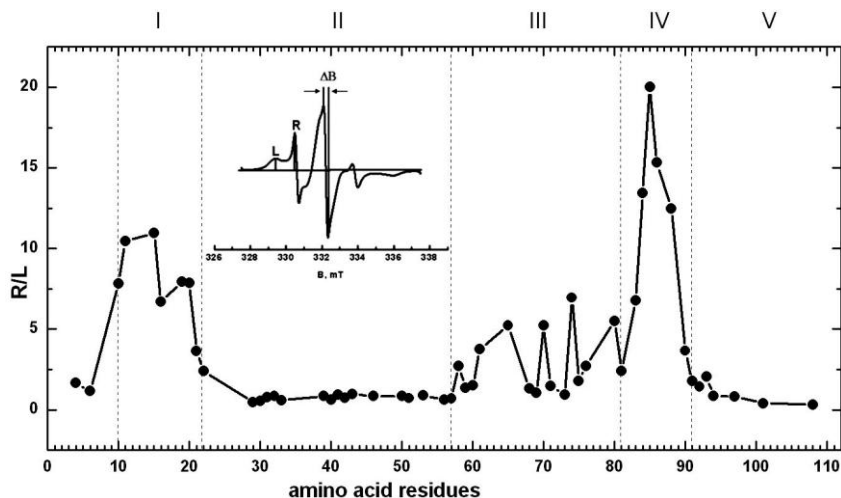


Figure 6.4 The R/L ratios versus the amino-acid residue number. The ΔB , L, and R peak indications are depicted on the inset spectrum. The line which connects the R/L values is just a guide to the eye. Five approximate regions (I-V) are defined according to the ratio of R/L, which is suggestive of different mobility regions within the N-terminus: I: residues 10 to 22, II: residues 23 to 57, III: residues 58 to 81, IV: residues 82 to 91 and V: residues 92 to 108.

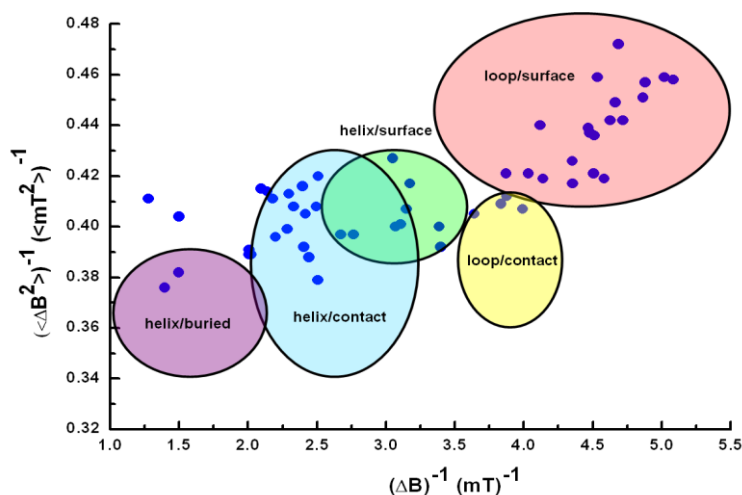


Figure 6.5 The values of the inverse second moment, $\langle \Delta B^2 \rangle^{-1}$, of the EPR lines, and of the inverse of the central line-widths, ΔB^{-1} , of the 55 singly labeled CP29 as determined from the EPR spectra (blue dots). The topological regions of a protein are indicated by ovals according to the Hubbell plot. The color-coded regions represent secondary structure in a protein: red: loop/surface site, yellow: loop/contact site, green: helix/surface site, blue: helix/contact site, and purple: helix/buried site.

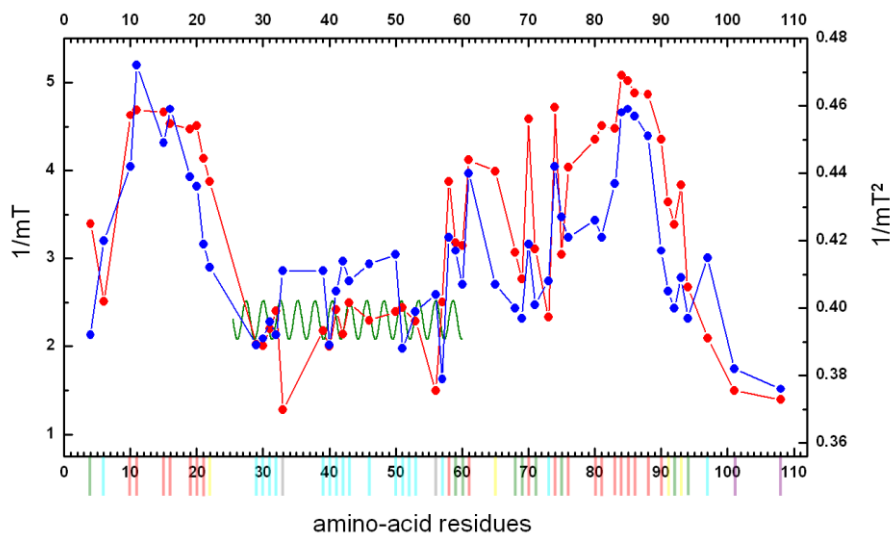


Figure 6.6 The $\langle \Delta B^2 \rangle^{-1}$ (blue dots) and the ΔB^{-1} (red dots) values versus the amino-acid residue number are given. For each amino-acid residue the color code, which is defined according to the Hubbell plot (figure 6.5) is given along the horizontal axis. The superimposed solid-green line shows the 3.6 amino-acid periodicity of an alpha-helix.

More details can be obtained from the Hubbell plot ^[20-23]. It classifies mobility in terms of the location of the residue in the protein (topographic regions), using the inverse of the central line-width (ΔB^{-1}) ^[19,20] and the inverse of the second moment ($\langle \Delta B^2 \rangle^{-1}$) ^[20-23]. For the spin-labeled variants of CP29 these values are shown as blue dots in the Hubbell plot (figure 6.5). This plot also shows the topographic regions as colored areas ^[20,29]. Most points fall within these regions. To relate these points to the sequence, figure 6.6 shows the ΔB^{-1} and $\langle \Delta B^2 \rangle^{-1}$ parameters and the region color coding as a function of the sequence number of the residue. As shown in figure 6.6, the first high-mobility region I fits with the red area in the Hubbell plot, indicating a loop/surface region. The next region with low mobility II falls into the blue area in the Hubbell plot, indicating a helix/contact region. Next is region III, which spreads over the green, red, and yellow areas, indicating a helix/surface and a loop/contact region, respectively. The next high-mobility region IV is mainly in the loop/surface region of the Hubbell plot. The last low-mobility region V coincides with the helix/buried region in the Hubbell plot, close to the transmembrane part of the protein.

We also checked for a possible periodicity in the mobility of sequential residues. While no part of the sequence exhibits a periodicity of two, indicative of a β -sheet, one stretch of residues (residues 39-46) exhibits a 3.6 periodicity (green line in figure 6.6), which suggests an α -helical stretch. The periodicity for residues 39 to 46 is most pronounced in the inverse of the central line-width. This proposed α -helical stretch is projected on an α -helical wheel diagram (figure 6.7), which reveals no clear hydrophobicity/ hydrophilicity pattern. Several residues on both sides of this helical region also fall on the green line, potentially extending the helix to residue 29 respectively 53. Clear evidence of periodicity requires data points from several successive residues and therefore, the periodicity between residues 29 to 38 and 47 to 53 cannot be confirmed. Since all residues between 29 and 53 are in the helix/contact region of the Hubbell plot, it is likely that the α -helix extends beyond the residues 39 to 46.

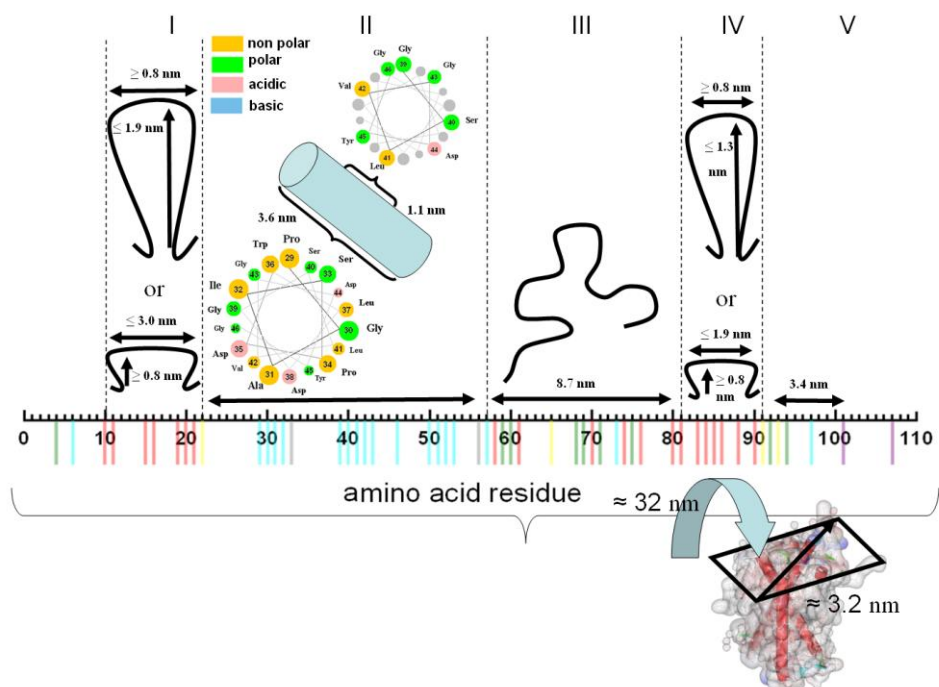


Figure 6.7 Interpretation of the mobility data obtained by EPR in the single mutants of CP29, giving geometrical constraints for the N-terminus. The residues of the N-terminus are shown horizontally, with colors from the Hubbell plot (figure 6.6). As a reference the diagonal of the stromal surface is 3.2 nm. The position of residues 101-110 should be close to the stromal surface and helix B. As an extended chain, residues 92-101 would cover a length of 3.4 nm (region V). Different models for the chain conformation result in the lengths shown for regions IV, III, and I (for details see text). Extreme loop dimensions, assuming minimum turn diameters of 8 Å and comparing long/narrow or wide/flat loops. Region II can be an α -helix. Helical-wheel diagram for region II with the corresponding amino-acid residues are depicted in colors. The color codes represent the type of amino-acid residues in the helical wheel. The numbers on each circle refer to the number of the residue within the N-terminus. Going down the helix, the size of the circles representing the residues in the helical wheel decreases. (<http://cti.itc.Virginia.EDU/~cmg/Demo/wheel/wheelApp.html>)

6.3.2 Pulsed EPR

Six different intra-molecular distances within the N-terminus of the CP29 protein are assessed using pulsed EPR measurements. The DEER time traces show clear non-exponential decays, which differ for all double mutants (figure 6.8). The absence of visible modulation indicates multiple distances or broad distance distributions. Distance distributions are obtained by the Tikhonov regularization method (see materials and methods). The distance distributions are fitted to a sum of Gaussians, the parameters of which are given in table 6.2. Most of the distance

distributions are composed of multiple Gaussians (figure 6.8), suggesting that the N-terminus adopts several conformations. For all mutants but 56/65, the distributions have at least two components with a distance larger than 2 nm (table 6.2). Components with distances below 1.8 nm are disregarded because they cannot be reliably determined under our experimental conditions ^[30]. The presence of very short distances (below 1.5 nm) can be excluded from the absence of line broadening in cw EPR spectra ^[31] of the same mutants (figure 6.9).

Table 6.2 The distance parameters for doubly labeled CP29 proteins, which are derived from the analysis of DEER data. The DEER data are analyzed by means of Tikhonov regularization. Given are: $\langle r \rangle$, distance in nm; $S(r)$, the width of the distance distribution in nm, % is the contribution of each peak and the number of spins. The width of the distance distributions reflects the unknown conformation distribution of the protein domains, which are carrying the spin labels, and the conformation distribution of the spin labels themselves. To define the number of spins, we compare the experimental time traces to the time trace of a standard sample, which contains two spins.

mutant	$\langle r_1 \rangle$ nm	$S(r_1)$ nm	%	$\langle r_2 \rangle$ nm	$S(r_2)$ nm	%	$\langle r_3 \rangle$ nm	$S(r_3)$ nm	%	$\langle r_4 \rangle$ nm	$S(r_4)$ nm	%	number of spins
4/97	—	—	—	3.19	0.84	28	4.27	0.67	20	4.94	0.98	52	1.38
4/101	1.96	1.28	35	3.53	0.68	22	5.14	0.95	43	—	—	—	1.46
4/205	1.14	1.15	44	3.14	0.84	15	3.69	0.34	2	5.06	0.76	39	1.35
56/65	1.92	1.7	95	1.67	0.6	5	—	—	—	—	—	—	1.79
56/81	2.86	1.3	54	3.72	0.9	29	5.62	0.89	17	—	—	—	2.26
56/97	1.24	1.51	49	2.95	1.62	21	3.93	0.79	11	5.6	0.9	19	2.01

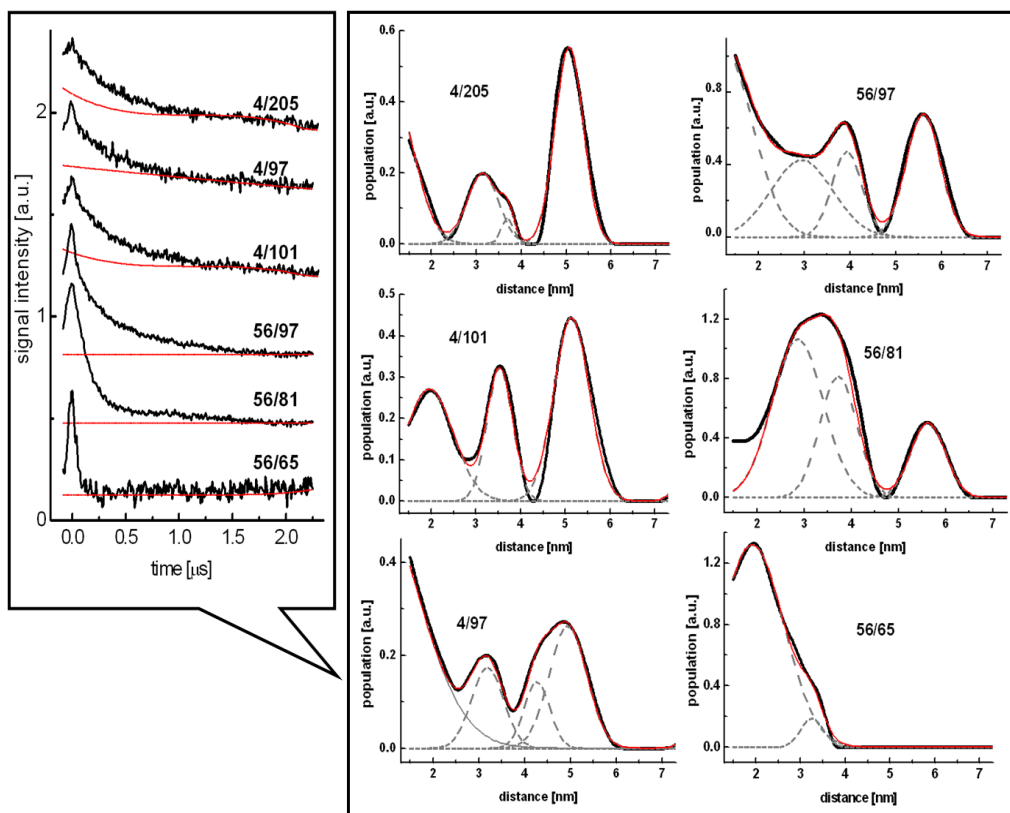


Figure 6.8 DEER data for mutants 4/97, 4/101, 4/205, 56/65, 56/97, and 56/81 are shown. Left: original DEER traces with the baseline used for correction. Right: individual distance distributions are given for each doubly labeled mutant with the corresponding Gaussian fits (performed using origin lab software). The experimental curve is shown in black and the best fit is shown in red.

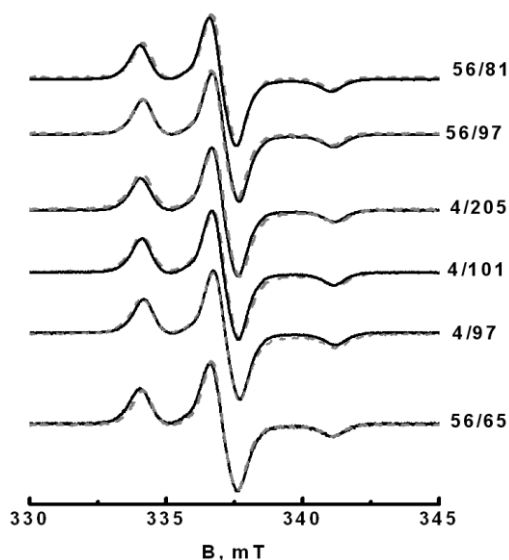


Figure 6.9 Continuous wave EPR spectra of the doubly-labeled mutants (solid lines) obtained at 80 K superimposed with the spectra of the respective singly labeled counterparts (dashed lines).

6.4 Localization of residue 4 of the N-terminus

The distances between residue 4 and residues 101 and 205, and the distance between residue 4 and the most-nearby chlorophyll as obtained from a time-resolved FRET study^[8] in the CP29 protein has been used to obtain information on the position of the end (residue 4) of the N-terminus. The crystal structure of spinach CP29^[14] served as a template in a triangulation approach described in detail in appendix B. To take into account the multiple distances obtained with DEER, all geometrically possible combinations of these distances are considered. Eliminating positions located in the protein interior, four positions remain as possible locations for residue 4 (figure 6.10.b). These positions are all close to the stromal membrane surface. Three of these positions cluster in the area where helices B and C reach the protein surface, and one is located farther from the protein surface, close to the membrane surface.

Also, a hydrophobic groove at the stromal side of the protein had been discussed as a possible location for residue 4^[8]. We note that the distances from residue 205 to selected residues in that groove (R93, Q169, K170, Y173, P174, G175, G176, D179, A184, S185, K190, and E194) are all between 0.38 and 1.71 nm. Therefore, that particular location for residue 4 would not show up in our analysis because it

would yield distances between residue 4 and 205, which are outside the distance range experimentally accessible.

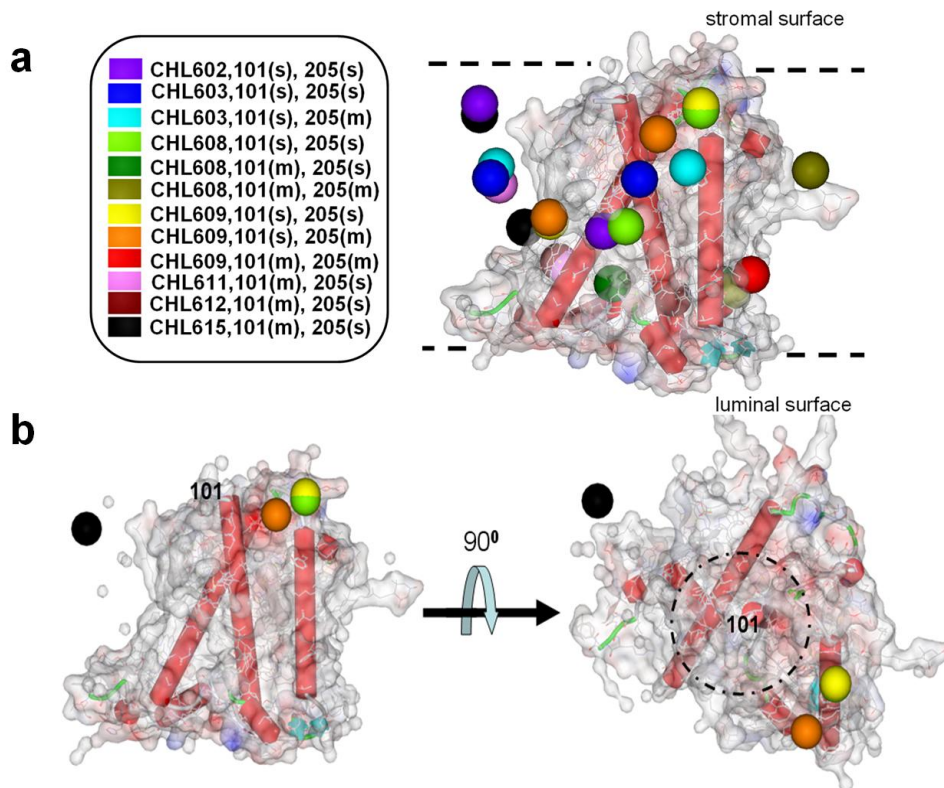


Figure 6.10 Possible locations of residue 4 shown as colored spheres, superimposed on the three-dimensional structure of the CP29 protein derived from the X-ray crystallography (orientation as in figure 6.1). a: All geometrically possible positions for residue 4. The positions are determined using distances from DEER and FRET (see text). The distance between the Mg-atom of all eight chlorophylls (see appendix B) to the C α -atoms of residue 101 (88 in *Spinach*) and residues 205 (191 in *Spinach*) are measured using the coordinates from the X-ray structure^[14]. The (s) and (m) stand for short and medium, which indicates the multiple distances obtained with DEER. Using a triangulation approach, 12 points of intersection are obtained. The intersection points are presented in different colors. For each color a three-section code is given. Each three-section code represents which chlorophyll (CHL) is used in combination with which two residues. The number given in front of CHL gives the number of the chlorophyll. b: Four positions remain possible for residue 4 after eliminating those positions that are located in the protein interior. The projection of the protein in the right hand side of the figure b is such that the yellow sphere eclipses the green sphere. The view along the membrane plane is given on the left and the view from the stromal side is given on the right. The dotted circle indicates the possible location of residue 97.

6.5 Discussion

We have investigated the N-terminus of CP29 spanning residues 1-110. This part of the protein is often considered to be flexible and only residues 101-110 are well defined in the X-ray structure^[14]. Determining the structure of such a flexible and long region of a protein is challenging. As yet the reported algorithms for prediction of loop structures were applied for loops with 4 to 20 amino-acid-residues only^[32]. Mobility of the spin label provides important markers for the structure. Here, we compare different methods of analysis of mobilities. Most rigorous is the simulation of the spectra, which reveals the multicomponent nature of the individual spectra. Absolute rotation-correlation times and the relative contribution of each component are obtained. Remarkably, spectra classified as strongly immobilized (residues 4 and 40) can have as little as 20 % of the slow component, so these spectra appear immobilized on account of a small (≤ 5 %) population of the fast component rather than a large amount of the slow component. The multicomponent nature of the spectra could indicate different conformations of the N-terminus, however, spectra with multiple components have also been reported for single-conformation proteins^[33]. Consequently, the multiple components are consistent with, but not proof for multiple conformations of the N-terminus. The interpretive value of the simulations is limited because the relation of the components and their τ_r values to the structural features of the protein is not yet understood.

The R/L method provides a qualitative measure of mobility. Comparison with the simulation shows that the spectral amplitude at the field position R derives mostly from the mobile components (the fast and the medium fraction in the simulation), whereas the amplitude at L derives from the least mobile spin labels (the slow fraction in the simulation). The R/L ratio is straightforward to determine, but because it depends on the composition of the spectrum it is difficult to apply consistently to other proteins. The analysis based on the Hubbell plot^[19,20] refers to a method for which ample reference data is available, and which enables comparison to known reference protein positions. Using the R/L method three regions of low mobility are identified: the N-terminus itself (residues 4 and 6) and the regions labeled II, and V in figure 6.4. Comparison with the Hubbell values (figure 6.6) reveals that the mobility of the spin label in region II corresponds to those found in the helix contact regions, those at III to the outer surface of proteins, and those at V to the helix/buried regions.

The distance measurements show that the N-terminus is not extended. For the nine residues from 56-65, for which the fully extended chain would have a length of 3.4 nm a length of approximately 2 nm is found. This compactness is even more evident for the mutant 56-81, which has a major contribution of a distance of 2.9

nm and a minor one of 3.7 nm, whereas the fully extended length would be 9.5 nm. The sequentially more distant pair of 56-97 has a dominant distance around 3 nm. Another indication for compactness and close association of the N-terminus is the location of residue 4. In a significant fraction of the protein this residue is close to the protein surface.

The data point to multiple conformations of the N-terminus. This follows directly from the multiple distances found in DEER experiments (table 6.2) and is consistent with multi-component cw EPR spectra (table 6.1).

Figure 6.7 shows how the mobility information relates to structural features of the 100-amino-acid-residue N-terminus. Residue 101 is located at the stromal end of helix B and its position is known from the X-ray structure. Residue 97 is 4 residues away from residue 101, the first residue defined in the X-ray structure, so residue 97 must be in a radius of maximally 1.5 nm from the entrance of helix B on the stromal side of the protein (figure 6.10). In region IV, residues have a high mobility, which is suggestive of a loop region. Assuming standard parameters for turns and interresidue separation (see materials and methods) such a loop can have two extreme shapes: as a flat loop it covers 1.9 nm in width (figure 6.7), and as a long and thin loop it extends 1.3 nm into the stroma. Region III (residues 58 to 81) has a loop/contact- helix/contact character. So it must be more strongly attached to the protein surface than region IV. In region II residues 39 to 46 have a pronounced 3.6 periodicity. Given that the entire stretch of residues in region II lies in the helix/contact region of the Hubbell plot, it may well be that this helix extends from residues 29 to 53, corresponding to a total length of the helix of 3.6 nm. Finally, region I that is flexible and shows no periodicity likely is a loop. For region I a flat loop would cover 3.0 nm almost traversing the stromal surface of the protein and as a long and thin loop it would extend 1.9 nm into the stroma, which shows that this loop is longer than the loop in region IV.

The overall architecture reveals non-covalent attachment of several N-terminal residues (at least residues 4-6), of the middle part (residues 39-46) and of the end of the N-terminus (from residue 100 onwards). Two flexible regions (I and IV) flank a less flexible region. The N-terminal part of the protein is located on the stromal side of the protein, which suggests that the less mobile regions are embedded in the stromal surface of the protein.

The first conclusion is that the N-terminus, which in its fully extended form would have a length of 38 nm, is surprisingly structured. It loops back-and-forth on the stromal surface of the protein.

Considering figure 6.10, a location of residue 97 in the vicinity of the stromal side of helix B would yield distances between residues 97 and 4 that are consistent with

the proposed locations of residue 4 derived from distances involving residues 101, 205 and FRET data. Four possible locations of residue 4 are found, out of which three (yellow, green, and orange spheres in figure 6.10.b) cluster on the region where helices B and C reach the surface of the protein. The closeness of the three positions suggests one location. The fourth position (black sphere, figure 6.10.b) suggests a second location for residue 4. A third location of residue 4 in the hydrophobic groove cannot be excluded from the data. We further speculate that the first location corresponds to the largest population of N-terminus conformations.

The presence of multiple conformations of the N-terminus, which is concluded from the present EPR investigation is in agreement with the heterogeneity reported before ^[8,9]. Two loop regions are reported, a short one, and a longer one, which are either sticking out into the stroma ^[9] or lying flat on the hydrophobic core most of the time ^[8]. According to these EPR and FRET studies ^[8,9], residue 15 is part of the short loop, and residues 65, 82, and 90 belong to the long loop. Similar to those previous reports, we find two loops. We differentiate the reported long-loop region ^[8,9] further into two mobility sections (regions III and IV), rather than one continuous mobility section. So essentially the long loop of Kavalenka et al. ^[8] and Berghuis et al. ^[9] becomes our short loop, containing both phosphorylation sites ^[34]. Compared to the previous EPR study, around residue 65 we find several residues of lower mobility (residues 57, 59, 60, 68, 69, 71, 73, and 75) arguing that residues 58 to 81 do not form part of the loop, although residue 65 has a relatively high mobility. Therefore, in addition to the report of Kavalenka et al. ^[9], where 10 residues of the N-terminus were investigated, a lot of information can be resolved by characterizing 55 residues. The structure of residues 58-97 is particularly relevant, because these residues are only present in CP29, and not in LHCII, which otherwise is similar to CP29. This may help to explain the difference in function of CP29 and LHCII in the outer membrane antenna complex.

The present study demonstrates that the N-terminus of CP29 is relatively structured and is separated into different regions with strongly differing mobilities. Moreover, there are clear signs of heterogeneity, demonstrating that the N-terminus is not fixed in one particular structure but is able to adopt various conformations. The presence of phosphorylation sites that are affected by light conditions in this region of the protein, for example at position 81 and 83 ^[34], is a strong indication that the N-terminus is important in membrane organization. The flexibility of the N-terminus found in the present study thus may be functionally important, because it enables the N-terminus to switch between different conformations in order to let the system adapt to different environmental (light) conditions.

Reference List

- [1] R.Croce, H.van Amerongen, *J.Photochem.Photobiol.B* **2011**, *104* 142-153.
- [2] G.D.Scholes, G.R.Fleming, A.Olaya-Castro, G.R.van, *Nat.Chem.* **2011**, *3* 763-774.
- [3] S.Caffarri, R.Kouril, S.Kereiche, E.J.Boekema, R.Croce, *EMBO J.* **2009**, *28* 3052-3063.
- [4] S.Caffarri, K.Broess, R.Croce, A.H.van, *Biophys.J.* **2011**, *100* 2094-2103.
- [5] T.K.Ahn, T.J.Avenson, M.Ballottari, Y.C.Cheng, K.K.Niyogi, R.Bassi, G.R.Fleming, *Science* **2008**, *320* 794-797.
- [6] N.S.Ginsberg, J.A.Davis, M.Ballottari, Y.C.Cheng, R.Bassi, G.R.Fleming, *Proc.Natl.Acad.Sci.U.S.A* **2011**, *108* 3848-3853.
- [7] S.Mauro, P.Dainese, R.Lannoye, R.Bassi, *Plant Physiology* **1997**, *115* 171-180.
- [8] B.A.Berghuis, R.B.Spruijt, R.B.M.Koehorst, A.van Hoek, S.P.Laptenok, B.van Oort, H.van Amerongen, *European Biophysics Journal with Biophysics Letters* **2010**, *39* 631-638.
- [9] A.A.Kavalenka, R.B.Spruijt, C.J.Wolfs, J.Strancar, R.Croce, M.A.Hemminga, A.H.van, *Biophys.J.* **2009**, *96* 3620-3628.
- [10] B.van Oort, S.Murali, E.Wientjes, R.B.M.Koehorst, R.B.Spruijt, A.van Hoek, R.Croce, H.van Amerongen, *Chemical Physics* **2009**, *357* 113-119.
- [11] M.Mozzo, F.Passarini, R.Bassi, A.H.van, R.Croce, *Biochim.Biophys.Acta* **2008**, *1777* 1263-1267.
- [12] Y.E.Chen, Z.Y.Zhao, H.Y.Zhang, X.Y.Zeng, S.Yuan, *J.Exp.Bot.* **2013**.
- [13] R.Croce, J.Breton, R.Bassi, *Biochemistry* **1996**, *35* 11142-11148.
- [14] X.Pan, M.Li, T.Wan, L.Wang, C.Jia, Z.Hou, X.Zhao, J.Zhang, W.Chang, *Nat.Struct.Mol.Biol.* **2011**, *18* 309-315.
- [15] S.Jansson, *Trends Plant Sci.* **1999**, *4* 236-240.
- [16] S.Stoll, A.Schweiger, *Journal of Magnetic Resonance* **2006**, *178* 42-55.
- [17] I.Sepkhanova, M.Drescher, N.J.Meeuwenoord, R.W.A.L.Limpens, R.I.Koning, D.V.Filippov, M.Huber, *Applied Magnetic Resonance* **2009**, *36* 209-222.
- [18] Q.F.Ma, J.Hu, W.H.Wu, H.D.Liu, J.T.Du, Y.Fu, Y.W.Wu, P.Lei, Y.F.Zhao, Y.M.Li, *Biopolymers* **2006**, *83* 20-31.
- [19] M.N.Oda, T.M.Forte, R.O.Ryan, J.C.Voss, *Nat.Struct.Biol.* **2003**, *10* 455-460.
- [20] W.L.Hubbell, H.S.Mchaourab, C.Altenbach, M.A.Lietzow, *Structure* **1996**, *4* 779-783.
- [21] W.L.Hubbell, C.Altenbach, *Current Opinion in Structural Biology* **1994**, *4* 566-573.
- [22] H.S.Mchaourab, M.A.Lietzow, K.Hideg, W.L.Hubbell, *Biochemistry* **1996**, *35* 7692-7704.
- [23] H.S.Mchaourab, T.Kalai, K.Hideg, W.L.Hubbell, *Biochemistry* **1999**, *38* 2947-2955.
- [24] L.Columbus, W.L.Hubbell, *Trends in Biochemical Sciences* **2002**, *27* 288-295.
- [25] W.G.Miller, C.V.Goebel, *Biochemistry* **1968**, *7* 3925-&.
- [26] M.Drescher, G.Veldhuis, B.D.van Rooijen, S.Milikisyants, V.Subramaniam, M.Huber, *J.Am.Chem.Soc.* **2008**, *130* 7796-7797.
- [27] G.Jeschke, *Chemphyschem* **2002**, *3* 927-932.
- [28] G.Jeschke, V.Chechik, P.Ionita, A.Godt, H.Zimmermann, J.Banham, C.R.Timmel, D.Hilger, H.Jung, *Applied Magnetic Resonance* **2006**, *30* 473-498.
- [29] J.M.Isas, R.Langen, H.T.Haigler, W.L.Hubbell, *Biochemistry* **2002**, *41* 1464-1473.
- [30] G.Jeschke, Y.Polyhach, *Phys.Chem.Chem.Phys.* **2007**, *9* 1895-1910.
- [31] M.Robotta, P.Braun, R.B.van, V.Subramaniam, M.Huber, M.Drescher, *Chemphyschem* **2011**, *12* 267-269.
- [32] R.Subramaniam, T.Koppal, M.Green, S.Yatin, B.Jordan, J.Drake, D.A.Butterfield, *Neurochemical Research* **1998**, *23* 1403-1410.
- [33] H.J.Steinhoff, *Frontiers in Bioscience* **2002**, *7* C97-C110.
- [34] R.Fristedt, A.V.Vener, *PLoS One* **2011**, *6* e24565.

CHAPTER 7

STRUCTURE AND FIRST EPR CHARACTERIZATION OF HELICAL PEPTIDES WITH TOAC SPIN LABELS: MODELS FOR SHORT DISTANCES

For structure determination in biophysical systems electron paramagnetic resonance (EPR) is rapidly gaining ground. Proteins labeled specifically with two nitroxide spin labels can be prepared, and several EPR methods are available for distance determination, which makes it possible to determine distance constraints. However, such methods require frozen solutions, potentially causing non-physiological states of the sample. Here we target spin-spin interaction in liquid solution at room temperature using rigid model compounds. A series of helical peptides is synthesized with pairs of spin labels separated by three, four, and five amino acids. To avoid flexibility, the non-coded nitroxyl containing α -amino acid TOAC that is rigidly connected with the peptide backbone is used. The EPR spectra of the peptides show a decreasing amount of coupling between the two spin labels within this series, which provides a first characterization of these models.

Maryam Hashemi Shabestari, Martin van Son, Alessandro Moretto, Marco Crisma, Claudio Toniolo, Martina Huber.

7.1 Introduction

Biological systems are preferably studied in liquid solution at room temperature because freezing a peptide or a protein can change or even destroy the three-dimensional structure of interest. Most EPR methods for distance determination require freezing the sample ^[1-6]. To address this problem, in the present work we investigate spin-spin interactions in model peptide systems in liquid solution. Such peptides have to be rigid to serve as useful model compounds. More specifically, we analyze a series of peptides consisting of stretches of the non-coded, host α -amino acid α -aminoisobutyric acid (Aib), combined with one or two 4-amino-1-oxy-2,2,6,6-tetramethylpiperidine-4-carboxylic acid (TOAC) guest residues. Both TOAC ^[7-13] and Aib ^[14-16] are known to stabilize regular 3_{10} -helices ^[14,16-19]. The backbone and side-chain conformations of TOAC are remarkably constrained, providing well-defined distances between the stable nitroxide free radicals of two TOAC residues. Flexibility, as resulting from the commonly used spin labels linked to the cysteine side chain in proteins, is thus avoided. Our series comprises a full set of peptides, from two to five intervening Aib residues, with incrementally increased TOAC...TOAC separations. The following compounds were investigated:

(i)	Z-(Aib) ₉ -OMe	NONA	unlabeled
(ii)	Z-(Aib) ₅ -TOAC-Aib-OMe	HEPTA ₆	monoradical
(iii)	Z-(Aib) ₆ -TOAC-Aib-OMe	OCTA ₇	monoradical
(iv)	Fmoc-Aib-TOAC-(Aib) ₇ -OMe	NONA ₂	monoradical
(v)	Fmoc-(Aib) ₂ -TOAC-(Aib) ₂ -TOAC-Aib-OMe	HEPTA _{3,6}	biradical
(vi)	Fmoc-TOAC-(Aib) ₃ -TOAC-Aib-OMe	HEXA _{1,5}	biradical
(vii)	Fmoc-Aib-TOAC-(Aib) ₄ -TOAC-Aib-OMe	OCTA _{2,7}	biradical
(viii)	Fmoc-Aib-TOAC-(Aib) ₅ -TOAC-Aib-OMe	NONA _{2,8}	biradical

Here Z is benzyloxycarbonyl, OMe is methoxy, and Fmoc is fluorenyl-9-methyloxycarbonyl. We address the sub-nanometer distances between two TOAC residues in the biradical peptides and compare them with a set of monoradical peptides that are matched in size. We determine the exchange interaction, *J*, in liquid solution using continuous-wave (cw) EPR. For selected peptides also the dipolar interaction in frozen solution was studied.

In the sub-nanometer distance regime in liquid solution, the spin-spin interaction should manifest itself primarily as the exchange interaction, *J*. In the weak-exchange limit, the spectra appear as those of the isolated radicals. For nitroxides

characteristic three-line spectra result, which come from the isotropic hyperfine interaction A_N of the electron spin with the ^{14}N , $I = 1$ nucleus. A strong-exchange interaction ($J \gg A_N$) results in a five-line spectrum. The magnitude of J is related to the orbital overlap, and often J is believed to decay exponentially with distance ^[20]. Orbital overlap through the bonds, which are linking the centers of spin density can also promote exchange interaction.

For selected peptides the dipolar interaction was studied in frozen solution with X-band (9.5 GHz) and W-band (95 GHz) EPR. At W-band, the spectral resolution increases and the information on magnetic parameters and molecular orientations, which is hidden under the broad lines in spectra that are obtained at X-band can be extracted. Furthermore, the higher resolution at W-band enables the detection of smaller dipolar interactions, i.e., longer distances than in X-band. Also, relative orientations of spin labels are accessible ^[21].

The rigid biradical peptides investigated enable a systematic study of the exchange interaction. Overall, a decrease of J with increasing separation of the two TOAC residues is observed. We speculate that J is dominated by through-bond rather than through-space interaction. Careful line-shape analysis gives insight into the intra-radical interactions.

7.2 Materials and methods

7.2.1 Synthesis and characterization of peptides

Peptides NONA ^[7], NONA₂ (labeled as NONA₉ in ^[7]) NONA_{2,8} ^[7], and HEPTA_{3,6} ^[22], have already been described. The difficult syntheses of the other very highly constrained TOAC/Aib peptides mentioned in this paper have been performed in solution ^[23] either: step-by-step by using the 1-(3-dimethylamino)propyl-3-ethylcarbodiimide/7-aza-1-hydroxy-1,2,3-benzotriazole method ^[24] (HEXA₅, HEXA_{1,5}, and OCTA_{2,7}) or by the segment condensation procedure using the isolated and uncharacterized intermediate 5(4*H*)-oxazolones from Z-(Aib)₃-OH ^[25] and Z-(Aib)₅-OH ^[25] for HEPTA₆ and OCTA₇, respectively. The chromatographically pure peptides show the following physical and analytical data: (a) HEPTA₆: melting point 219-221° C (from EtOAc – PE); infrared (IR) (KBr) 3322, 1712, 1664 cm⁻¹. (b) OCTA₇: melting point 222-224° C (from EtOAc – PE); IR (KBr) 3318, 1712, 1662 cm⁻¹. (c) HEXA_{1,5}: melting point 146-147° C (from EtOAc – PE); IR (KBr) 3331, 1669 cm⁻¹. (d) OCTA_{2,7}: melting point 160-162°C (from EtOAc – PE); IR (KBr) 3306, 1659 cm⁻¹.

7.2.2 Fourier transform infrared absorption spectroscopy

Fourier transform infra red absorption spectra were recorded using a Perkin-Elmer 1720 X FT-IR spectrophotometer, nitrogen-flushed, with a sample shuttle device and at 2 cm^{-1} nominal resolution, averaging 100 scans. Solvent (baseline) spectra were recorded under the same conditions. Cells with CaF_2 windows and path lengths of 0.1 and 1.0 mm were used. Spectrograde deuteriochloroform (99.8 % deuterated) was obtained from Fluka.

7.2.3 EPR spectroscopy

The X-band cw EPR measurements were performed both at room temperature (293 K) and at 80 K using an Elexsys 680 (Bruker BioSpin GmbH, Rheinstetten, Germany) spectrometer equipped with a rectangular cavity. For the room temperature measurements microwave power, modulation frequency, and modulation amplitude were 0.3994 mW, 100 kHz, and 30 μT , respectively, and accumulation time was about 20 minutes per spectrum. In the frozen solution at X-band microwave power, modulation frequency, and modulation amplitude were 0.159 mW, 100 kHz, and 0.2 mT, respectively.

For room temperature W-band measurements, a modulation frequency of 100 kHz and a modulation amplitude of 0.1 mT were applied. The standard 95 MHz sample clamp was used with the usual sample holder to place the sample properly in the resonator. For the frozen solution W-band measurements, microwave power, modulation frequency, and modulation amplitude were $5.0 \cdot 10^{-5}$ mW, 100 kHz, and 0.5 mT, respectively.

7.2.4 Preparation of the samples

All peptides were dissolved in acetonitrile (Biotech. grade, $\geq 99.93\%$, Sigma-Aldrich). For room temperature X-band measurements, all the peptide samples were degassed and prepared in quartz tubes with an outer diameter of 4 mm and an inner diameter of 1.5 mm. The samples were then subjected to seven freeze-pump-thaw cycles. To freeze the sample, liquid nitrogen was used. The sample was thawed to room temperature. While the samples were frozen, the quartz tubes were connected to a rotary vacuum pump for 5 minutes and disconnected from the pump before thawing the sample. Finally the degassed samples were flame-sealed. The room temperature W-band samples were prepared in suprasil quartz capillaries, with an inner diameter of 0.125 mm and an outer diameter of 0.25 mm, from Wilmad-Lab glass (Buena, NJ, USA). The capillaries were sealed at one end. A Wilmad suprasil quartz tube with an inner diameter of 0.60 mm and an outer diameter of 0.84 mm,

which was sealed at one end, was used as an outside tube. The concentration of the TOAC spin label in all liquid solution samples was 0.1 mM.

For the measurements in frozen solution at X-band, samples were prepared in quartz tubes with an outer diameter of 4 mm and were frozen in liquid nitrogen before inserting them in the pre-cooled helium gas-flow cryostat. For 80 K W-band measurements, the samples were measured in Wilmad suprasil quartz tubes with an inner diameter of 0.60 mm and an outer diameter of 0.84 mm that were sealed at one end. Both the monoradical, NONA₂, and the biradical, NONA_{2,8}, samples were diluted with NONA, the Aib peptide at a 1 to 10 diamagnetically dilution. The concentration of NONA₂ and NONA_{2,8} in frozen solution was 0.2 mM and 0.1 mM, respectively.

7.2.5 Simulation

The spectra were simulated using Matlab and the EasySpin package ^[26]. For the simulation the following parameters were used: $g = [2.009, 2.006, 2.003]$ ^[7], $A_{xx} = A_{yy} = 0.553$, and $A_{zz} = 3.375$ mT. The three-line spectra were simulated using a Gaussian line-shape. The five-line spectra were simulated using an equal-amount contribution of a Gaussian and a Lorentzian line-shape ^[26].

For the biradical peptides, the treatment of the effect of J depends on the type of spectrum. For compounds with a three-line spectrum, the spectra were simulated with the chili subroutine of EasySpin as an $S = 1/2$ system. For the five-line spectra, the effect of the exchange interaction was included explicitly in the simulation using the pepper subroutine as two coupled $S = 1/2$ systems. The presence of a sharp three-line component in the five-line spectrum was taken into account in the simulation by adding a mono-radical contribution to each spectrum using the chili subroutine. We checked the presence of satellite lines for HEXA_{1,5} and OCTA_{2,7} by measuring at higher powers, larger sweep widths and higher concentrations (about 5 mM, non degassed). We also increased the modulation amplitude. However, no satellite lines were detected.

7.3 Results

7.3.1 Conformational analysis

We carried out a conformational analysis of all TOAC-labeled (Aib)_n host peptides (from hexamers to nonamers) studied in this work in CDCl₃, a secondary-structure supporting solvent. Since neither circular dichroism (because all peptides are achiral) nor nuclear magnetic resonance (because all peptides contain at least one stable paramagnetic free radical) are appropriate spectroscopies with these compounds, we relied heavily on FT-IR absorption. The N-H stretching (amide A)

spectral region proved to be the most conformationally informative. Here, all peptides are characterized by two bands: a much weaker one, seen at 3435-3418 cm^{-1} (free, solvated NH groups) and a much more intense one at 3339-3318 cm^{-1} (H-bonded NH groups) ^[15,27,28]. With increasing main-chain length, the stronger band moves to lower wave numbers and increases in intensity ^[15]. The role of peptide concentration, at least below 5×10^{-3} M, is of minor significance, which indicates that the observed C=O...H-N H-bonds are mostly intra-molecular. The ratios of the integrated molar extinction coefficients of the H-bonded versus free NH groups point clearly to almost fully developed 3_{10} -helical ^[14,16-19] peptide structures ^[15]. These findings are not unexpected on the basis of literature data of medium-sized peptides rich in the known helicogenic TOAC ^[8,13] and Aib ^[14-16] residues in CDCl_3 solution and in the crystal state.

7.3.2 Room temperature cw EPR

Figure 7.1 presents the room temperature spectra of the monoradical and the biradical peptides. The spectra of the monoradical peptides consist of three narrow lines. The spectra of the biradical peptides can be grouped into two distinct classes: the HEPTA_{3,6} and the HEXA_{1,5} peptides with a five-line spectrum and the OCTA_{2,7} and the NONA_{2,8} peptides with a three-line spectrum. The five-line spectra have broader lines than those of the monoradical peptides and a contribution of a narrow-line spectrum consisting of three lines marked in figure 7.1.

The two classes of spectra are simulated by different approaches. For the two biradical peptides that have a five-line spectrum, the contribution of exchange interaction is larger than the hyperfine coupling of the ^{14}N nucleus in the TOAC spin label (table 7.1), and we consider the contribution of J explicitly in the simulation. For the HEPTA_{3,6} peptide, the value of J is larger than 900 MHz. For HEXA_{1,5}, the next biradical peptide in the series, the value of J is 800 MHz. For the three-line-spectra of the OCTA_{2,7} and NONA_{2,8} peptides, the value of J must be smaller than 9 MHz because for values of J above 9 MHz a significant deviation of the simulation from the observed three-line spectra occurs, a deviation that is not visible in the experimental spectra. Given that small value of J , we do not explicitly consider J in the simulation.

To exactly match the line-shape of the simulated to the experimental spectra for all biradical peptides, additional parameters are needed (figure 7.2 and table 7.1). The spectra of the HEXA_{1,5} and the HEPTA_{3,6} peptides are simulated by two components, one component with a large J -value, representing the biradical, and the other representing a monoradical component. The monoradical contribution is simulated with the parameters of the respective monoradical peptide (table 7.1). The

spectra of the second class of peptides, the OCTA_{2,7} and the NONA_{2,8} peptides are fully described by a single component. The NONA_{2,8} peptide is simulated with an isotropic rotation correlation time, similar to the value we used to simulate the corresponding monoradical, NONA₂. The simulated spectrum of the OCTA_{2,7} peptide does not fit as well to the isotropic rotation model as the NONA_{2,8} peptide. The deviation of the simulated low-field line from the experimental one derives either from an anisotropic rotation or from a contribution of J in the order of 9 MHz. The spectrum of the OCTA_{2,7} peptide can be fitted with an anisotropic-rotation model using the best-fit option in the EasySpin program (table 7.1). However, we cannot exclude J-coupling, as it would produce qualitatively similar features. For the NONA₂ and the NONA_{2,8} peptides, EPR spectra are also acquired at W-band. The spectra of NONA₂ and NONA_{2,8} are identical (figure 7.3), which reveals that for these peptides the EPR spectra at W-band frequencies are dominated by motion, rather than by the spin-spin interaction.

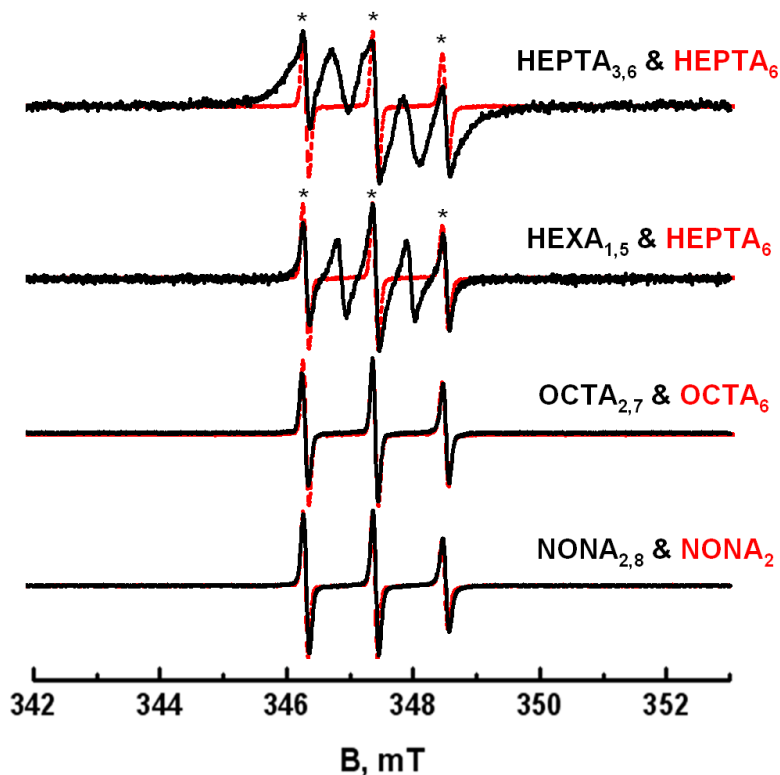


Figure 7.1 The room temperature X-band EPR spectra of monoradical (red) and biradical (black) peptides. Comparison of mono- with biradical peptides are shown from top to bottom: HEPTA_{3,6} with monoradical HEPTA₆; HEXA_{1,5} with monoradical HEPTA₆; OCTA_{2,7} with monoradical OCTA₇, and NONA_{2,8} with monoradical NONA₂. The black asterisks indicate the presence of narrow lines on top of the broad lines in the spectrum of the biradical peptides.

Table 7.1 Parameters used for the simulation of the liquid solution X-band EPR spectra of the monoradical and biradical peptides. Given on the right are parameters for monoradicals: rotation correlation times τ_r and line-widths. On the left are simulation parameters for biradicals (τ_r , line-widths, and the line-shape: mixture of Gaussian and Lorentzian). The simulation parameters and the relative contribution of monoradical species to these spectra is given on the right. For HEPTA_{3,6} and HEXA_{1,5} the exchange interaction is explicitly considered. For details see text.

peptides			τ_r (ns)	line-width ^a (mT)				
HEPTA ₆			0.13	0.130				
OCTA ₇			0.15	0.130				
NONA ₂			0.17	0.130				
peptides	parameters used for the simulation of biradical peptides					monoradical contribution to biradical spectra		
	Relative position of the 2 nd TOAC in the helix	J-coupling (MHz)	τ_r (ns)	line-width (mT)		τ_r (ns)	line-width ^a (mT)	monoradical component in biradical spectra %
				Gaussian	Lorentzian			
HEPTA _{3,6}	4	> 900	n.a. ^b	0.450	0.480	0.13	0.130	3
HEXA _{1,5}	5	800	n.a.	0.000	0.290	0.13	0.130	23
OCTA _{2,7}	6	< 9	0.15 ^c	0.098	0.037	n.a.	n.a.	n.a.
NONA _{2,8}	7	< 9	0.17	0.110	0.037	n.a.	n.a.	n.a.

^a Gaussian single-component line

^b not applicable

^c The EPR simulation parameters for the OCTA_{2,7} peptide using an anisotropic rotation with axial rotation tensor; Best-fit parameters: $\tau_{\parallel} = 0.016$, $\tau_{\perp} = 0.78$, $\tau_{iso} = 0.046$

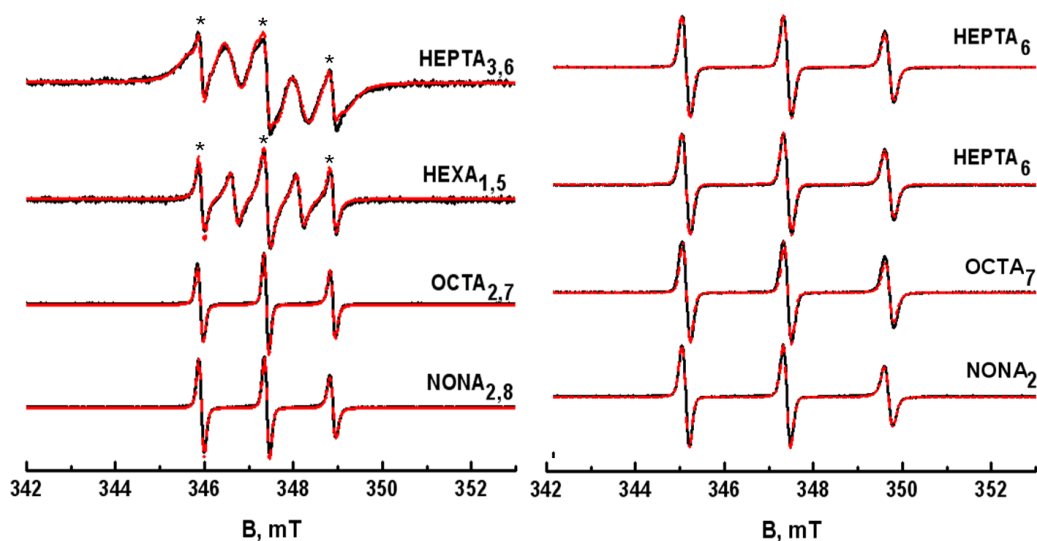
$\tau \parallel$ 

Figure 7.2 The room temperature X-band EPR spectra of monoradical and biradical peptides compared with the simulation. Simulated spectra are shown in red and the experimental ones are shown in black. On the left, the spectra of HEPTA_{3,6}, HEXA_{1,5}, OCTA_{2,7}, and NONA_{2,8} are shown. On the right, the spectra of HEPTA₆, OCTA₇, and NONA₂ are shown. The black asterisks indicate the presence of narrow lines (monoradical contribution) on top of the broad lines in the spectrum of the biradical peptides.

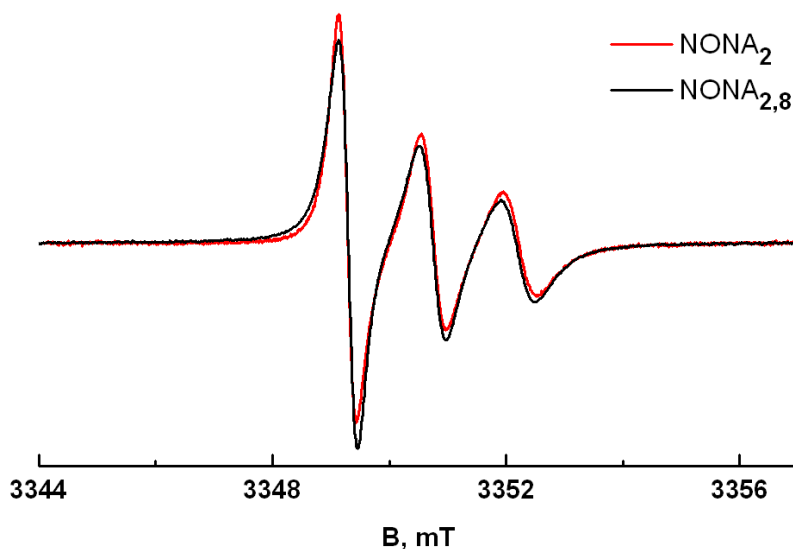


Figure 7.3 The room temperature W-band EPR spectra of the NONA₂ peptide (red) and the NONA_{2,8} peptide (black). The spectra of NONA₂ and NONA_{2,8} are similar. The spectra are normalized to the number of spins in each sample.

7.3.3 NONA₂ and NONA_{2,8} at X-band, in frozen solution

In frozen solution, in addition to the exchange interaction, the dipolar interaction can be determined. However, the peptides seem to aggregate in frozen solution, as evidenced by the line broadening of NONA₂ relative to a reference sample containing the MTS spin label, which is prepared in the same solvent and measured under the same conditions (figure 7.4).

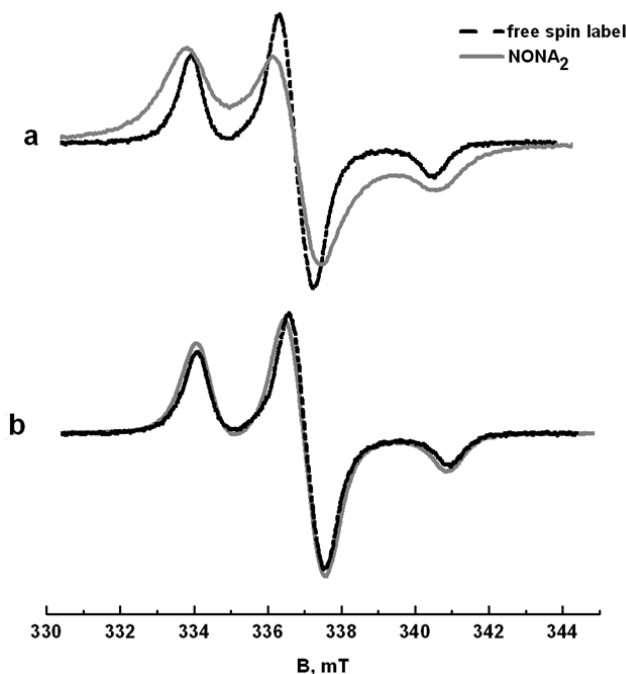


Figure 7.4 Frozen solution X-band EPR spectra of the NONA₂ peptide and the free MTS spin label in the same solvent. a: Pure NONA₂ peptide (grey line) and free MTS spin label (black line). b: Diamagnetically diluted (1:10) NONA₂ peptide (grey line) and free MTS spin label (black line). In a the lines of the NONA₂ peptide are broader compared to the lines in b, owing to the intermolecular spin-spin interaction. The spectra are normalized to the number of spins in each sample.

To suppress intermolecular spin-spin interaction, diamagnetic dilution with the Aib-only peptide NONA is applied^[29]. We investigated 1:5 and 1:10 ratios of NONA₂ to NONA. At both ratios the spectra have the same line-width as the reference sample has. Therefore, the biradical NONA_{2,8} was investigated at a 1 to 10 diamagnetic dilution. For NONA_{2,8} compared with NONA₂, the lines are broader, which results from the dipolar interaction in the NONA_{2,8} peptide (figure 7.5).

Distances derived from the second-moment analysis ^[30] of the NONA₂ and the NONA_{2,8} spectra result in a distance of 1.1 nm, which is in good agreement with the distance of 1.2 nm reported from the X-ray structure ^[7].

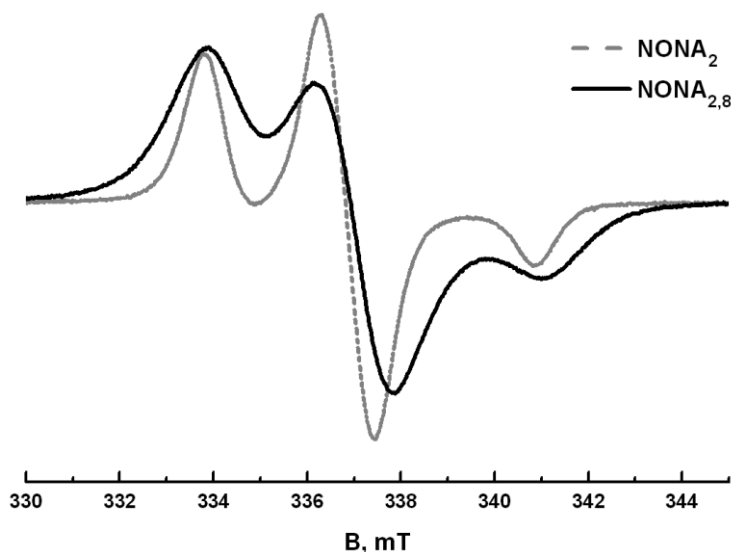


Figure 7.5 Frozen solution X-band EPR spectra of the NONA₂ peptide (grey line) and the NONA_{2,8} peptide (black line). Both peptides are diamagnetically diluted (1:10). The lines of the NONA₂ peptide are narrower compared to those of the NONA_{2,8} peptide. The spectra are normalized to the number of spins in each sample.

7.3.4 NONA₂ and NONA_{2,8} at W-band, in frozen solution

The EPR spectra of both NONA₂ and NONA_{2,8} at W-band (figure 7.6) are acquired from the same diamagnetically diluted samples as used for X-band in frozen solution (1 to 10).

At W-band, the g-tensor resolution increases, making it possible to resolve the rhombic g-tensor, while at X-band the nitroxide spectrum is dominated by the hyperfine interaction with the nitrogen nucleus. Similar to the result at X-band, the lines of NONA_{2,8} are broadened with respect to NONA₂. The higher resolution at W-band was used by Carlotto et al. ^[33] to determine the distance and relative orientation of the TOAC radicals in NONA_{2,8}.

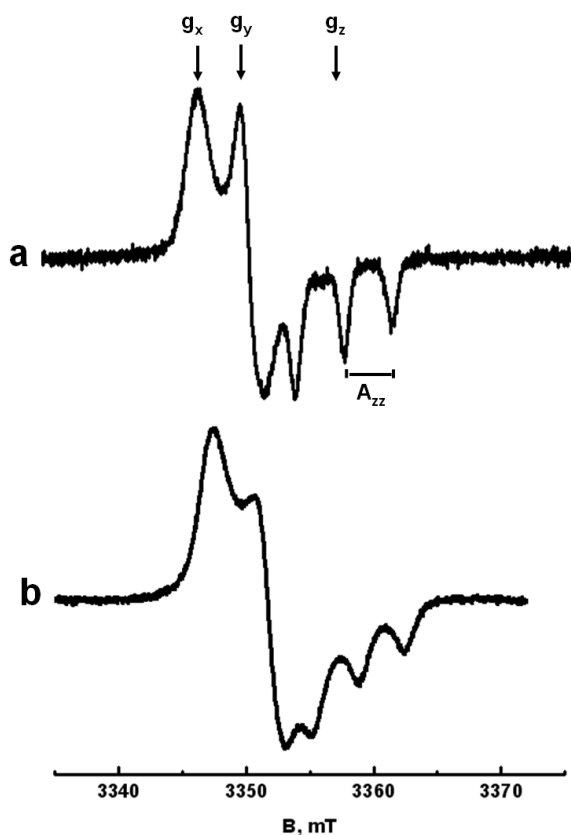


Figure 7.6 Frozen solution W-band EPR spectra of a: the NONA₂ peptide and b: the NONA_{2.8} peptide. The position of the spectral features at g_x , g_y , g_z , and the hyperfine splitting A_{zz} are indicated.

7.4 Discussion

We have investigated a set of biradical peptides built from the non-natural amino-acid Aib, both in liquid and in frozen solution. In liquid solution at room temperature, the peptides have spectra that are in the motionally narrowed regime. The spectra of the biradicals are determined primarily by the exchange interaction [32]. In the strong-exchange regime, where $J \gg A_N$, the EPR spectrum is characterized by a five-line pattern with intensities 1:2:3:2:1, while in the weak-exchange regime the EPR spectrum has three lines of equal intensity. The spectra of biradicals HEPTA_{3,6} and HEXA_{1,5} are in the strong-exchange regime. The difference in the line-shapes between HEPTA_{3,6} and HEXA_{1,5} suggests a larger J for HEPTA_{3,6} or an additional dynamic process. The biradicals OCTA_{2,7} and NONA_{2,8} are in the weak-exchange limit. Because the effect of J on the spectrum is minimal and because no

simulation program combines J-interaction with restricted mobility we have simulated the spectra of the OCTA_{2,7} and the NONA_{2,8} peptides as two independent spins. Therefore, only upper limits of J can be determined. The spectrum of OCTA_{2,7} shows deviations from the isotropic-motion regime. Whether this deviation reflects anisotropic motion or a J-value that is slightly larger than 9 MHz is not clear yet. The main result is that the J-coupling decreases with increasing residue separation in the sequence.

7.4.1 Origin of the narrow-line contribution

The presence of a sharp narrow-line component is prominent in the five-line-spectrum of the HEPTA_{3,6} and HEXA_{1,5} peptides. There are two possibilities for the origin of this component. First, the sharp component may arise from a minimally populated conformation of the peptides, which leads to increased separation between the labels such that we have a contribution of a low J-value in addition to the dominant high J-value conformation of the peptide. A second possibility is that in a fraction of the peptides one of the nitroxides is chemically degraded. The rigidity of the peptides investigated argues against the presence of minority conformations in which J is small. Therefore we attribute the narrow-line component to a monoradical contamination.

7.4.2 The relation between structure and J-coupling

The strength of the exchange interaction is often considered to decay exponentially with distance and has been used to obtain a qualitative ranking of the distance of spin-label positions ^[32]. For the set of peptides that are investigated here, the separation between the TOAC residues increases by one residue each in the series. The distance between the nitroxide groups, i.e., the through-space distance does not increase through the series (table 7.2). For example, the distance between residues one and five (in HEXA_{1,5}) is similar to the distance between two and eight (in NONA_{2,8}). So if J would scale with the distance between the nitroxide groups through space, the HEXA_{1,5} and NONA_{2,8} peptides should have similar values of J. However, the NONA_{2,8} peptide has a very small J, while the HEXA_{1,5} has a much larger J, a clear indication that the through-space distance of the nitroxides does not dominate J. The number of bonds between the nitroxides does increase monotonically within the series from HEXA_{1,5} to NONA_{2,8}. Particularly, the number of bonds between the nitroxides in HEXA_{1,5} is smaller than those in the NONA_{2,8} peptide, nicely following the trend in J. The difference between these two peptides shows that the through-bond contribution to J plays a major role.

Table 7.2 Comparison of the biradical peptides investigated. The number of covalent bonds between the two TOAC spin labels in each biradical peptide and the distance between the mid-points of the N-O bonds of the two TOAC labels in the 3_{10} -helix are given.

peptide	position of the two TOAC labels	distance between the two TOAC residues (Å)	number of covalent bonds	J-coupling (MHz)
HEPTA _{3,6}	i, i + 3	6.5 ^a	15	> 900
HEXA _{1,5}	i, i + 4	11.6 ^b	18	800
OCTA _{2,7}	i, i + 5	14.6 ^b	21	< 9
NONA _{2,8}	i, i + 6	12.6 ^c	24	< 9

^a Experimentally determined i, i + 3 distance from the X-ray diffraction structure of HEPTA_{3,6}^[33].

^b Calculated from a 3_{10} -helical peptide model.

^c Experimentally determined i, i + 6 distance from the X-ray diffraction structure of OCTA_{1,4,7}^[34].

7.4.3 The contribution of dipolar interaction

In the spectra in liquid solution no dipolar interaction is observed, although this interaction is expected to be large in view of the distance between the TOAC residues. The absence of dipolar broadening in the spectra proves that the rotation of the peptides is fast enough to average the dipolar interaction.

In frozen solution, both the exchange and dipolar interactions are detectable. However, in frozen solution these peptides tend to aggregate and intermolecular interactions interfere with the intra-molecular interactions. To avoid this interference, we applied diamagnetic dilution. Comparison of the diluted monoradical vs. biradical peptides provides us with intra-molecular information, i.e., the spin-spin distance in a biradical peptide. The value of 1.1 nm obtained from the line-shape analysis agrees with the results from X-ray crystallography^[7].

7.4.4 Summary and conclusions

The series of biradical peptides enabled a systematic study of the exchange interaction. We demonstrate that in these helical peptides the through-bond contribution dominates over the through-space contribution, which gives rise to a substantial J even over a separation of 12 Å. We are pursuing these studies with the quantum-chemical approach applied in reference^[7], which will give insight into the electronic structure of these peptides.

Reference List

- [1] W. L. Hubbell, C. Altenbach, *Current Opinion in Structural Biology* **1994**, 4 566-573.
- [2] Q. Cai, A. K. Kusnetzow, W. L. Hubbell, I. S. Haworth, G. P. Gacho, E. N. Van, K. Hideg, E. J. Chambers, P. Z. Qin, *Nucleic Acids Res.* **2006**, 34 4722-4730.
- [3] G. Jeschke, *Chemphyschem* **2002**, 3 927-932.
- [4] G. Jeschke, A. Bender, H. Paulsen, H. Zimmermann, A. Godt, *J.Magn Reson.* **2004**, 169 1-12.
- [5] G. Jeschke, H. Zimmermann, A. Godt, *J.Magn Reson.* **2006**, 180 137-146.
- [6] G. Jeschke, Y. Polyhach, *Phys.Chem.Chem.Phys.* **2007**, 9 1895-1910.
- [7] S. Carlotto, M. Zerbetto, M. H. Shabestari, A. Moretto, F. Formaggio, M. Crisma, C. Toniolo, M. Huber, A. Polimeno, *J.Phys.Chem.B* **2011**, 115 13026-13036.
- [8] M. Crisma, J. R. Deschamps, C. George, J. L. Flippen-Anderson, B. Kaptein, Q. B. Broxterman, A. Moretto, S. Oancea, M. Jost, F. Formaggio, C. Toniolo, *J.Pept.Res.* **2005**, 65 564-579.
- [9] M. Grimaldi, M. Scrima, C. Esposito, G. Vitiello, A. Ramunno, V. Limongelli, G. D'Errico, E. Novellino, A. M. D'Ursi, *Biochim.Biophys.Acta* **2010**, 1798 660-671.
- [10] P. Hanson, G. Martinez, G. Millhauser, F. Formaggio, M. Crisma, C. Toniolo, C. Vita, *Journal of the American Chemical Society* **1996**, 118 271-272.
- [11] V. Monaco, F. Formaggio, M. Crisma, C. Toniolo, P. Hanson, G. L. Millhauser, *Biopolymers* **1999**, 50 239-253.
- [12] S. Stoller, G. Sicoli, T. Y. Baranova, M. Bennati, U. Diederichsen, *Angew.Chem.Int.Ed Engl.* **2011**, 50 9743-9746.
- [13] C. Toniolo, M. Crisma, F. Formaggio, *Biopolymers* **1998**, 47 153-158.
- [14] I. L. Karle, P. Balaram, *Biochemistry* **1990**, 29 6747-6756.
- [15] C. Toniolo, G. M. Bonora, V. Barone, A. Bavoso, E. Benedetti, B. Diblasio, P. Grimaldi, F. Lelj, V. Pavone, C. Pedone, *Macromolecules* **1985**, 18 895-902.
- [16] C. Toniolo, M. Crisma, F. Formaggio, C. Peggion, *Biopolymers* **2001**, 60 396-419.
- [17] E. Benedetti, B. B. Di, V. Pavone, C. Pedone, C. Toniolo, M. Crisma, *Biopolymers* **1992**, 32 453-456.
- [18] K. A. Bolin, G. L. Millhauser, *Accounts of Chemical Research* **1999**, 32 1027-1033.
- [19] C. Toniolo, E. Benedetti, *Trends Biochem.Sci.* **1991**, 16 350-353.
- [20] Luckhurst G.R., in *spin labeling* **1976**, p. pp. 133-179.
- [21] E. J. Hustedt, A. I. Smirnov, C. F. Laub, C. E. Cobb, A. H. Beth, *Biophys.J.* **1997**, 72 1861-1877.
- [22] M. Zerbetto, S. Carlotto, A. Polimeno, C. Corvaja, L. Franco, C. Toniolo, F. Formaggio, V. Barone, P. Cimino, *Journal of Physical Chemistry B* **2007**, 111 2668-2674.
- [23] Goodman M., A. Felix, C. Moroder, C. Toniolo, Ed.: G. Thieme: Stuttgart) **20103**, p. pp. 292-310.
- [24] L. A. Carpino, *Journal of the American Chemical Society* **1993**, 115 4397-4398.
- [25] D. S. Jones, *Proceedings of the Cambridge Philosophical Society-Mathematical and Physical Sciences* **1965**, 61 223-&.
- [26] S. Stoll, A. Schweiger, *Journal of Magnetic Resonance* **2006**, 178 42-55.
- [27] M. H. Baron, C. Deloze, C. Toniolo, G. D. Fasman, *Biopolymers* **1978**, 17 2225-2239.
- [28] G. M. Bonora, C. Mapelli, C. Toniolo, R. R. Wilkening, E. S. Stevens, *International Journal of Biological Macromolecules* **1984**, 6 179-188.
- [29] F. Scarpelli, M. Drescher, T. Rutters-Meijneke, A. Holt, D. T. Rijkers, J. A. Killian, M. Huber, *J.Phys.Chem.B* **2009**, 113 12257-12264.
- [30] H. J. Steinhoff, *Frontiers in Bioscience* **2002**, 7 C97-C110.
- [31] J. C. McNulty, J. L. Silapie, M. Carnevali, C. T. Farrar, R. G. Griffin, F. Formaggio, M. Crisma, C. Toniolo, G. L. Milhauser, *Biopolymers* **2000**, 55 479-485.
- [32] C. J. Gorter, J. H. van Vleck, *Physical Review* **1947**, 72 1128-1129.
- [33] S. Carlotto, P. Cimino, M. Zerbetto, L. Franco, C. Corvaja, M. Crisma, F. Formaggio, C. Toniolo, A. Polimeno, V. Barone, *J.Am.Chem.Soc.* **2007**, 129 11248-11258.
- [34] E. Sartori, C. Corvaja, S. Oancea, F. Formaggio, M. Crisma, C. Toniolo, *Chemphyschem* **2005**, 6 1472-1475.

APPENDIX A

SUPPORTING INFORMATION ON THE MODEL OF ONE A β PER MICELLE DESCRIBED IN CHAPTER 2

In chapter 2, the effect of the membrane mimicking detergent SDS on the aggregation of the A β peptide is investigated. We propose that at SDS concentrations above the critical micelle concentration (CMC) only one species is present, which we assign to a monomeric, micelle bound form of A β . If A β in this form is indeed monomeric, non-diamagnetically diluted samples should show the same spectrum as the diamagnetically diluted samples investigated in chapter 2. The figure shows that this is the case, confirming the one A β per micelle model.

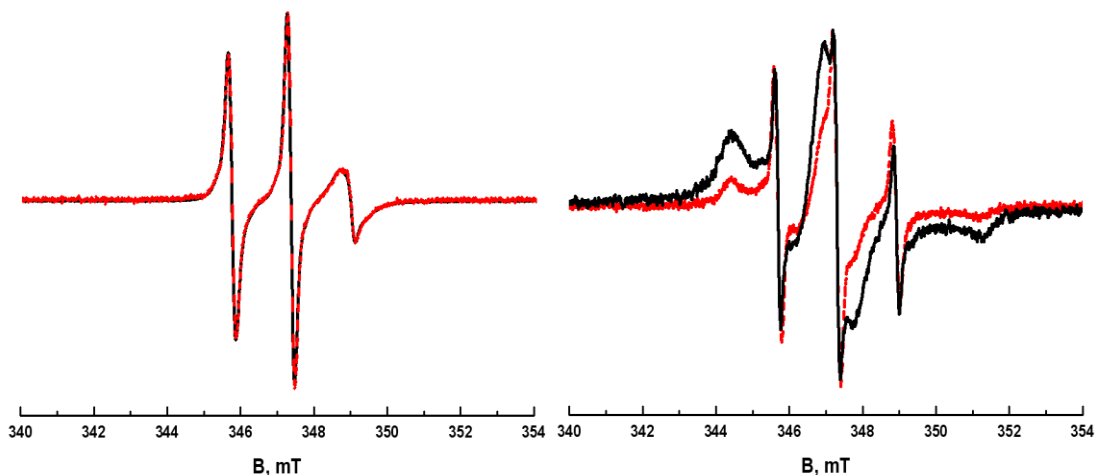


Figure A.1 Room temperature continuous wave EPR spectra of SL-A β 40 comparing diamagnetically diluted (red line) with non-diamagnetically diluted (black line) samples. Left: Spectra of SL-A β 40 at high SDS concentrations with D/P of 130.9 (SDS = 72 mM). The spectra consist of one mobility component with a rotation-correlation time of 0.93 ± 0.03 ns. Black and red spectra are identical within the signal to noise. Right: Spectra of SL-A β 40 in the absence of SDS, i.e., D/P = 0. The spectra consist of at least three mobility components, fast, medium, and slow. The corresponding rotation-correlation times and the contributions of each component are given in chapter two of this thesis. Given in black is the non-diluted SL-A β 40 at a D/P = 0. Similar to the red spectrum, the black spectrum consists of at least three mobility components. The contribution of the fast component to the spectrum of the non-diluted SL-A β 40 is smaller than that of the diamagnetically diluted SL-A β 40. Also, the slow component has a larger contribution to the spectrum of the non-diluted SL-A β 40, compared to that of the diamagnetically diluted SL-A β 40. We attribute the overall broadening in the right part of the figure to spin-spin interaction. Such a broadening is absent in the spectra given on the left, confirming the one A β per micelle model described in chapter 2.

APPENDIX B

THE TRIANGULATION APPROACH USED IN CHAPTER 6: CALCULATING THE POSITION OF RESIDUE 4 OF CP29

In chapter 6, the N-terminus of the light-harvesting protein CP29 is studied. The triangulation approach is used to determine the position of the end (residue 4) of the N-terminus, which is explained in this appendix. The distances between residue 4 and residues 101 and 205, and between residue 4 and a chlorophyll as obtained from a time-resolved FRET study ^[1] define the position.

The triangulation approach used in chapter 6: calculating the position of residue 4 of CP29

For the triangulation of the unknown position of residue 4 of CP29 we start from three known atom positions: A, B and C. To determine the position of residue 4, we have three experimental distances from atoms A, B and C to residue 4 that are measured either by DEER (table B.1) or by FRET.

The distances a and b between A respectively B and the residue 4 define the radius of spheres around A and B that intersect as a circle between A and B (figure B.1). The distance c (distance between C and residue 4) defines a sphere around C with a radius of c . This sphere can have two points of intersection with the circle between A and B, one of these points is the position sought. The atoms are selected such that the distance AB (r_{AB}) is longer than the distance AC (r_{AC}). The lines joining these three positions r_{AB} , r_{AC} , and r_{BC} (figure B.1) define the sides of a triangle.

Amongst the three experimentally determined distances (a , b , and c), two are obtained from DEER measurements: residue 4 to residue 101 (88 in *Spinach*) and residue 4 to residue 205 (191 in *Spinach*). The third distance is the distance between residue 4, labeled with a fluorescent dye ^[1], and a chlorophyll taken from FRET data reported earlier ^[1].

The FRET distance of 1.8 nm refers to a distance between residue 4 and one of the 13 chlorophylls in the CP29 protein. To account for this, all 13 chlorophylls are considered individually and the coordinates of their central Mg-atom are combined with the other two C_{α^-} positions. We exclude only those chlorophylls whose Mg atoms are farther than 30 Å from the C_{α^-} atoms of residue 101 (88 in *Spinach*) or of residue 205 (191 in *Spinach*), because if these distances are larger, the chlorophylls are located on the other, luminal side of the protein and therefore cannot contribute to FRET with residue 4. Eight chlorophylls remain, which are listed in table B.2.

Table B.1 Distance parameters of the doubly spin-labeled CP29 (for details see chapter 6) derived from the analysis of DEER data selected and labeled as used in the present model. Given are: $\langle r \rangle$, distance in nm; $S(r)$, the width of the distance distribution in nm, % shows the contribution of each peak. The width of the distance distributions reflects the conformation distribution of the N-terminus as well as the distribution of the conformations of the spin-label linkers.

mutant	short (s)			medium (m)			long (l)		
	$\langle r_s \rangle$ nm	$S(r_s)$ nm	%	$\langle r_m \rangle$ nm	$S(r_m)$ nm	%	$\langle r_l \rangle$ nm	$S(r_l)$ nm	%
4/97C	3.19	0.84	28	4.27	0.67	20	4.94	0.98	52
4/101C	1.96	1.28	35	3.53	0.68	22	5.14	0.95	43
4/205C	3.14	0.84	15	3.69	0.34	2	5.06	0.76	39

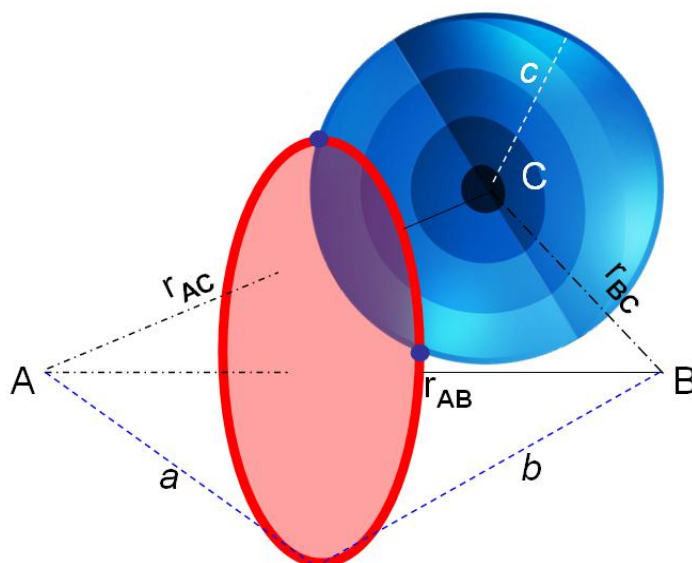


Figure B.1 Principle of the triangulation approach. For the triangulation we use three atom positions: A, B, and C. The coordinates of the three atom positions, C_{α^-} for residues 101 (88 in *Spinach*), 205 (191 in *Spinach*), and the central Mg-atom of the chlorophylls are taken from the CP29 pdb file (access code: 3PL9) ^[2]. The vectors joining these three positions (r_{AB} , r_{AC} , and r_{BC}) define the sides of a triangle. The distances a and b between A or B to the residue of interest define spheres around A and B that intersect as a circle between A and B (shown as a red circle). The distance c defines a sphere around C with radius c . This sphere can have two intersections with the red circle (shown as blue dots), one of them the residue position sought. The sides were defined such that r_{AB} is longer than r_{AC} .

Table B.2 Distance combinations considered to determine the location of residue 4 in CP29. Given are the 72 possible combinations in two sections of the table, which comprise the five left-hand and the five right-hand columns each. In the first column, the number of the chlorophylls is given together with the atom label A, B, and C used in the computation. The second column gives the distances from DEER, either for the 4/101 or for the 4/205 mutant. The letters s, m, and l stand for short, medium and long distance derived from DEER analysis. The remaining three columns give the distances: *a*, *b*, and *c*. Nine rows describe all possible distance combinations for the chlorophyll in question.

section 1					section 2				
		a (Å)	b (Å)	c (Å)			a (Å)	b (Å)	c (Å)
CHL602 A: CHL B: 205 C: 101	1: 101(s), 205(s)	18	31.4	19.6	CHL610 A: CHL B: 101 C: 205	1: 101(s), 205(s)	18	19.6	31.4
	2: 101(s), 205(m)	18	36.9	19.6		2: 101(s), 205(m)	18	19.6	36.9
	3: 101(s), 205(l)	18	50.6	19.6		3: 101(s), 205(l)	18	19.6	50.6
	4: 101(m), 205(s)	18	31.4	35.3		4: 101(m), 205(s)	18	35.3	31.4
	5: 101(m), 205(m)	18	36.9	35.3		5: 101(m), 205(m)	18	35.3	36.9
	6: 101(m), 205(l)	18	50.6	35.3		6: 101(m), 205(l)	18	35.3	50.6
	7: 101(l), 205(s)	18	31.4	51.4		7: 101(l), 205(s)	18	51.4	31.4
	8: 101(l), 205(m)	18	36.9	51.4		8: 101(l), 205(m)	18	51.4	36.9
	9: 101(l), 205(l)	18	50.6	51.4		9: 101(l), 205(l)	18	51.4	50.6
CHL603 A: 101 B: 205 C: CHL	1: 101(s), 205(s)	19.6	31.4	18	CHL611 A: 205 B: 101 C: CHL	1: 101(s), 205(s)	31.4	19.6	18
	2: 101(s), 205(m)	19.6	36.9	18		2: 101(s), 205(m)	36.9	19.6	18
	3: 101(s), 205(l)	19.6	50.6	18		3: 101(s), 205(l)	50.6	19.6	18
	4: 101(m), 205(s)	35.3	31.4	18		4: 101(m), 205(s)	31.4	35.3	18
	5: 101(m), 205(m)	35.3	36.9	18		5: 101(m), 205(m)	36.9	35.3	18
	6: 101(m), 205(l)	35.3	50.6	18		6: 101(m), 205(l)	50.6	35.3	18
	7: 101(l), 205(s)	51.4	31.4	18		7: 101(l), 205(s)	31.4	51.4	18
	8: 101(l), 205(m)	51.4	36.9	18		8: 101(l), 205(m)	36.9	51.4	18
	9: 101(l), 205(l)	51.4	50.6	18		9: 101(l), 205(l)	50.6	51.4	18
CHL608 A: CHL B: 101 C: 205	1: 101(s), 205(s)	18	19.6	31.4	CHL612 A: 205 B: 101 C: CHL	1: 101(s), 205(s)	31.4	19.6	18
	2: 101(s), 205(m)	18	19.6	36.9		2: 101(s), 205(m)	36.9	19.6	18
	3: 101(s), 205(l)	18	19.6	50.6		3: 101(s), 205(l)	50.6	19.6	18
	4: 101(m), 205(s)	18	35.3	31.4		4: 101(m), 205(s)	31.4	35.3	18
	5: 101(m), 205(m)	18	35.3	36.9		5: 101(m), 205(m)	36.9	35.3	18
	6: 101(m), 205(l)	18	35.3	50.6		6: 101(m), 205(l)	50.6	35.3	18
	7: 101(l), 205(s)	18	51.4	31.4		7: 101(l), 205(s)	31.4	51.4	18
	8: 101(l), 205(m)	18	51.4	36.9		8: 101(l), 205(m)	36.9	51.4	18
	9: 101(l), 205(l)	18	51.4	50.6		9: 101(l), 205(l)	50.6	51.4	18
CHL609 A: 101 B: 205 C: CHL	1: 101(s), 205(s)	19.6	31.4	18	CHL615 A: 205 B: 101 C: CHL	1: 101(s), 205(s)	31.4	19.6	18
	2: 101(s), 205(m)	19.6	36.9	18		2: 101(s), 205(m)	36.9	19.6	18
	3: 101(s), 205(l)	19.6	50.6	18		3: 101(s), 205(l)	50.6	19.6	18
	4: 101(m), 205(s)	35.3	31.4	18		4: 101(m), 205(s)	31.4	35.3	18
	5: 101(m), 205(m)	35.3	36.9	18		5: 101(m), 205(m)	36.9	35.3	18
	6: 101(m), 205(l)	35.3	50.6	18		6: 101(m), 205(l)	50.6	35.3	18
	7: 101(l), 205(s)	51.4	31.4	18		7: 101(l), 205(s)	31.4	51.4	18
	8: 101(l), 205(m)	51.4	36.9	18		8: 101(l), 205(m)	36.9	51.4	18
	9: 101(l), 205(l)	51.4	50.6	18		9: 101(l), 205(l)	50.6	51.4	18

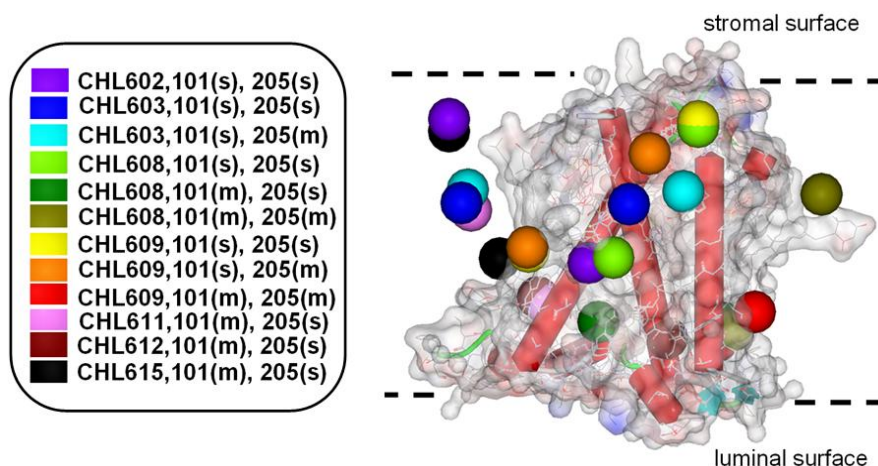


Figure B.2 Location of all geometrically possible positions for residue 4 within the structure of CP29. The orientation of CP29 is such that the membrane stromal surface is horizontal and follows the top surface of the protein. The positions are determined using the distances, which were measured with DEER (chapter 6) and FRET ^[1], as described in the text. Using the triangulation approach, 12 points of intersection are obtained. The intersection points are presented as spheres in different colors. Each color corresponds to one chlorophyll (CHL) number (see legend) and the distances from DEER, s: short, m: medium, and l: long. Six out of the 12 positions are physically possible positions for residue 4.

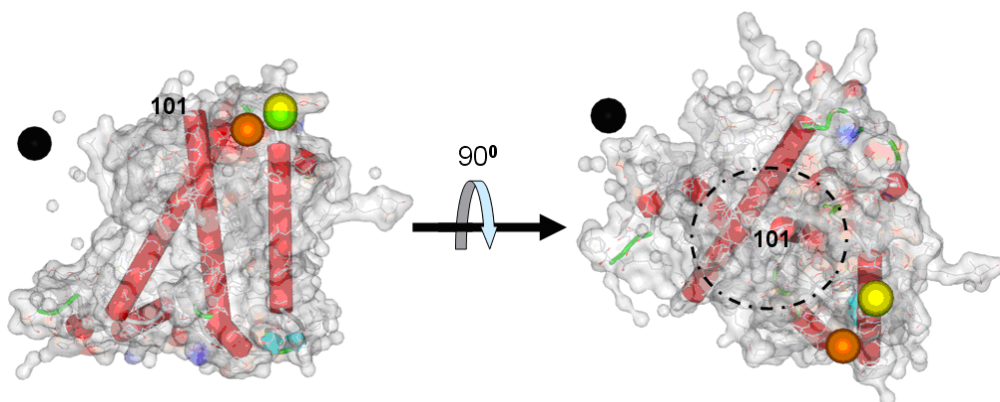


Figure B.3 The four most likely positions of residue 4, selected from those in figure B.2. The orientation of CP29 on the left is as in figure B.2. On the right, the view onto the stromal surface of the protein is shown. These positions are given as spheres with different colors. Three of these spheres (the green, yellow, and orange sphere) cluster in the area where helices B and C reach the protein stromal surface, and the black sphere is located farther from the stromal surface of the protein, close to the membrane surface. The projection of the protein is so that it is hiding two of the spheres representing the position of residue 4 (shown in yellow and green). The dotted circle indicates the possible location of residue 97 (see chapter 6 of this thesis).

Each of the DEER experiments probing the separation of residue 4 with residues 101 or 205 resulted in three distances, s, m, and l (see chapter 6 of this thesis). Combining the eight possible Mg atom positions and the three distances found for each DEER experiment results in the 72 combinations listed in table B.2. Amongst these 72 combinations, only 12 have points of intersection as defined in figure B.2. All these points are shown in figure B.2 as spheres, color coded to indicate the combination of distances that gives rise to these solutions. Because every combination gives rise to two intersection points, only six of these 12 solutions are physically meaningful, i.e., represent possible positions of residue 4. We discarded all points that were in the interior of the protein or the membrane, which leaves us with the four points discussed in chapter 6 of this thesis (figure B.3).

Reference List

- [1] B.A.Berghuis, R.B.Spruijt, R.B.M.Koehorst, A.van Hoek, S.P.Laptenok, B.van Oort, H.van Amerongen, *European Biophysics Journal with Biophysics Letters* **2010**, 39 631-638.
- [2] X.Pan, M.Li, T.Wan, L.Wang, C.Jia, Z.Hou, X.Zhao, J.Zhang, W.Chang, *Nat.Struct.Mol.Biol.* **2011**, 18 309-315.

LIST OF ABBREVIATIONS

Aβ	amyloid beta
AD	Alzheimer's disease
APP	amyloid precursor protein
αS	alpha synuclein
CMC	critical micelle concentration
cw	continuous wave
DEER	double electron electron resonance
DMSO	anhydrous dimethyl sulfoxide
DTT	DL-dithiothreitol
EPR	electron paramagnetic resonance
J	the exchange interaction
LHCII	light harvesting complex II
MTS	((1-oxyl-2,2,5,5-tetramethylpyrroline-3-methyl) methanethiosulfonate)
mw	microwave
PBS	phosphate-buffered saline
PD	Parkinson's disease
PSII	photosystem II
SDS	sodium dodecyl sulfate
ThioT	thioflavin T
TOAC	alpha-amino acid 2,2,6,6-tetramethylpiperidine-1-oxyl-4- amino-4-carboxylic acid
τ_r	rotation-correlation time

SUMMARY

The work reported in this thesis concerns novel methods to investigate the aggregation and misfolding of intrinsically disordered proteins, and the characterization of disordered parts of proteins by EPR. Such questions are difficult if not impossible to study with other approaches. To this aim, both pulsed and cw EPR has been applied and nitroxide spin labels are used as paramagnetic probes. In chapter 1 details of the EPR methods used are provided. In chapters 2 to 4 the aggregation of the amyloid β (A β) peptide is investigated. In chapter 5 the structure of the α -synuclein protein in its fibrillar state is described. Chapter 6 concerns the conformation of a disordered region in a protein, and chapter 7 the spin-spin interaction in a series of model peptides.

In chapters 2 to 4 we describe the aggregation of the A β peptide. This peptide plays a role in Alzheimer's disease. Two themes are treated: the effect of membrane mimics (chapters 2 and 3) and the role of shorter A β fragments (chapter 4). We used sodium dodecyl sulfate (SDS) detergent as membrane mimicking agent. The EPR approach enables us to monitor the changes occurring in the reaction mixture in the presence of different amounts of SDS on the time scale of aggregation.

In chapter 2 we observe that with increasing SDS concentration the A β aggregates become smaller as the concentration of SDS increases, until at SDS concentrations above the critical micelle concentration (CMC) a monomeric, micelle-bound form of A β is the only species remaining, the “one A β /micelle” state. In chapter 3 we place our magnifier on the SDS concentration regime below the CMC. To understand the results obtained at SDS concentrations below the CMC we eliminate the effect of local mobility of the spin label, by comparing two different label positions, which is particularly important. At the lower end of these SDS concentrations, the N-terminus of A β participates in the solubilization by being located at the particle/water interface. At higher SDS concentrations, the aggregate changes to an SDS-solubilized state that is a precursor to the “one A β /micelle” state above the CMC. In this chapter, we demonstrate how global properties of the A β -aggregation state can be obtained from the local mobility parameters.

In chapter 4 the aggregation potential of two shorter fragments, A β 15 and A β 16, and their influence on A β 40 is described. The shorter A β fragments draw a lot of attention especially in the search for indicators of Alzheimer's disease. However, the role of these shorter fragments in aggregation of the full-length A β is under debate. We show in chapter 4 that neither A β 15 nor A β 16 aggregate by themselves and that they do not influence the aggregation of A β 40.

One of the consequences of using EPR as done here is the requirement of relatively high concentrations of peptide. At these concentrations the A β peptide forms aggregates and fibrils very quickly, i.e., within minutes. But even this strong tendency to aggregate can be suppressed by SDS, and above the CMC the A β peptides become monomeric. In addition, we learn that the global properties of A β aggregates depend on the SDS concentration. The results of chapters 2 to 4 reveal the unique potential of EPR in studying the aggregation of the A β peptide.

In chapter 5 we investigate the α -synuclein protein, which, similar to A β , can form fibrils. This protein has a role in Parkinson's disease. We focus on the fibrillar state of α -synuclein. A series of α -synuclein proteins are used with two spin labels at different positions. After the formation of the α -synuclein fibril, the distance between pairs of spin-labeled residues in the fibril is measured with pulsed double electron-electron resonance spectroscopy, DEER. We find that the N-terminus up to residue 27 is unstructured and extends away from the fibril core. We propose a model for the fibril core, based on three intra-molecular distances, thus revealing the fold of a substantial part of the fibril core.

In chapter 6 we investigate the light-harvesting protein CP29, combining cw EPR and pulsed EPR. The CP29 protein is an antenna protein in photosynthesis, the process by which solar energy is converted to chemical energy in plants. The CP29 protein has a disordered region, the unusually long N-terminal domain (about 100 amino-acid residues). For light-regulation within the plant antenna system, CP29 seems to make use of this N-terminus. Even though the crystal structure of the CP29 protein was determined, the structure of the N-terminal domain remained elusive. In chapter 6, we demonstrate that the N-terminus of CP29 is partly structured and five regions are recognized that differ considerably in their dynamics. Two regions are relatively immobile, and one of the immobile regions shows α -helical character and is in contact with the bulk of the protein. This immobile part is flanked by highly dynamic and rather unstructured regions (loops). We speculate that the different conformations may be important for the interaction with other light-harvesting complexes and enable the protein to switch between different protein complexes within the photosynthetic membrane to help the plant adapt to different light conditions.

In chapter 7 we target spin-spin interaction in liquid solution at room temperature. Here we use a series of rigid model peptides, containing pairs of TOAC spin labels. The pairs of spin labels are separated by three, four, and five amino acids. These rigid biradical peptides enable a systematic characterization of the spin-spin interaction in these peptides, which can be compared to the structure of the peptide.

Here we determine the exchange interaction J of the two spins. For selected peptides also the dipolar interaction is measured. Overall, a decrease of J with increasing separation of the two TOAC residues is observed. Our results show that in these helical peptides the through-bond contribution dominates over the through-space contribution, which gives rise to a substantial J even over a separation of 12 Å. Although liquid-solution studies are more favorable for biological systems than the frozen state, we learned in chapter 7 that the information we can obtain in liquid solution is ambiguous. Specifically, in contrast to the dipolar interaction, no direct distance information can be obtained from the quantity J . Therefore, more information can be determined in the frozen state, i.e., from dipolar interaction, as demonstrated in chapter 5 and 6 of this thesis. A combination of both approaches is needed to understand the scope of the protein structures.

The work described in this thesis shows that EPR methods are useful in determining aspects of protein structure that are difficult to probe otherwise. This brings the big challenge of solving the molecular structure of proteins one step further.

SAMENVATTING

Het werk beschreven in dit proefschrift betreft nieuwe methoden om de aggregatie van eiwitten te onderzoeken met elektron-paramagnetische-resonantie (EPR) spectroscopie, in het bijzonder van eiwitten die fibrillen vormen. Daartoe zijn zowel experimenten met continue microgolffexcitatie (cw) als experimenten met gepulste microgolffexcitatie uitgevoerd. Als paramagnetische sensoren zijn nitroxide spinlabels gebruikt. In hoofdstuk 1 worden de gebruikte EPR methoden beschreven. De hoofdstukken 2 tot en met 4 betreffen de aggregatie van het amyloid β ($A\beta$) peptide. In hoofdstuk 5 wordt de structuur van het α -Synuclein (αS) eiwit in het corresponderende fibril beschreven. Hoofdstuk 6 betreft de conformatie van een ongeordend gebied in een eiwit, hoofdstuk 7 de spin-spin wisselwerking in een reeks van modelpeptiden.

In hoofdstuk 2 tot en met 4 beschrijven wij de aggregatie van het $A\beta$ peptide. Dit peptide speelt een rol bij de ziekte van Alzheimer. In deze hoofdstukken komen twee aspecten aan de orde: de invloed van het membraan, dat wij nabootsen met natrium dodecyl sulfaat (SDS), en de rol van kortere $A\beta$ fragmenten. Met behulp van EPR kunnen wij de veranderingen in het reactiemengsel ten gevolge van de aanwezigheid van verschillende hoeveelheden SDS op de tijdschaal van aggregatie volgen.

In hoofdstuk 2 laten wij zien dat de $A\beta$ aggregaten, die aanwezig zijn in de afwezigheid van SDS, steeds kleiner worden naarmate de concentratie van SDS toeneemt, totdat bij SDS concentraties boven de kritische-micel-concentratie (CMC) een monomeer, micel-gebonden vorm van $A\beta$ als enige overblijft, de "één $A\beta$ /micelle" toestand.

In hoofdstuk 3 richten wij ons op SDS concentraties onder de CMC. Door gebruik te maken van twee verschillende posities van het label, wordt het effect van de lokale mobiliteit van het spin label geëlimineerd. Dit is belangrijk voor de interpretatie van de resultaten bij deze SDS concentraties. Bij de laagste concentraties SDS draagt de N-terminus van $A\beta$ bij aan de oplossing van $A\beta$ aggregaten door zich te positioneren aan het deeltje/water-grensvlak. Bij hogere concentraties van SDS veranderen de $A\beta$ aggregaten in een SDS-opgeloste toestand, die een voorloper is van de "één $A\beta$ / micelle" toestand boven de CMC. In dit hoofdstuk laten we zien hoe uit parameters die de lokale mobiliteit reflecteren, globale eigenschappen van de $A\beta$ aggregaten kunnen worden afgeleid.

In hoofdstuk 4 beschrijven wij de mogelijkheid van aggregatie van twee kortere fragmenten, $A\beta_{15}$ en $A\beta_{16}$, en hun invloed op $A\beta_{40}$. De kortere $A\beta$ fragmenten

trekken veel aandacht, in het bijzonder in relatie tot het zoeken naar remmers van A β aggregatie. De rol van deze kortere fragmenten in de aggregatie van A β 40 staat echter nog ter discussie. In hoofdstuk 4 laten wij zien dat geen van de korte fragmenten, A β 15 noch A β 16, op zichzelf aggregeren en dat zij geen invloed hebben op de aggregatie van A β 40.

Bij het gebruik van EPR zijn hoge peptide concentraties niet te vermijden. Bij deze hoge concentraties vormen A β 40 peptiden binnen enkele minuten aggregaten en fibrillen. Maar zelfs deze sterke neiging tot aggregeren kan door SDS worden onderdrukt. Bovendien komt boven de CMC het A β voor als monomeer. Daarnaast hebben wij geleerd dat de globale eigenschappen van A β aggregaten afhankelijk zijn van de SDS concentratie.

In hoofdstuk 5 onderzoeken wij het α S eiwit, dat soortgelijke fibrillen kan vormen als A β . Dit eiwit speelt een rol bij de ziekte van Parkinson. In dit hoofdstuk richten wij ons op de fibril vorm van α S. Een reeks van α S eiwitten wordt gebruikt met twee spin labels op verschillende posities. Na de vorming van de fibrillen wordt de afstand tussen die paren in het fibril gemeten in een gepulst EPR experiment met gebruikmaking van de zogenoemde DEER methode. Uit onze resultaten bleek dat de N-terminus van het α S eiwit tot aan residue 27 ongestructureerd is en zich uitstrekt weg van de kern van het fibril. Gebaseerd op drie van de gemeten intra-moleculaire afstanden stellen wij een model op voor de vouwing van een aanzienlijk deel van de kern van het fibril.

In hoofdstuk 6 onderzoeken wij het “light-harvesting” complex CP29 met behulp van cw EPR en gepulste EPR. Het CP29 eiwit speelt een belangrijke rol in de fotosynthese, het proces waarbij zonne-energie wordt omgezet in chemische energie. Dit eiwit heeft een ongeordend deel van ongebruikelijke lengte, ongeveer 100 aminozuren aan het N-terminale deel van het eiwit. Onlangs is de kristalstructuur van dit eiwit bepaald met behulp van Röntgen-diffractie, maar de structuur van de N-terminus bleef onbepaald.

In hoofdstuk 6 laten wij zien dat de N-terminus van CP29 gedeeltelijk gestructureerd is en dat daarin vijf gebieden herkend kunnen worden die verschillen in hun dynamiek. Twee gebieden zijn relatief meer immobiel, en een van de immobiele gebieden heeft het karakter van een α -helix, en is in contact met de bulk van het eiwit. Dit immobiele deel wordt geflankeerd door meer dynamische gebieden (“loops”). Wij speculeren dat de verschillende conformaties belangrijk zijn voor de interacties met andere “light-harvesting” complexen, waardoor het eiwit tussen verschillende gebieden van het fotosynthetisch membraan kan schakelen om de plant te helpen zich aan verschillende lichtomstandigheden aan te passen.

In hoofdstuk 7 adresseren wij de spin-spin interactie in vloeibare oplossing bij kamertemperatuur. Hier gebruiken wij een reeks van rigide modelpeptiden voorzien van paren van TOAC spin labels. De paren van spin labels zijn gescheiden door drie, vier of vijf aminozuren.

Met behulp van deze rigide biradicaal peptiden kunnen wij de spin-spin interactie in deze peptiden systematisch karakteriseren en die interactie vergelijken met de structuur van het peptide. Wij bepalen de exchange-wisselwerking J van de twee spins. Voor geselecteerde peptiden meten wij ook de dipolaire interactie. De waarde van J neemt af met toenemende afstand van de twee TOAC residuen. Onze resultaten laten zien dat in deze spiraalvormige peptiden de “through-bond” bijdrage tot J groter is dan de “through-space” bijdrage; hierdoor heeft J nog een aanzienlijke grootte, zelfs bij een scheiding van de residuen van 12 Å. Hoewel voor biologische systemen studies in vloeibare oplossing geschikter zijn dan in de bevroren toestand, zien wij dat de informatie die wij kunnen krijgen in vloeibare oplossing niet eenduidig is. In het bijzonder geeft de exchange-wisselwerking geen directe afstands-informatie, dit in tegenstelling tot de dipolaire interactie. Meer informatie kan verkregen worden in de bevroren toestand, zoals aangetoond in de hoofdstukken 5 en 6 van dit proefschrift. Een combinatie van beide benaderingen is nodig om verschillende aspecten van de eiwitstructuur te begrijpen.

In dit proefschrift hebben wij laten zien hoe met behulp van EPR informatie kan worden verkregen met betrekking tot de structuur van eiwitten die moeilijk op een andere manier toegankelijk is. Daarmee dragen wij bij aan de bepaling van de moleculaire structuur van eiwitten.

PUBLICATIONS

Journal papers

- 2012** Scanu S., Förster J., Finiguerra M., **Hashemi Shabestari M.**, Huber M., Ubbink M. "The complex of cytochrome f and plastocyanin from *Nostoc* sp. PCC 7119 is highly dynamic". *Chembiochem.* (2012), 13: 1312-8.
- 2011** Carlotto S., Zerbetto m., **Hashemi Shabestari M.**, Toniolo C., Huber M., Polimeno A. "In Silico interpretation of cw-ESR at 9 and 95 GHz of Mono- and bis- TOAC labeled Aib-homopeptides in fluid and frozen acetonitrile". *J. Phys.Chem. B.* (2011), 115: 13026-36.
- 2006** **Hashemi Shabestari M.**, Sarbolouki M.N. "Novel transdermal drug delivery systems". *Iranian Journal of Dermatology.* (2006), 9: 270-283.

Published abstracts

- 2013** **Hashemi Shabestari M.**, Wolfs C., Spruijt R., van Amerongen H., Huber M. "The disordered N-terminus of the plant antenna protein CP29 studied by EPR- is this 100 residue stretch unstructured". *Biophysical Journal.* (2013), 104: p219a.
- 2013** **Hashemi Shabestari M.**, Segers-Nolten I.M.J., Meeuwenoord N.J., Filippov D.V., Claessens M.M.A.E., van Rooijen B.D., Subramaniam V., Huber M. "Aggregation and membrane interaction of alpha-synuclein and amyloid β by electron paramagnetic resonance". *Biophysical Journal.* (2013), 104: p52a.
- 2012** **Hashemi Shabestari M.**, Segers-Nolten I.M.J., Subramaniam V., Huber M. "Elucidating the α Synuclein Fibril Fold by Pulsed EPR". *Biophysical Journal.* (2012), 102: 441a.
- 2012** **Hashemi Shabestari M.**, Meeuwenoord N.J., Filippov D.V., Huber M. "The effect of a membrane mimicking detergent on Alzheimer's amyloid peptide aggregation studied by EPR". *Biophysical Journal.* (2012), 102: 454a.
- 2010** **Hashemi Shabestari M.**, Sepkhanova I., Drescher M., Meeuwenoord N.J., Filippov D.V., Limpens R., Koning R.I., Huber M. "Detecting the aggregation of amyloid peptides by Spin Label EPR". *Biophysical Journal.* (2010), 98: 458a.

In preparation

- 2013** **Hashemi Shabestari M.**, van Son M., Moretto A., Crisma M., Toniolo C., Huber M. “Structure and first EPR characterization of helical peptides with TOAC spin-labels: models for short distances”.
- 2013** **Hashemi Shabestari M.**, Meeuwenoord N.J., Filippov D.V., Huber M. “The interaction of amyloid β peptide with a membrane mimicking detergent using EPR”.
- 2013** **Hashemi Shabestari M.**, Plug T., Motazacker M.M., Meeuwenoord N.J., Filippov D.V., Meijers J., Huber M. “The aggregation potential of the 1-15 and 1-16 fragments of the amyloid β peptide and their influence on the aggregation of A β 40”.

CURRICULUM VITAE

Maryam Hashemi Shabestari was born on September 21, 1979 in Tehran, Iran. After graduating from high school in 1997, she studied plant biology at the Faculty of Sciences at Tehran University, and received her bachelor's degree (with honor) in 2001. She obtained her MSc. degree in biophysics in 2004 from the Institute of Biophysics and Biochemistry at Tehran University with a focus on preparation and evaluation of lipid formulations in transdermal drug delivery. Her MSc. thesis work was presented at the "European conference on drug delivery and pharmaceutical technology" in Seville, Spain in 2004 and at the "49th annual meeting of Biophysical Society" in Long Beach, California in 2005. She then worked as a research assistant at the Osvah (ex IRAN-Merck) pharmaceutical company and as a part-time instructor at Tehran University.

In 2008, she started her PhD at the Department of Molecular Physics at Leiden University under the supervision of Prof. dr. Edgar Groenen and Dr. Martina Huber. Her research concerned determining the structure, dynamics, and interaction of proteins, specifically fibril-forming proteins involved in neurodegenerative disorders, using advanced Electron Paramagnetic Resonance (EPR) methods. During her PhD period, she contributed to the teaching at the Department of Physics by assisting the 2nd year and 3rd year physics course for biology students and supervised a four month bachelor project in the Molecular Physics group. She was also involved in the "LAPP-Top program (Leiden Advanced Pre-university Program for Top students). In addition, she has attended several national and international workshops and training courses. She has presented the results of her research orally at the NWO study group meeting on Protein research, Nucleic acids, Lipids, and Biomembranes (2010, Veldhoven, Netherlands), at the 44th Annual International Meeting of the ESR Spectroscopy Group of the Royal Society of Chemistry (2011, York, UK), at the 19th meeting of the Benelux EPR Society (2011, Antwerp, Belgium), and at the physics@FOM meeting (2013, Veldhoven, Netherlands). Besides several national symposia and meetings, her work was presented as a poster at the 7th European Federation of EPR (2009, Antwerp, Belgium), and at the 5th EF-EPR Summer School on Advanced EPR Spectroscopy (2010, Konstanz, Germany). In November 2010, she was awarded the 2010 Holland Research School of Molecular Chemistry (HRSMC) poster prize with a project titled: "Aggregation of transmembrane peptides studied by spin-label EPR". Her PhD program was supported by the "Stichting voor Fundamenteel Onderzoek der Materie (FOM)" and resulted in this thesis.

ACKNOWLEDGEMENT

Although the cover of this thesis bears only my name, many people have contributed to the work in this thesis. I gladly acknowledge their contribution here.

First of all, I would like to thank Dr. Martina Huber for giving me the opportunity to do a PhD in the MoNOS group. There is no PhD trajectory without ups and downs, and I greatly appreciate the strong support and wise decisions of Prof. Edgar Groenen during my PhD period, which helped me to stay on track.

I would like to acknowledge Prof. Vinod Subramaniam and Prof. Herbert van Amerongen for providing me with the samples and giving me the permission to use their facilities. I would like to acknowledge Prof. Joost Meijers for generously supplying me with materials and allowing me to use their facilities in his lab, and Tom Plug who kindly helped me with performing the measurements. I appreciate our collaboration with Prof. Marcellus Ubbink, Prof. Claudio Toniolo, and Dr. Dmitri Filopov, from which I learned a lot. I would like to acknowledge the contribution of Dr. Ine Segers-Nolten, Nico Meeuwenoord, Ruud Spruijt, and Cor Wolfs in the preparation of the samples and for providing me with the initial measurements, which saved me a lot of time.

I am thankful to Henriette van Leeuwen, for her support in all the administrative matters, and to Jos Disselhorst and Harmen van der Meer for their technical assistance. I am grateful to Siva Kanaku at Expeditie, and Frans Folst and Tom Jansen at the Leidse Instrumentmakers School who prepared the delicate glass tubes for me and helped me with the last-important step in the preparation of the degassed samples. I thank Arno van Amersfoort and Ruud Kuyvenhoven for the maintenance of the computers and the computer network.

I would like to thank all my friends and colleagues at Leiden University, at Leiden Observatory, in the Biophysics group, and especially in the MoNOS group for turning the work environment into a sociable and friendly place. Diagonalization, Hamiltonian, and many other expressions would have stayed strange terms for me, if Dr. Silvia Sottini would not have spent her time on sharing her knowledge with me. The simplified sketches and drawings of the instruments in my lab books are the results of the fruitful discussions that I had with Dr. Huib Blok. I would like to thank Martin van Son and Sandra Scanu, not only for their scientific contribution, but also for being good and caring friends. I am also thankful to Faezeh Nami for encouraging me to sport actively, which helped me a lot to reduce the work pressure.

I would like to acknowledge the FOM organization, which beyond the financial support, provided me with lots of opportunities to improve important skills and to get in contact with experts. I am grateful to Harry Linders who had an important role in the last phase of my PhD period and helped me to orient myself.

I would like to thank my family, especially my parents for their endless support, love, and dedication in each step and every moment of my life; Mitra, Mehran, and Masoud for being always there and supporting me by all their means, and Mahdi with whom I shared every single minute of my PhD period and who has always encouraged me to keep going despite all the challenges.

